UNIVERSITÀ CAMPUS BIO-MEDICO DI ROMA

DEPARTMENTAL FACULTY OF ENGINEERING

Ph.D. Course in Science and Engineering for Humans and Environment
Curriculum Bioengineering

XXXVII Cycle

Wearable Technologies and Sensors for Enhanced Physiological Monitoring in Healthcare and Sports

Coordinator
Prof. Giulio Iannello

Supervisors
Prof. Emiliano Schena
Eng. Carlo Massaroni

Ph.D. Candidate
Chiara Romano

To the experiences that enriched this journey,
to the twists and turns that gave it meaning.
To my family for their unwavering support,
to the friends I met along the way,
and to the ones always by my side.

Abstract

Technological innovations have reshaped healthcare and wellness, promoting proactive health management. Among these advancements, wearable devices (WDs) contribute significantly by enabling continuous, long-term monitoring of physiological parameters beyond clinical setting. This enhances health awareness and supports clinical decision-making with objective data. In sports, WDs facilitate real-time tracking of multiple physiological and biomechanical parameters, optimizing training and helping to prevent injuries. However, despite these benefits, real-world monitoring is not yet fully integrated into everyday practice due to persisting limitations, particularly in measurement accuracy and user comfort, which still need to be addressed.

This PhD thesis focuses on the design, development, and validation of WDs for cardiac and respiratory monitoring across daily life, clinical, and sports settings. It highlights the importance of adapting WDs to each context, particularly in non-laboratory conditions. For daily life applications, inertial measurement unit (IMU) sensors were investigated for heart rate (HR) and respiratory rate (RR) monitoring. Sensor placement has been shown to significantly influence accuracy, with the mitral valve location providing the best performance for HR and RR monitoring. Moreover, while IMU-based methods have demonstrated promising performance for HR estimation, RR monitoring remains more challenging due to the higher susceptibility to motion artifacts and postural changes. To address these limitations, textile-based sensors have been investigated, providing improved RR estimation, even in dynamic conditions. In clinical settings, research demonstrated that IMU sensor placement and algorithm selection impact the classification of aortic stenosis. Sensors at the pulmonary and mitral valves yielded the highest accuracy (>95%), with support vector machines outperforming deep learning models. Similarly, heart rate variability analysis with IMUs demonstrated that performance depends on posture, with supine measurements yielding better results. In sports, motion

artifacts pose a major challenge for respiratory monitoring. To address this issue, a smart facemask embedding a temperature sensor has been developed for breathing monitoring. Its working principle has been shown to mitigate the impact of motion, while its design minimizes the increase in airflow resistance typically associated with face masks, preserving athlete comfort. Testing confirmed its accuracy, with a mean absolute error below 1 breath per minute. Chest-worn devices, commonly used in sports due to their comfort, were also tested. Since they are prone to motion artifacts, an algorithm was developed to assess signal quality and identify unreliable breaths. This approach reduced the mean absolute percentage error by 30.7% during high-intensity interval training while excluding only 4.4% of detected breaths, demonstrating its effectiveness compared to the unprocessed data.

In conclusion, leveraging IMU sensors, textile-based technologies and temperature sensing systems, this work investigates sensor design and configurations, their placement on the body and algorithms to improve the applicability and reliability of WDs in real-world scenarios.

The work is organized into five chapters: Chapter 1 presents the background and establishes the research context; Chapter 2 explores WDs for cardiac and respiratory monitoring in daily life; Chapter 3 presents IMU-based solutions for cardiac monitoring in clinical applications; Chapter 4 investigates WDs for respiratory monitoring in sports; Chapter 5 summarizes the main findings and explores future perspectives in wearable monitoring systems.

Keywords

Wearable devices, Physiological monitoring, Inertial measurement units, Signal processing, Healthcare technology, Sports science, Clinical applications, Motion artifacts, Respiratory rate, Cardiac monitoring

List of Acronyms, Symbols, and Abbreviations

A Amplitude

AB Adaboost

AC Aortic Valve Closure

AC Alternating Current

AI Artificial Intelligence

AO Aortic Valve Opening

AS Aortic Stenosis

ASp Peak of Atrial Systole

AV Atrioventricular

AV Aortic Valve

AVA Aortic Valve Area

$\boldsymbol{A_{avg}}$ Average Amplitude of Displacement

$\boldsymbol{l_0}$ Baseline Distance Between Markers at The End of The First Inhalation

BH Bioharness Chest Strap

BMI Body Mass Index

bpm Beats Per Minute

brpm Breaths Per Minute

CNN Convolutional Neural Network

COPD Chronic Obstructive Pulmonary Disease

CT Comftech Vest

CTI Cardiac Time Intervals

CVD Cardiovascular Disese

CWT Continuous Wavelet Transform

DC Direct Current

DF Differential Flowmeter

DFA Detrended Fluctuation Analysis

DL Deep Learning

DT Digital Transformation

ECG Electrocardiogram

EDR Electrocardiogram Derived Respiration

FBG Fiber Bragg Grating Sensors

FIR Finite Impulse Response

FOS Fiber Optic Sensor

g standard gravity

GCG Gyrocardiogram

GF Gauge Factor

HF High Frequency

HFD Higuchi Fractal Dimension

HIIT High-Intensity Interval Training

HR Heart Rate

HRV Heart Rate Variability

HWA Hot Wire Anemometers

IBI Inter Beat Intervals

IC Isovolumic Contraction

IM Isovolumic Movement

IMU Inertial Measurement Unit

IoT Internet Of Things

IVCT Isovolumic Contraction Time

IVRT Isovolumic Relaxation Time

LF Low Frequency

LOA Limits Of Agreements

LVET Left Ventricular Ejection Time

MAE Mean Absolute Error

MAPE Mean Absolute Percentage Error

MAPE IR Mape Improvement Rate

MC Mitral Valve Closure

ML Machine Learning

MO Mitral Valve Opening

MOD Mean Of Differences

MRI Magnetic Resonance Imaging

MV Mitral Valve

NTC Negative Temperature Coefficient

NTC Negative Temperature Coefficient

PCG Phonocardiogram

PDMS Polydimethylsiloxane

PEP Pre-Ejection Period

PLA Polylactic Acid

PPG Photopletismography

PSD Power Spectral Density

PTC Positive Temperature Coefficient

PV Pulmonary Valve

R Resistance

RE Peak of Rapid Systolic Ejection

$\boldsymbol{x(t)}$ Relative Displacement,

$\boldsymbol{\Delta R}$ Resistance Change

RF Random Forest

RFp Peak of Rapid Diastolic Filling

RH Relative Humidity

RIFT Ramp Incremental Respiratory Frequency Test

RMSE Root Mean Square Error

RMSSD Root Mean Square of Successive Differences

RR Respiratory Rate

RSA Respiratory Sinus Arrhythmia

SA Sinoatrial

SampEn Sample Entropy

SCG Seismocardiogram

SD Standard Deviation

SD Standard Deviation

SD1 Short-Term Variability

SD2 Long-Term Variability

SDNN Standard Deviation of Ibi Values

SH Smart Healthcare

SNR Signal to Noise Ratio

SpO2 Blood Oxygen Saturation

SQI Signal Quality Index

$\boldsymbol{S_e}$ Static Sensitivity

STFT Short Time Fourier Transform

SVM Support Vector Machine

T Temperature

TAVI Transcatheter Aortic Valve Implantation

TE Ambient Temperature

$\boldsymbol{T_{Exp}}$ Temperature Of Exhaled Air

TPU Thermoplastic Polyurethane

TR Respiratory Period

TV Tricuspid Valve

TW Tymewear Vest

VLF Very Low Frequency

VMU Vector Magnitude Unit

$\boldsymbol{V_0}$ Voltage Variation

WD Wearable Devices

X Xiphoid Process

λB Bragg Wavelength

$\boldsymbol{\varepsilon}$ Strain

$\boldsymbol{\rho}$ Pearson's Correlation Coefficient

List of Contents

Abstract iii
List of Acronyms, Symbols, and Abbreviations v
List of Contents ix
List of Figures xi
List of Tables xvi
List of Equations xvii
Chapter 1: Wearable Technologies in The Era of Digital Transformation 1
1.1. Introduction 1
1.2. Digital transformation of healthcare 2
1.3. The role of wearables in healthcare and sports 4
1.4. Cardiac and Respiratory Monitoring: Clinical Relevance and Traditional Approaches 7
1.4.1. Cardiac activity 7
1.4.2. Respiratory activity 10
1.5. Wearable solutions for cardiac and respiratory monitoring 14
1.5.1. Cardiac activity 14
1.5.2. Respiratory activity 26
1.6. Key factors influencing wearable design 35
1.7. Ph.D. candidate contribution 37
Chapter 2: Wearable Sensors for Cardiac and Respiratory Monitoring in Daily Life 39
2.1. Introduction 39
2.2. IMU-based physiological monitoring 40
2.2.1. IMU sensors for cardiac and respiratory monitoring 40
2.2.2. Evaluating sensor position and its impact on data accuracy using accelerometers 41
2.2.3. Influence of sensor configuration on measurement using accelerometers and gyroscopes 51
2.3. Textile-based sensors for respiratory monitoring 58
2.4. Conclusions 72
Chapter 3: IMU-Based Solutions for Cardiac Monitoring in Clinical Applications 74

3.1. Introduction 74
3.2. IMU sensors for HRV extraction 76
3.3. IMU applications for aortic stenosis classification 86
3.4. Conclusions 93
Chapter 4: Wearable Sensors for Respiratory Monitoring in Sports Science 95
4.1. Introduction 95
4.2. Design and development of a smart facemask for respiratory monitoring in sports 97
4.2.1. Design and working principle 98
4.2.2. Laboratory bench test 101
4.2.3. Validation during cycling 104
4.3. The role of algorithms in respiratory frequency estimation in sports 111
4.3.1. Comparative evaluation of torso-worn wearables for breathing monitoring in soccer 112
4.3.2. Development of an algorithm for improving the estimation of breath-by-breath RR during sports and exercise 122
4.4. Conclusions 130
Chapter 5: Conclusions 133
Bibliography 136
List of Publications 158

List of Figures

Figure 1.1: Schematic representation showing the key enabling technologies and the main benefits of digital transformation in healthcare and wellness fields. 4

Figure 1.2: WDs enabling continuous health monitoring across clinical, daily life, and sports environments. 5

Figure 1.3. Anatomy and function of the heart. Left: Structural overview of the heart chambers, valves, and blood flow pathways. Right: The heart's electrical conduction system, showing the sinoatrial (SA) node, atrioventricular (AV) node, Bundle of His, Purkinje fibers, and associated conduction pathways. 8

Figure 1.4. Visualization of the cardiac conduction system and its corresponding phases on the ECG. The panels illustrate the propagation of electrical signals through the heart during different stages of the cardiac cycle, including atrial depolarization (P wave), ventricular depolarization (QRS complex), and ventricular repolarization (T wave). .. 9

Figure 1.5. Schematization of breathing mechanics during inspiration and expiration. 11

Figure 1.6. Schematization of traditional techniques for respiratory assessment. a) Bell spirometer; b) Hot-wire anemometer; c) Fleisch pneumotachograph; d) Turbine pneumotachograph; e) Lung Plethysmograph. 13

Figure 1.7. Prevalence of wearable sensor techniques in cardiac monitoring based on Scopus search results. The chart illustrates the distribution of different sensing approaches in WDs for cardiac activity monitoring. 15

Figure 1.8. Overview of different types of wearable electrodes for cardiac monitoring. The categories include microneedle electrodes, textile-based electrodes, and 3D-printed electrodes. 17

Figure 1.9. Schematization of a capacitive MEMS accelerometer structure (left) and temporal relationship between ECG and SCG signals (right), showing key cardiac electrical events, mechanical events, and time intervals..... 20

Figure 1.10. Schematization of capacitive vibrating mass gyroscope structure (left) and temporal relationship between ECG and GCG signals (right), highlighting electrical waves, mechanical cardiac events, and key time intervals. 22

Figure 1.11. Schematic of a multi-point FBG sensing system for SCG measurement. Left: FBG array configuration and chest placement. Right: SCG signals from different measurement points with a detailed view of aortic opening (AO) events. Adapted from [121]. 24

Figure 1.12. Schematic representation of PPG sensor (on left) and PPG signal (on right). 25

Figure 1.13. Overview of wearable solutions for breathing monitoring..... 27

Figure 1.14. Prevalence of wearable sensor techniques in respiratory monitoring based on Scopus search results. The chart illustrates the distribution of different sensing approaches in wearable respiratory monitoring. 28

Figure 2.1: Schematization of experimental setup and protocol. ----------43

Figure 2.2: Overview of the data processing pipeline for axis and sensor selection in cardiac and respiratory monitoring. 44

Figure 2.3: Results of axis and sensor selection for cardiac (top) and respiratory (bottom) activity. Percentages for sensor selection indicate the proportion of subjects for whom each sensor position performed best, while percentages for axis selection reflect the overall performance of each axis across all sensor positions and subjects. Standing includes both pre- and post-exercise conditions. 47

Figure 2.4: MAE values for HR (left) and RR (right) estimation across different activities. The values within the bars indicate the MAPE values for each posture. In the bottom panels the Bland-Altman plot is reported per each posture. Different colors represent different subjects. 49

Figure 2.5: Comparison of MAE between the general-purpose and posture-dependent configurations for HR (left) and RR (right) estimation across different activities. 50

Figure 2.6: IMU sensor positioning on the subject's chest. Filtered accelerometer and gyroscope signals isolating the cardiac and respiratory components.....53

Figure 2.7: HR and RR values were extracted using frequency-domain analysis in sliding windows with six different sizes. Welch's method was applied to identify the dominant frequency, and examples of HR and RR values for one subject are shown across all window sizes. 55

Figure 2.8: Bar graph of the MAE values for HR (top) and RR (bottom) analysis, comparing accelerometer (black) and gyroscope (grey) across different postures and window lengths. Mean MAE values and standard deviations are reported for all subjects. ACC: accelerometer; GYR: gyroscope; STD: standard deviation. 56

Figure 2.9: Bland Alman plots for accelerometer and gyroscope used for HR and RR estimations in different postures. 57

Figure 2.10: (a) Illustration showing the placement of 89 photo-reflective markers on the chest wall, divided into two sections: the abdomen (marked in violet) and the rib cage (marked in blue). The diagram also shows the connections between the pairs of markers. (b) A graph representing the relative

displacement signal (i.e., x) between two markers over time, highlighting maximum peaks (end of inhalation, shown as green triangles) and minimum peaks (end of exhalation, shown as blue triangles).....61

Figure 2.11: Representation of the connections between markers positioned on the anterior and posterior rib cage. The colormap indicates $Uavgnorm$ values, which combine deformation metrics with normalized SNR values.....62

Figure 2.12: Schematization of the main steps involved in the fabrication of the two piezoresistive textile sensors and their integration into the WD using a polymer matrix.....64

Figure 2.13: (A) Illustration of the output response of the sensors integrated into the WD under a quasi-static tensile load, with strain levels reaching up to 10% of their initial length. (B) Visualization of the hysteresis cycles produced by the sensors when subjected to cyclic loading at different simulated breathing frequencies: 6 bpm, 12 bpm, 24 bpm, and 36 bpm.....67

Figure 2.14: Experimental setup with flexible sensors integrated into the WD and a PLA case housing the signal conditioning and data acquisition modules. The protocol included quiet breathing and tachypnea in sitting, standing, and walking conditions, with signals compared to those from the BH reference system.....69

Figure 2.15: Bar charts display the mean RR values across all subjects for Sensor A, Sensor B, and the WD, representing the summed signal from both sensors. The results are shown for all phases of the experimental protocol, along with their respective standard deviations. 70

Figure 3.1: Schematization of experimental setup, protocol, and main steps carried out for data analysis. Adapted from [260]. ----------78

Figure 3.2: Classification of HRV indexes into Linear and Non-Linear categories. Linear indexes are further divided into time-domain and frequency-domain methods. Adapted from [260]. ---------- 80

Figure 3.3: A representative Poincarè plot. n: number of IBIs ---------- 83

Figure 3.4. Correlation coefficients (R) calculated using ECG-derived HRV indexes as the reference. Panel (a) shows the results from the optimized axis selection described above, while panel (b) represents the conventional axes used in the literature, with the z-axis selected for SCG and the y-axis for GCG. Adapted from [260]. ---------- 85

Figure 3.5. Experimental setup (a) and protocol (b) used for testing AS patients and the healthy group. Additionally, the ML and DL techniques employed for data analysis are illustrated (d). Adapted from [280]. ---------- 89

Figure 3.6. Mean recognition accuracies obtained from cross-validation tests for increasing probe durations, leveraging SCG and GCG signals as inputs to SVM- and RN18-based classifiers. The results from different frame analyses are combined at the score level. Adapted from [280].---------- 93

Figure 4.1: Diagram of the system architecture showing the main components (remote base station, central data logger, sensor unit, and case unit) along with their respective modules. Adapted from [296]. ----------98

Figure 4.2: Example of a normalized resistance signal (A) and the corresponding normalized temperature signal (B) recorded during breathing with the smart facemask. The normalized signal (C) was collected from the reference flowmeter used for validation. In all signals, the segment a–b shows the end-inspiratory apnea, c–d represents the expiratory phase, and d–e marks the inhalation phase. Adapted from [296].---------- 100

Figure 4.3: schematization of the experimental setup (a) used for the in-laboratory testing of the smart facemask. Also, the signal collected during the bench test (b) and the signal processing steps (c) are reported. brpm: breaths/min Adapted from [296]. ---------- 102

Figure 4.4: Comparison between RR values set on a mechanical ventilator (Set RR) and those measured by the smart face mask (Measured RR). Error bars represent mean±uncertaint; brpm: breaths/min. Adapted from [296].---------- 103

Figure 4.5: experimental setup and protocol carried out during the indoor tests of the smart facemask on cyclists. Adapted from [296]. ---------- 104

Figure 4.6. experimental setup and protocol carried out during the outdoor tests of the smart facemask on cyclists. Adapted from [296]. ---------- 107

Figure 4.7: experimental setup and protocol carried out during the outdoor tests of the smart facemask on cyclists. Adapted from [296]. ---------- 108

Figure 4.8: Average values of external temperature (TE) and signal amplitude (A) for each volunteer during indoor and outdoor tests. ---------- 108

Figure 4.9. (A) RMSE values using the smart facemask and the reference system against the metronome during the RIFT in indoor tests; (B) RR values trend calculated using the smart facemask and the metronome during RIFT in outdoor tests; (C) RMSE values using the smart facemask against the metronome during RIFT in indoor and outdoor tests. Adapted from [296]. ---------- 109

Figure 4.10: mean and standard deviation of RR values over time during RIFT and HIIT tests in indoor and outdoor setting. All the volunteers were considered inhis analysis. Adapted from [296]. ---------- 110

Figure 4.11: Experimental setup, protocol and main steps carried out for data analysis. Adapted from [312]. ---------- 115

Figure 4.12: MAPE (A), false negative (B) and false positive (C) values found per each prominence values. All WDs under test and all the protocol phases were considered in the analysis separately. Adapted from [312].---------- 117

Figure 4.13: mean and standard deviation of RR values during the RIFT test considering all subjects and the three WDs under test. Adapted from [312]. ---------- 118

Figure 4.14: mean and standard deviation of RR values during the HIIT test considering all subjects and the three WDs under test. Adapted from [312]. ---------- 119

Figure 4.15: MAPE values per each window length used to calculate the average RR over time. Data are reported per each phase of the protocol and WD under test. Adapted from [312]. ---------- 120

Figure 4.16: Outline of the primary steps in the SQI-based algorithm designed to exclude unreliable breaths: (a) signal preprocessing; (b) breath detection; (c) segmentation of breaths and assessment of the average template signal; (d) similarity analysis and elimination of unreliable breaths. Adapted from [314]. ---------- 125

Figure 4.17: Schematization of the experimental setups (a) and protocols (b) during walking and running tests. Adapted from [314].---------- 126

Figure 4.18: Schematization of the experimental setup (a) and protocols (b) during cycling tests. Adapted from [314].---------- 127

Figure 4.19: MAPE improvement rate and percentage of excluded breaths per each threshold and each protocol phase. Adapted from [314].---------- 128

Figure 4.20: MAPE values for all subjects and all protocols using 0.8 as correlation threshold. Adapted from [314]. ---------- 129

Figure 4.21: Raw normalized respiratory signal collected during HIIT (A) and respective breath-by-breath RR values (B). Also, the RR values with the exclusion of unreliable breaths are reported (C). Adapted from [314]. ---------- 130

List of Tables

Table 3.1: Bland-Altman analysis results and R coefficients for IBI calculated from SCG and GCG, compared with those calculated with ECG. ----------79

Table 3.2: Mean and standard deviation of HRV linear indexes calculated with time domain (SDNN, RMSSD, pNN50) and frequency domain (LF, HF, LF/HF) analysis. *:statistically significant (p <0.05). ----------84

Table 3.3: Mean and standard deviation of HRV non linear indexes. *:statistically significant (p <0.05). ----------85

Table 3.4: Recognition performance, in terms of accuracy (mean ± standard deviation, in %), for a single frame lasting 10s used as a probe, considering SCG and GCG sensors placed at different positions, and different classifiers. The best-performing results for each input type and sensor position are highlighted in bold. ----------91

Table 3.5: recognition performance, in terms of accuracy (mean ± standard deviation, in %), for a single frame lasting 10 s used as probe, jointly exploiting SCG and GCG signals, and both SVM- and RN18-based classifiers. ----------92

Table 4.1: Breath-by-breath analysis results: (A) RIFT test and (B) HIIT test. ---------- 106

Table 4.2: Window analysis results: (A) RIFT test and (B) HIIT test. ------ 106

Table 4.3: Values of MOD and LOA obtained from Bland-Altman analysis of RR extracted using breath-by-breath and window-based analyses. ---------- 121

List of Equations

Equation 2.1: ----------45

Equation 2.2: ----------61

Equation 2.3: ----------65

Equation 2.4: ----------65

Equation 2.5: ----------66

Equation 3.1: ----------81

Equation 3.2: ----------81

Equation 3.3: ----------81

Equation 4.1: ---------- 103

Equation 4.2: ---------- 107

Equation 4.3: ---------- 123

Equation 4.4: ---------- 124

Equation 4.5: ---------- 127

1

Chapter 1: Wearable Technologies in The Era of Digital Transformation

1.1. Introduction

Technological innovation has integrated into our daily lives, with advancements such as artificial intelligence (AI), Internet of Things (IoT), cloud computing, big data analytics, and sensors reshaping healthcare and wellness [1]–[6]. The advent of these technologies has not only transformed the way that health and well-being are approached but has also promoted person-centered care [7], [8]. This change reflects both a technological advancement and a cultural shift away from reactive treatment towards proactive health management, placing greater emphasis on early disease detection and prevention through continuous tracking of health-related factors [9].

The evolution of wearable devices (WDs) is at the core of this change [7], [10]. They enable individuals to track vital signs continuously over extended periods, increasing consciousness of personal health and lifestyle choices while providing health professionals with useful data to guide their decisions on treatment plans [11], [12]. WDs are becoming important for managing cardiovascular and respiratory diseases (CVRDs), which are the leading causes of death worldwide [13]. According to the World Health Organization, in 2021, the top 10 causes of death accounted for 39 million deaths, with cardiovascular diseases (such as ischemic heart disease and stroke) and respiratory diseases (such as chronic obstructive pulmonary disease and lower respiratory infections)

ranking among the leading causes [14]. The global burden of CVRD is further increased by inequalities in access to healthcare, particularly between high-income and lower-middle income countries. Despite international efforts, including the UN Sustainable Development Goal to reduce premature mortality from CVRDs, many countries still struggle to implement effective interventions. Integrating WDs into healthcare systems could help address this challenge by enabling continuous monitoring of parameters related to cardiac and respiratory activities. Moreover, they have the potential to make long-term monitoring more accessible, reducing both mortality and financial pressure on healthcare systems.

Beyond clinical applications, WDs are also encouraging health management in daily life [12], [15], [16]. Moreover, in sports field, WDs are transforming how athletes train and perform. They not only assist in evaluating physical effort but also enable the monitoring of physiological variables such as heart rate variability (HRV), respiratory rate (RR) and muscle fatigue, useful for optimizing training strategies and preventing injuries. For example in endurance sports such as cycling and running, they help coaches tailor training strategies and assist in evaluating physical effort, promoting safer and more efficient athletic experiences [17].

Given the growing importance of WDs in both healthcare and sports, this thesis will explore their role in the future of personalized health monitoring. Initially, an overview will be provided on the concept of digital transformation in healthcare and its impact, followed by an analysis of the contributions of WDs to both medical and sports settings. The function of WDs in this context will next be examined, with particular emphasis on their contribution to monitoring cardiac and respiratory activity.

1.2. Digital transformation of healthcare

Digital transformation includes the systematic integration of digital technologies across societal and industrial sectors [19], with global investments projected to increase from $1.6 trillion in 2022 to $3.9 trillion by 2027 [20]. The

adoption of digital solutions in healthcare is powered by demographic changes, an increase in the prevalence of chronic diseases and greater health awareness among populations [21]. Through data analytics and connected technologies, this digitization optimizes administrative workflow, improves clinical outcomes, and enhances service delivery efficiency [7], [22], [23]. This approach reduces costs, while supporting data-driven decisions through predictive modelling and preventive health management strategies [24]–[26].

Several technologies drive the digitalization of healthcare: IoT connects sensors between medical devices to enable continuous monitoring and timely interventions [6], [10]; Big Data Analytics extracts information from healthcare datasets for resource optimization, risk assessment, and predictive modeling [27], [28]; AI and Machine Learning (ML) improve workflows through pattern recognition in disease progression and patient outcome prediction [29], [30]. Cloud computing complements this ecosystem by providing scalable data management and access to healthcare providers [26], [31]–[34]. Figure 1.1 summarizes these enabling technologies and their applications in health/wellness.

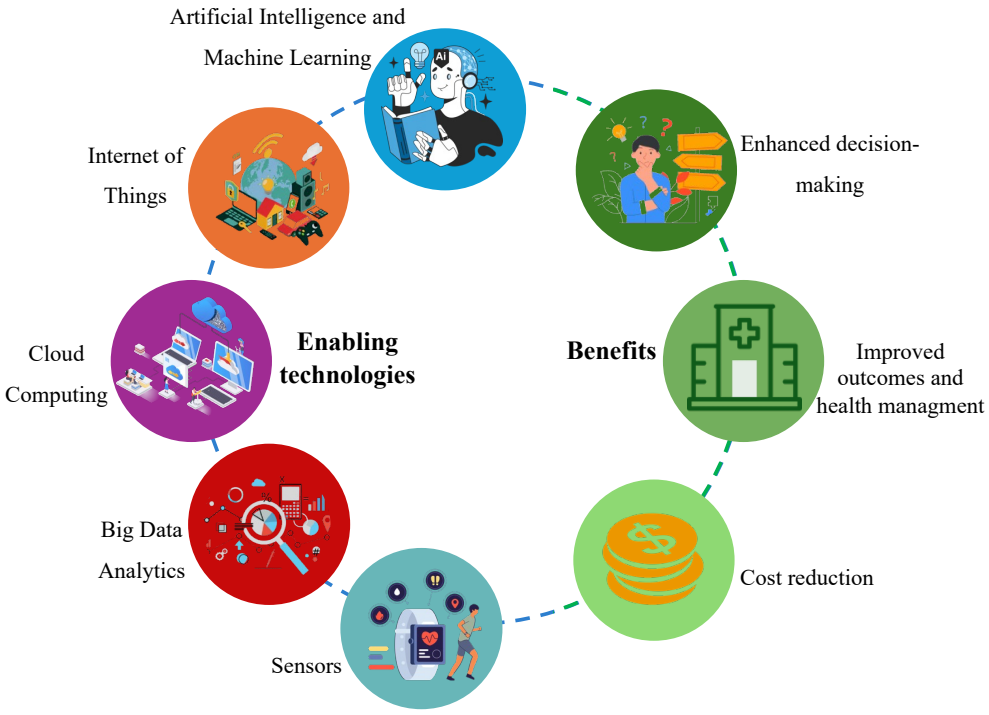

Figure 1.1: Schematic representation showing the key enabling technologies and the main benefits of digital transformation in healthcare and wellness fields.

In the digital health ecosystem, WDs are the main point of contact between patients and healthcare systems. These devices provide data streams by continuously tracking physiological parameters, which are then integrated with cloud infrastructure, analytics platforms, IoT networks and artificial intelligence systems to provide proactive and personalized health management.

1.3. The role of wearables in healthcare and sports

WDs, commonly referred to as “wearable technologies” or "wearables," are compact electronic systems designed to be worn on the body or integrated into clothing and accessories. Market projections estimating that the wearable device market will reach 64 billion USD by 2025 [18]. Their wide adoption reflects their versatility in healthcare applications, from fitness monitoring and stress management, to chronic condition monitoring [35]. These devices enable continuous health assessment in clinical, home and sports environments, as illustrated in Figure 1.2.

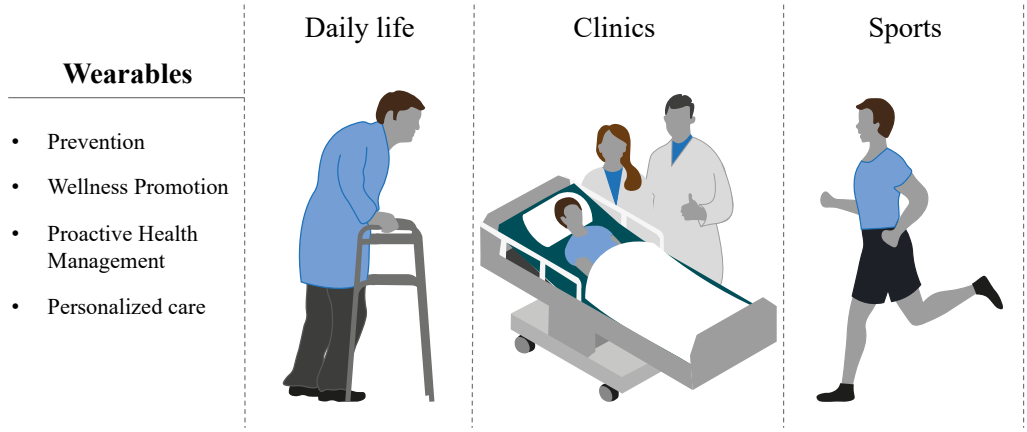

Figure 1.2: WDs enabling continuous health monitoring across clinical, daily life, and sports environments.

WDs are increasingly integrated into healthcare systems, with applications ranging from early disease detection to remote patient monitoring and preventive medicine. Beyond their role in general healthcare, WDs are particularly beneficial in supporting home-based care, rehabilitation, and disability management. In home settings, they can support patients after hospital discharge and assist in managing chronic conditions [37]–[39]. For example, by tracking daily activities, energy expenditure and sleep patterns, these devices can support more independent health management, especially benefiting the elderly and people with disabilities [38], [40]. In rehabilitation, WDs contribute to patient recovery by continuously monitoring progress and ensuring a safe return to activity [41]. This is particularly relevant considering that, according to the World Health Organization, 15% of the global population lives with a disability, a figure expected to rise due to aging [42]. Furthermore, approximately 2.4 billion people require rehabilitation services for conditions such as musculoskeletal disorders, stroke, and neurological diseases [43]. By providing continuous and objective monitoring, WDs enable therapists to personalize interventions, optimize recovery plans, and improve patient adherence. Their real-time tracking capabilities reduce reliance on infrequent clinical assessments, facilitating more adaptive and responsive rehabilitation programs.

In addition to their role in healthcare, WDs are transforming sports performance monitoring [44]. With approximately 44% of the EU population

engaging in exercise at least once a week [45], the growing participation in sports and fitness has increased the demand for effective performance tracking tools. Athletes and coaches widely adopt WDs for performance evaluation and injury prevention [17]. By monitoring parameters such as fatigue, biomechanical information, breathing-related parameters and cardiovascular response, these devices help manage training loads and recovery strategies. In team sports, these devices assist in workload management and injury prevention by monitoring player exertion levels and minimizing the risk of overtraining.

Although WDs are advancing rapidly and gaining widespread adoption, several limitations still hinder their integration into daily life, healthcare, and sports. In everyday use, challenges such as battery life constraints and user comfort affect long-term adoption. Within healthcare, a major concern is that most WDs are not classified as medical devices. As a result, their primary role remains wellness tracking, pre-screening, and trend analysis. Data privacy and security also pose significant risks, given that WDs collect and transmit sensitive health information, necessitating stringent encryption and compliance with healthcare regulations. In the sports sector, data accuracy and consistency are critical concerns, indeed factors such as environmental conditions, and athletes' movement, can impact sensor reliability.

Despite these challenges, WDs continue to evolve. Among the most critical physiological parameters assessed through WDs, cardiac and respiratory measures stand out due to their role in detecting physiological and psychological states. These parameters, regulated by the autonomic nervous system, reflect stress levels, emotional states and systemic homeostasis [46], [47]. They help detect and manage conditions ranging from arrhythmias to respiratory disorders [48], providing information about general health status.

The significance of these parameters has established cardiac and respiratory monitoring as central applications for WD development. The technical strategies

and implementations for the various monitoring applications are described in detail in the following sections.

1.4. Cardiac and Respiratory Monitoring: Clinical Relevance and Traditional Approaches

Before examining wearable monitoring devices, it is useful to provide a summary of cardiac and respiratory monitoring activities. The physiological principles underlying these activities and their standard monitoring methods are presented in this part, which serves as a basis for understanding wearable monitoring technology.

1.4.1. Cardiac activity

The heart is a vital organ that maintains systemic circulation by pumping oxygenated blood to the body's tissues and returning deoxygenated blood to the lungs for gas exchange. Its structure comprises four chambers: the right and left atria and the right and left ventricles. These chambers are separated by valves (tricuspid, pulmonary, mitral and aortic) that ensure unidirectional blood flow. During the cardiac cycle, the right side directs deoxygenated blood to the lungs, while the left side pumps oxygenated blood to the systemic circulation [49]. The cycle consists of systole (ventricular contraction) and diastole (cardiac relaxation and chamber filling), controlled by the heart's electrical conduction system. This system originates in the sinoatrial (SA) node, which generates impulses that propagate through the atria, initiating atrial contraction and facilitating blood flow in the ventricles. They stop at the atrioventricular (AV) node to allow complete ventricular filling and travel through the His bundle and Purkinje fibers to coordinate ventricular contraction.

Cardiac function involves two interrelated components: electrical activity (impulse generation and conduction) and mechanical activity (muscle contraction and relaxation), as illustrated in Figure 1.3.

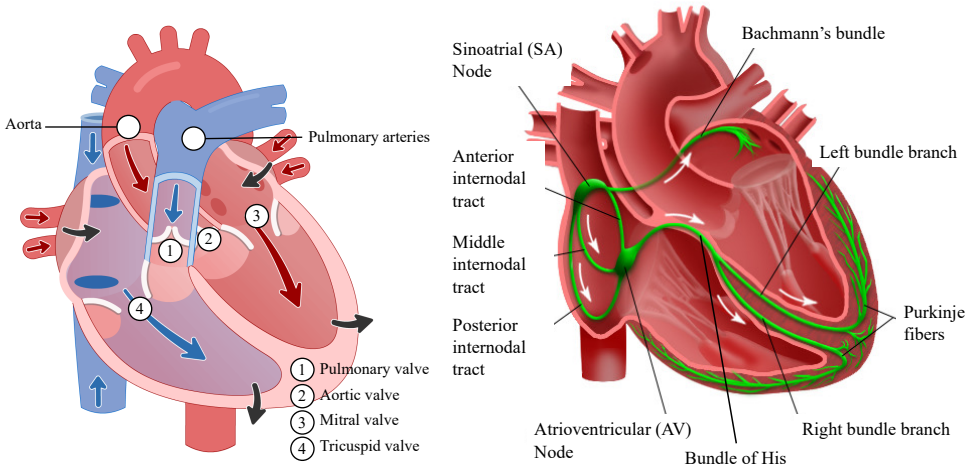

Figure 1.3. Anatomy and function of the heart. Left: Structural overview of the heart chambers, valves, and blood flow pathways. Right: The heart's electrical conduction system, showing the sinoatrial (SA) node, atrioventricular (AV) node, Bundle of His, Purkinje fibers, and associated conduction pathways.

A complete cardiovascular evaluation requires monitoring of both electrical and mechanical cardiac activities. Electrical signal monitoring allows arrhythmias [50], [51], conduction disorders [52], and other electrical abnormalities to be diagnosed. Mechanical monitoring assesses contractility, valve function, and blood flow through parameters including stroke volume, cardiac output, ejection fraction, and wall motion. These measurements help identify heart failure, valvular dysfunctions, and structural abnormalities [53]. Other parameters, such as left-ventricular ejection time (LVET) and isovolumic contraction time (IVCT), indicate specific conditions like aortic stenosis (AS) [54] and impaired contractility [55].

Heart rate (HR), expressed in beats per minute (bpm) and representing the number of heart cycles per minute, reflects both electrical and mechanical functions. Monitoring this parameter supports the management of cardiovascular disease and the optimization of physical activity [56], [57]. Furthermore, it allows the extraction of HRV, an index of autonomic nervous system function and stress levels, which is particularly relevant in occupational health monitoring [58].

Traditional techniques for monitoring cardiac activity include electrocardiography (i.e., ECG) for electrical activity, and phonocardiography and echocardiography for mechanical activity.

ECG records electrical signals through the ECG waveform (see Figure 1.4), comprising P waves (atrial depolarization), QRS complexes (ventricular depolarization), and T waves (ventricular repolarization) [59]. Standard ECG systems use a 12-lead configuration, requiring ten electrodes placed on the body to capture electrical activity from multiple perspectives [60]. Although this setup offers a complete assessment of cardiac function, its bulky instrumentation makes it less practical for long-term, portable monitoring outside clinical settings

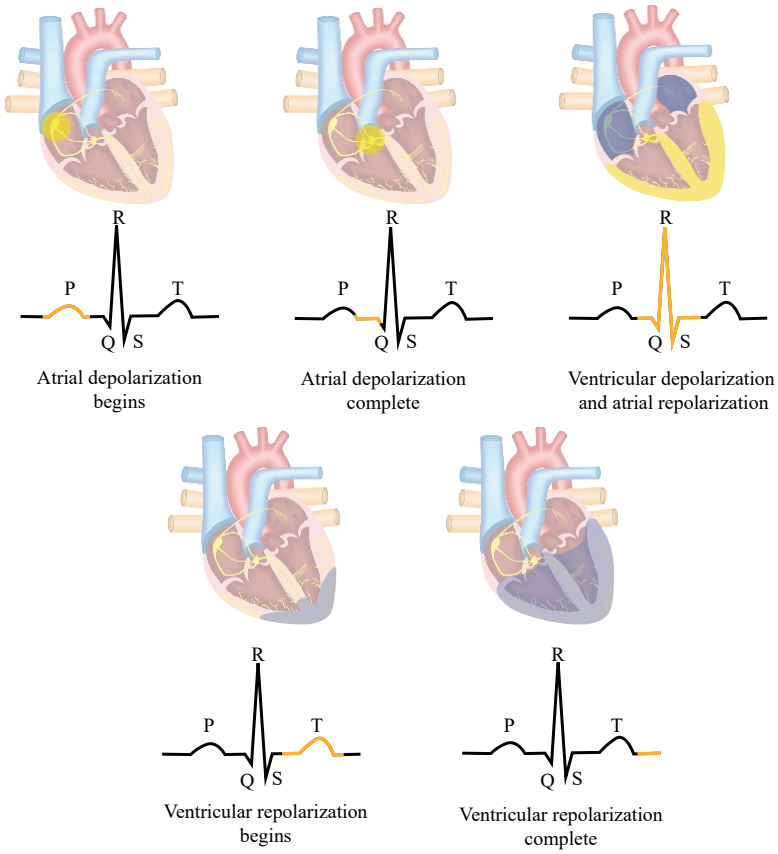

Figure 1.4. Visualization of the cardiac conduction system and its corresponding phases on the ECG. The panels illustrate the propagation of electrical signals through the heart during different stages of the cardiac cycle, including atrial depolarization (P wave), ventricular depolarization (QRS complex), and ventricular repolarization (T wave).

On the other hand, mechanical cardiac activity has traditionally been monitored by phonocardiography and echocardiography. Phonocardiography records cardiac acoustic signals (PCG). It measures sounds produced by valve movements and blood flow. These include the first cardiac sound (S1), associated with the closure of the mitral and tricuspid valves, and the second cardiac sound (S2), related to the closure of the aortic and pulmonary valves [61]. PCG is particularly effective in detecting valvular dysfunctions such as stenosis or regurgitation [62]. It is performed using a phonocardiograph, a device equipped with sensitive acoustic sensors, including microphones or piezoelectric transducers, placed on the chest to capture heart sounds. However, sensitivity to environmental noise and dependence on expert interpretation may limit its effectiveness in uncontrolled environments.

Echocardiography uses ultrasound to produce real-time images of the heart and provides a detailed assessment of mechanical activity. It assesses myocardial contractility, valve dynamics, and blood flow [62], [63]. Doppler echocardiography measures blood flow velocities, while 3D echocardiography offers volumetric imaging to diagnose complex structural abnormalities [64]. Echocardiography is widely used as the gold standard for diagnosing conditions such as heart failure, valvular diseases, and congenital defects. However, its reliance on specialized equipment and trained personnel typically confines its use to clinical settings.

1.4.2. Respiratory activity

The respiratory system, which includes the lungs, trachea, bronchi, larynx, pharynx and nose, facilitates the exchange of gases for cell metabolism. External respiration, in which oxygen and carbon dioxide are exchanged between the alveoli and the blood, and internal respiration, in which these gases are transferred between the blood and body tissues, are the two main components of this process.

Respiratory mechanics is based on the coordinated action of muscles, particularly the diaphragm and intercostal muscles, which create pressure gradients for airflow. During inspiration, the contraction and flattening of the diaphragm combine with the action of the intercostal muscles to elevate the rib cage, expanding the volume of the chest cavity and reducing the intrapulmonary pressure to draw air into the lungs. Exhalation follows when these muscles relax, reducing thoracic volume and increasing intrapulmonary pressure to expel air [65], as illustrated in Figure 1.5.

Several factors influence respiratory efficiency, including lung compliance, airway resistance and the elastic properties of the lungs and chest wall. Alterations in these parameters can lead to respiratory disorders, such as restrictive and obstructive lung diseases, which are often manifested by changes in RR.

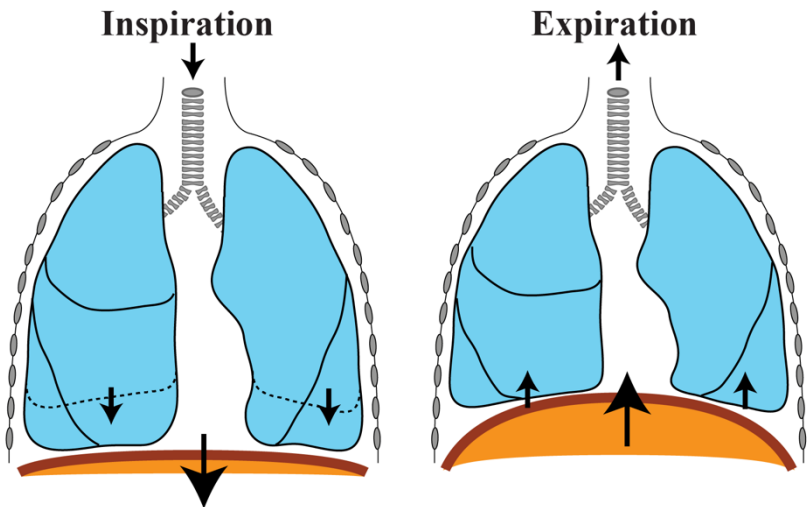

Figure 1.5. Schematization of breathing mechanics during inspiration and expiration.

RR, measuring breaths per minute (brpm or breaths/min), serves as an indicator of both physiological and pathological respiratory states [66], [67]. Its variations can predict critical events, including cardiac arrest and the need for intensive care [68], [69]. RR provides insight into physiological deterioration [70] and perceived exertion during physical activity [71], which are particularly relevant to patients with chronic respiratory conditions like asthma and chronic

obstructive pulmonary disease (COPD) [72], [73]. Traditional RR monitoring techniques include:

- Spirometers: represent the gold standard for the assessment of lung function [74]. These devices measure inhaled and exhaled air volumes during breathing cycles. During spirometry, patients wear nasal clips and breathe through a connected tube. As the patient inhales and exhales, changes in airflow or volume are recorded, with the method varying depending on the type of spirometer. Traditional devices, such as bell spirometers, measure lung volumes by recording the displacement of a sealed chamber caused by air movement, while modern digital variants directly measure airflow with integrated sensors.
- Flowmeters: quantify respiratory airflow rates by measuring air volume per time unit. They employ various technologies, including: i) Fleisch pneumotachographs measure airflow by detecting pressure differences across a resistive element, such as a series of capillary tubes. The pressure drop created by the resistive element is proportional to the flow rate [60]; ii) Hot-wire anemometers employ a thin, electrically heated wire that cools as air flows over it. The cooling rate is directly correlated to the air velocity, allowing calculation of the flow rate. These devices are particularly sensitive to low flow rates and are valued for their high temporal resolution [60]; iii) Turbine pneumotachographs determine flow rate based on the rotational speed of a turbine placed in the airflow path. As air flows through the device, it drives the turbine blades, and the angular velocity is used to compute the flow rate [60].
- Lung Plethysmography: measures comprehensive lung volumes and airway resistance using Boyle's Law principles, which relates pressure and volume in an enclosed system. The technique requires an airtight chamber where patients perform breathing maneuvers while connected to pressure measurement systems. The patient breathes through a mouthpiece connected to a pressure-measuring system, and slight

pressure variations correspond to changes in lung volume. Thoracic gas volume, which represents the air volume in the lungs at a specific moment, is calculated using simultaneous measurements of chamber and airway pressures [60]. While valuable for diagnosing both obstructive and restrictive conditions, its use remains limited to specialized settings due to complexity and cost. A schematization of traditional techniques is reported in Figure 1.6.

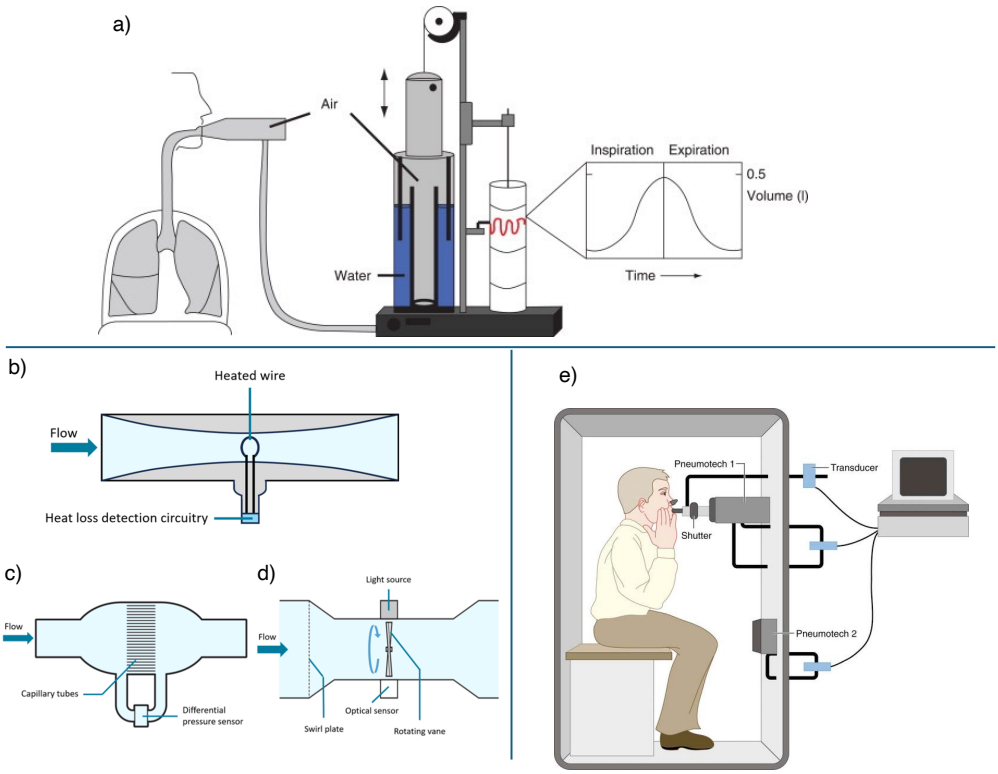

Figure 1.6. Schematization of traditional techniques for respiratory assessment. a) Bell spirometer; b) Hot-wire anemometer; c) Fleisch pneumotachograph; d) Turbine pneumotachograph; e) Lung Plethysmograph.

Though robust for lung function assessment, these established techniques primarily suit structured clinical environments. Their dependence on specialized equipment restricts their application for continuous monitoring in daily life settings.

1.5. Wearable solutions for cardiac and respiratory monitoring

While accurate, traditional monitoring methods are confined to clinical environments due to their specialized equipment requirements. Wearable technologies address these limitations by providing non-invasive, continuous monitoring capabilities in diverse settings. These solutions enable real-time data collection and analysis, expanding healthcare accessibility beyond traditional clinical boundaries.

This section will discuss the main wearable solutions for cardiac and respiratory monitoring.

1.5.1. Cardiac activity

The WD technologies for cardiac monitoring can be categorized based on the type of physiological parameter they measure. Figure 1.7 illustrates the prevalence of different sensing techniques in WDs for cardiac monitoring. To quantify the relative use of these technologies, a literature search was conducted on Scopus, focusing on peer-reviewed articles discussing WDs employing bioelectrical signals (e.g., ECG), mechanically induced movements (e.g.., seismocardiography - SCG and gyrocardiography - GCG), mechanically induced strain sensors (e.g., Fiber Bragg Grating sensors - FBGs), and blood volume changes (photoplethysmography – PPG sensors). The search queries included combinations of keywords related to each sensing approach, along with terms such as "wearable device", "wearable sensor", and "cardiac monitoring". The total number of articles retrieved for each technique was used to estimate its prevalence, and the results were normalized as percentages to generate the pie chart in Figure 1.7.

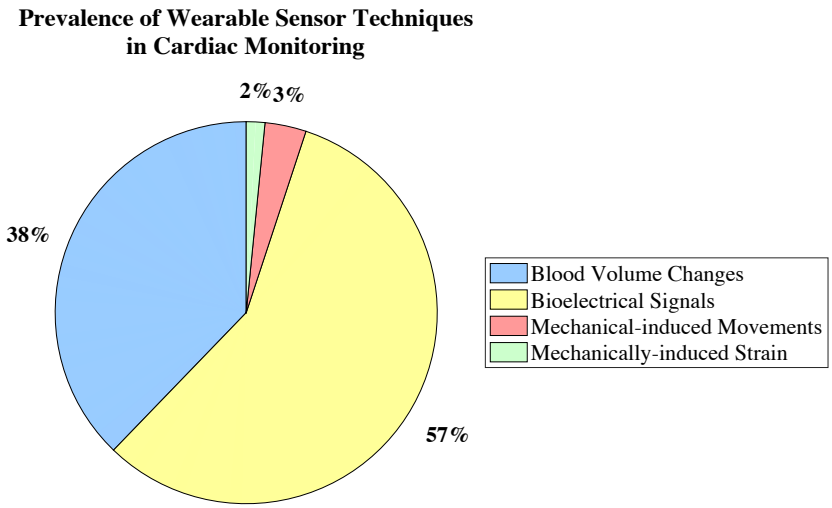

Figure 1.7. Prevalence of wearable sensor techniques in cardiac monitoring based on Scopus search results. The chart illustrates the distribution of different sensing approaches in WDs for cardiac activity monitoring.

The analysis highlights that bioelectrical signal (i.e., ECG) and blood volume changes (i.e., PPG) dominate wearable cardiac monitoring technologies, representing 57% and 38% of the reviewed studies, respectively. This trend reflects the long-standing clinical reliability of ECG and the widespread integration of PPG in consumer wearables, such as smartwatches and fitness trackers. In contrast, mechanically induced movements (3%) and strain-based sensors (2%) remain significantly less explored, suggesting that these techniques are still in early research stages. However, given their potential advantages, future advancements in sensor technology may lead to broader applications of these emerging methods in wearable cardiac monitoring.

The following is a brief description of the techniques listed above.

1. Bioelectrical signals

The development of WDs for continuous monitoring of the heart's electrical activity addresses the constraints of traditional ECG systems. Modern wearable ECG devices utilize single-lead configurations with two electrodes, made of flexible materials [75], [76]. This simplified design enables integration into everyday accessories like chest straps, and fitness bands. The evolution of

wearable electrodes has enhanced both accessibility and user comfort by eliminating adhesive gels and rigid components. These electrodes are classified according to their design approaches and material properties (see Figure 1.8):

- Dry electrodes: these electrodes are made in various forms, and do not require conductive gels, offering a solution for long-term monitoring. Main solutions include: i) 3D-Printed electrodes, which utilize materials such as conductive polylactic acid (PLA) and carbon composites to achieve high signal quality [77]–[79]. Designs like microdomes arrays or coiled tips help reduce impedance and motion artifacts, making them well-suited for continuous monitoring; ii) stretchable electrodes made from materials like polydimethylsiloxane (PDMS) or elastomers combined with conductive particles, designed to conform to the skin's surface and maintain consistent contact during movement, ensuring accurate signal acquisition in dynamic conditions.
- Hybrid (or semi-dry) electrodes: offer a middle ground between traditional wet and dry electrodes for biopotential signal acquisition. These electrodes use a small amount of conductive gel or electrolyte, often stored in microcapsules, to ensure stable skin contact and enhance signal quality. This design reduces issues such as skin irritation and drying, which are common with fully wet electrodes, while maintaining good performance [80], [81]. An example are textile electrodes, which are integrated into fabrics and constructed with conductive fibers or coatings (e.g., silver, graphene) to ensure flexibility, comfort, and reliable signal acquisition [82]–[84]. These are commonly used in applications requiring integration into clothing, such as T-shirts or chest bands.
- Microneedle Electrodes: penetrate the outermost layer of the skin to access the underlying tissue, thereby reducing skin-electrode impedance [85]. These electrodes are typically used in high-precision applications

but are less commonly integrated into everyday WDs due to their invasive nature [85]–[87].

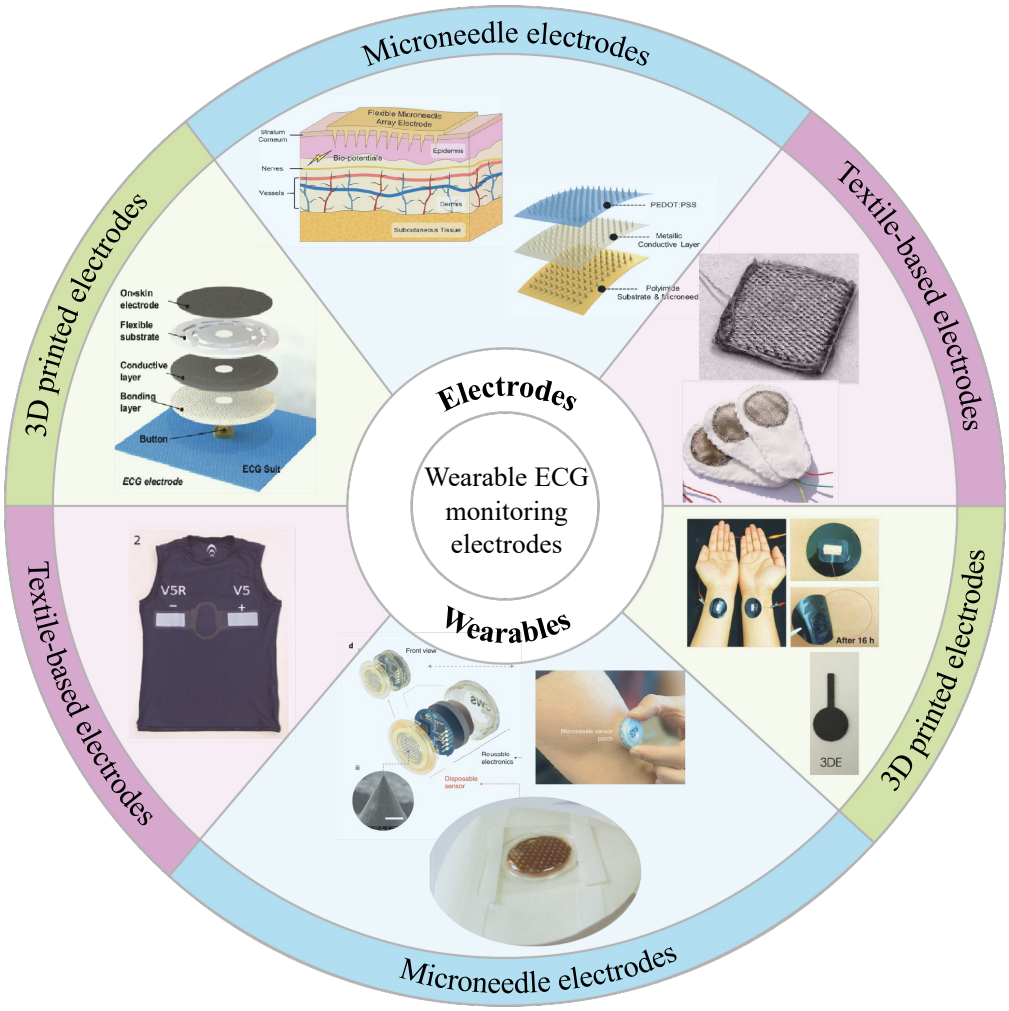

Figure 1.8. Overview of different types of wearable electrodes for cardiac monitoring. The categories include microneedle electrodes, textile-based electrodes, and 3D-printed electrodes.

While wearable electrodes offer advantages, they also present limitations that affect their performance and long-term usability. Dry electrodes, despite eliminating the need for conductive gels, suffer from signal degradation after washing, particularly in textile-based designs, where poor coating adhesion and surface wear reduce durability [88]–[91]. High-frequency (HF) noise and baseline fluctuations can interfere with ECG signal quality, while sweat-induced oxidation of metallic components further compromises long-term performance [92]. Similarly, microneedle-based electrodes, while improving signal quality by

reducing skin-electrode impedance, can cause discomfort and potential injury. A significant risk is fragmentation, where broken microneedles remain embedded in the skin, leading to localized irritation or damage [95], [96].

2. Mechanically-Induced Movements:

The mechanical activity of the heart, including muscle contractions, valve aperture and closure, and blood flow, generates vibrations that propagate through the thoracic tissues to the chest wall. The resulting precordial vibrations, detectable at the chest surface, reflect distinct cardiac mechanical events during the cardiac cycle, such as ventricular contractions, valve closures, and ventricular filling [97]. These vibrations are characterized by frequency bands associated with specific events: low frequencies (<50 Hz) from overall cardiac motion and higher frequencies (>50 Hz) related to valve dynamics and blood flow [98].

Among the innovative solutions, IMU sensors, comprising accelerometers and gyroscopes, have demonstrated good potential for cardiac monitoring. Unlike traditional techniques, IMU sensors can directly measure the mechanical aspects of heart function, through accelerations (seismocardiography, SCG) and angular velocities (gyrocardiography, GCG).

a. Linear Accelerations (SCG): the monitoring of cardiac mechanical activity through linear accelerations has been investigated using accelerometers positioned on the chest wall to capture cardiac-induced displacements. The signals measured through this method are known as SCG [98]. An accelerometer is a device used to measure acceleration by detecting the displacement of a suspended mass within its housing. Accelerometers can be monoaxial or triaxial. In a single-axis accelerometer, the mass is supported by a spring and moves only in the direction of the sensitive axis. When the device experiences acceleration, the mass is displaced from its equilibrium

position due to the force generated by inertia. The extent of this displacement depends on the stiffness of the spring and the magnitude of the acceleration acting on the system. The mass displacement is then converted into an electrical signal using different sensing methods. In capacitive sensing, changes in displacement alter the capacitance between plates. In piezoresistive sensing, the displacement changes the resistance of a material. In piezoelectric sensing, the displacement generates an electric charge. These methods allow the accelerometer to translate mechanical movement into measurable electric signals. Three single-axis accelerometers can be combined into a triaxial configuration to measure acceleration in three dimensions, with each sensor aligned along one of the three orthogonal axes.

SCG signal reflects the mechanical activity of the heart, especially chest wall vibrations caused by heart contractions, valve activity, and blood flow [99]. This signal is collected using accelerometers placed on the chest wall, typically at the xiphoid process level [98]. The SCG waveform exhibits distinct peaks that correspond to specific events in the mechanical activity of the heart [100]. These mechanical events occur with a characteristic time delay relative to their corresponding electrical events (on the ECG signal), reflecting the temporal relationship between cardiac electrical activation and subsequent mechanical responses. The main fiducial points are aortic valve opening (AO) and closing (AC), mitral valve opening (MO) and closing (MC), isovolumic contraction (IC), the peak of rapid systolic ejection (RE), the peak of rapid diastolic filling (RFp), and the peak of atrial systole (ASp) [101]. Additional fiducial points include isovolumic movement (IM) during ventricular isovolumetric contraction, as shown in Figure 1.9 [102]. The derivation of these intervals from SCG has been validated by comparing them with corresponding intervals obtained from ECG signals and

echocardiography [100], [103]. These fiducial points enable the calculation of cardiac time intervals (CTIs), such as the pre-ejection period (PEP), LVET, isovolumetric contraction time (IVCT), isovolumetric relaxation time (IVRT) and QS2, the interval between the onset of the Q wave in the ECG and the AC point, representing the total systolic time [104]. These parameters are useful for assessing myocardial contractility, systolic and diastolic function. SCG has been studied in the clinical setting to identify valve defects, arrhythmias and heart failure [105]. Moreover, it has been used in non-clinical applications for HR and RR monitoring in daily life applications [106]–[108]. However, challenges include variability in sensor placement, inter-subject differences (e.g., age, BMI, posture), and motion artifacts. Advances in ML and signal processing are addressing these limitations, improving fiducial point detection and overall reliability [109].

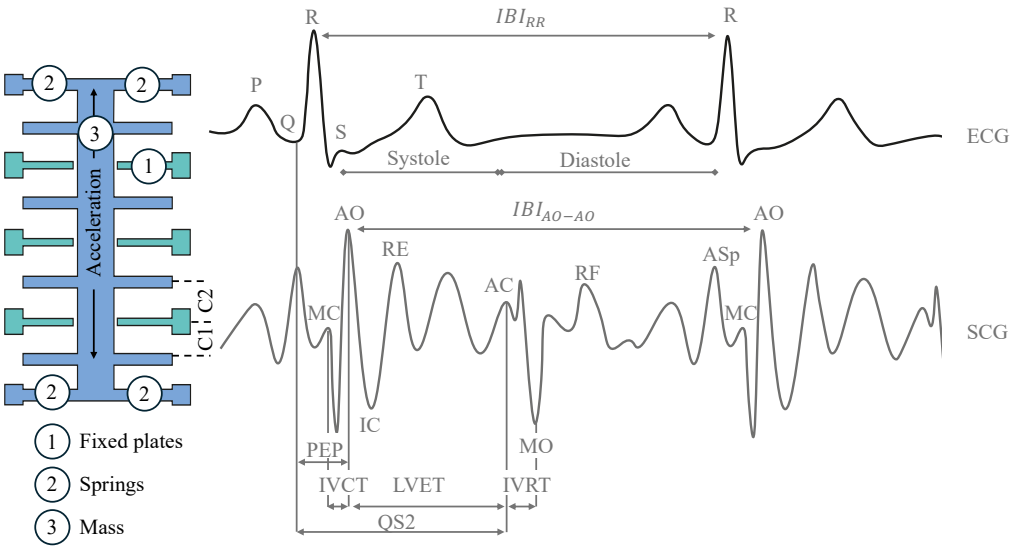

Figure 1.9. Schematization of a capacitive MEMS accelerometer structure (left) and temporal relationship between ECG and SCG signals (right), showing key cardiac electrical events, mechanical events, and time intervals.

b. Angular Velocities: gyroscopes placed on the chest wall quantify rotational movements induced by cardiac mechanics. The signal

collected through these sensors is called gyrocardiogram (GCG) [110].

A gyroscope is a sensor used to measure angular velocity, representing the rotation rate around a specific axis. Gyroscopes are based on various technologies, including spinning rotor gyroscopes, laser gyroscopes, and vibrating mass gyroscopes. Among them, vibrating mass gyroscopes are the most used for WDs. The operating principle of vibrating mass gyroscopes relies on the Coriolis effect, which describes the apparent force exerted on a vibrating mass when the device rotates. The gyroscope contains a mass that vibrates in a specific direction (driving direction), typically actuated by a piezoelectric element. When the device rotates, the Coriolis force acts on the vibrating mass, causing it to deflect in a direction perpendicular to both the axis of vibration and rotation. This deflection is proportional to the angular velocity and is measured using sensing elements such as capacitive, piezoelectric, or piezoresistive sensors. Like accelerometers, a three-dimensional gyroscope can be constructed by combining three single-axis gyroscopes, each aligned along one of the three orthogonal axes. This setup allows gyroscopes to measure angular velocity across multiple dimensions.

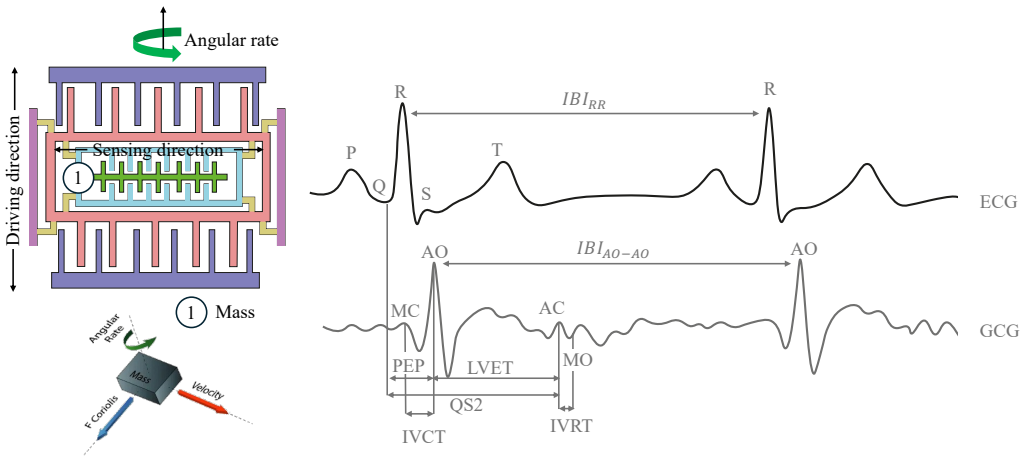

Figure 1.10. Schematization of capacitive vibrating mass gyroscope structure (left) and temporal relationship between ECG and GCG signals (right), highlighting electrical waves, mechanical cardiac events, and key time intervals.

GCG quantifies rotational movements of the chest wall induced by cardiac mechanics using gyroscopes. This method typically complements SCG by capturing angular dynamics, providing additional perspectives on cardiac events [111]. Despite its demonstrated potential in clinical and non-clinical contexts, including HR estimation and CTI analysis, GCG remains a relatively novel technique. Hence, the annotation of GCG signals is less well-established in the scientific literature compared to SCG [112]. Currently, only a limited set of fiducial points has been reliably identified in GCG signals, including MC, MO, AC, and AO (see Figure 1.10). From these fiducial points, it is possible to derive CTIs such as PEP, LVET, IVCT, IVRT, and QS2 [113]. GCG is also subject to challenges, including susceptibility to motion artifacts and the absence of standardized sensor placement and signal processing protocols.

One major challenge with SCG and GCG is the high variability in sensor placement and the identification of fiducial points [114], [115]. Furthermore, inter-subject differences, such as age, body mass index (BMI), and posture, may introduce variability that complicates measurements' standardization and

generalizability across populations. SCG and GCG signals are also highly susceptible to motion artifacts, since external body movements can obscure cardiac-induced vibrations [116]. Moreover, while ML and signal processing techniques have improved fiducial point detection and artifact reduction, their effectiveness depends on large, high-quality datasets, which remain limited. As a result, the accuracy and consistency of SCG- and GCG-derived parameters still rely on filtering techniques, which may not always be feasible in real-time wearable applications.

3. Mechanically-Induced Strain:

SCG traditionally measured using accelerometers, can also be derived from strain sensors, with fiber Bragg grating (FBG) sensors being particularly suited for this application due to their high sensitivity to subtle vibrations. These sensors, when placed on the chest, detect the slight deformations of the chest wall caused by cardiac activity, making them a viable alternative for strain-based SCG (see Figure 1.11). FBG sensors reflect a specific wavelength of light, known as the Bragg wavelength (λB), which shifts in response to strain (ε) applied to the sensor [117]. By integrating these sensors into flexible matrices that adhere to the chest surface, cardiac-induced deformations can be effectively transduced into measurable shifts in λB, producing a strain-derived SCG signal. Currently, the use of strain-derived SCG from FBG sensors has been primarily focused on HR estimation, also using multipoint measurements [118]–[121]. While studies have demonstrated their effectiveness in this area, the feasibility of deriving fiducial points or conducting detailed waveform analysis from these signals has not yet been investigated. Additionally, their integration into wearable systems is challenging due to placement sensitivity, signal variability, and the need for bulky optical components, which may hinder real-time implementation.

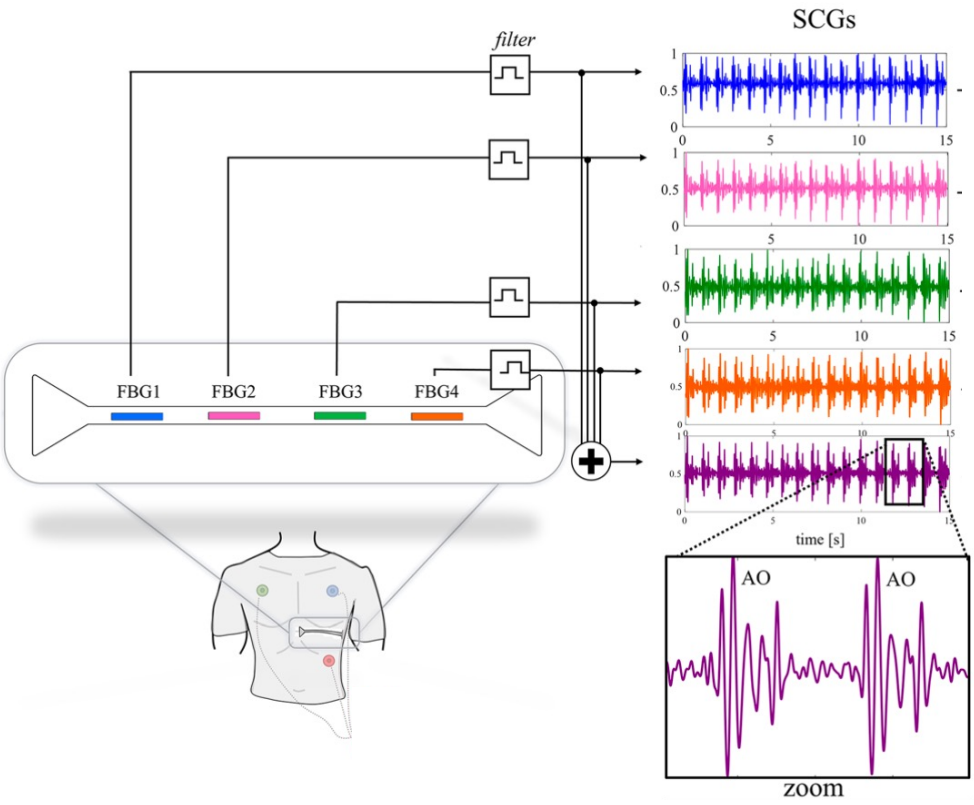

Figure 1.11. Schematic of a multi-point FBG sensing system for SCG measurement. Left: FBG array configuration and chest placement. Right: SCG signals from different measurement points with a detailed view of aortic opening (AO) events. Adapted from [121].

4. Blood Volume Changes (Photoplethysmography):

Monitoring changes in blood volume is another method to monitor the cardiac cycle non-invasively. This has been achieved through PPG, an optical sensing technique that has become increasingly popular in WDs [122]. PPG technology operates on the principle of light-tissue interaction, specifically exploiting the difference in light absorption between blood and surrounding tissues. This absorption variation changes dynamically during the cardiac cycle, due to the fluctuation of blood volume in the vessels.

A typical PPG sensor integrates light-emitting diodes (LEDs) as light sources and photodetectors as sensing elements. The LEDs emit light at specific

wavelengths, commonly red (~660 nm) and infrared (~900 nm), which penetrate the skin and interact with the underlying tissues. The photodetectors then measure either the reflected or transmitted light, depending on the sensor configuration. In reflection mode, both the LED and photodetector are placed on the same side of the tissue, making this configuration suitable for various measurement sites like the wrist or forehead. In transmission mode, the LED and photodetector are on opposite sides of the tissue, limiting this configuration to sites like the fingertip or earlobe, but potentially providing better signal quality.

The PPG signal comprises two main components with distinct physiological origins. The alternating current component represents the pulsatile variation in blood volume that occurs with each heartbeat, directly reflecting cardiac activity. This component typically constitutes 2-5% of the total signal amplitude and contains information about cardiac function and vascular properties. The direct current (DC) component, which makes up most of the signal, represents the relatively constant absorption from non-pulsatile arterial blood, venous blood, and surrounding tissues. This component varies slowly with respiration, thermoregulation, and vasomotor activity. A schematic representation PPG sensor and signal is reported in Figure 1.12.

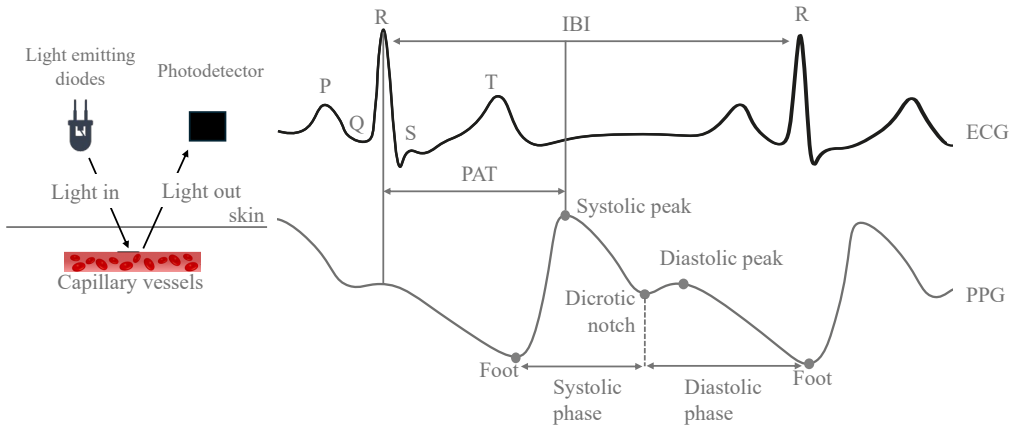

Figure 1.12. Schematic representation of PPG sensor (on left) and PPG signal (on right).

Through advanced signal processing techniques, PPG technology enables the extraction of various cardiovascular parameters. The fundamental

measurement is HR, derived from the frequency of the signal peaks. Also, HRV can be assessed through analysis of beat-to-beat intervals. Moreover, when multiple wavelengths are used, blood oxygen saturation (SpO2) can be calculated by exploiting the different absorption characteristics of oxygenated and deoxygenated hemoglobin. The combination of PPG with ECG enables the measurement of pulse transit time (PAT), which correlates with blood pressure [123].

Despite these capabilities, PPG measurements in WDs face several technical and physiological challenges. Motion artifacts affect signal quality, particularly during physical activity, as movement can alter the sensor-tissue interface and create noise [124]. The technology's performance is influenced by individual factors such as skin pigmentation, which affects light absorption, and tissue perfusion, which varies with temperature and cardiovascular status [125]. Environmental factors, including ambient light and temperature variations, can also impact measurement accuracy.

Modern WDs combine technologies like ECG with SCG and GCG to improve cardiac monitoring [126]. This integration allows for simultaneous tracking of electrical activity and mechanical function, offering a more complete assessment of heart performance. By linking electrical and mechanical events, these devices can better identify issues such as myocardial ischemia or valve problems. For example, combining ECG and SCG data helps detect cardiac cycle abnormalities, like valve timing or ventricular function changes.

1.5.2. Respiratory activity

WDs for respiratory monitoring are classified according to the measurand they are designed to capture [127]. Figure 1.13 presents an overview of the main sensing approaches:

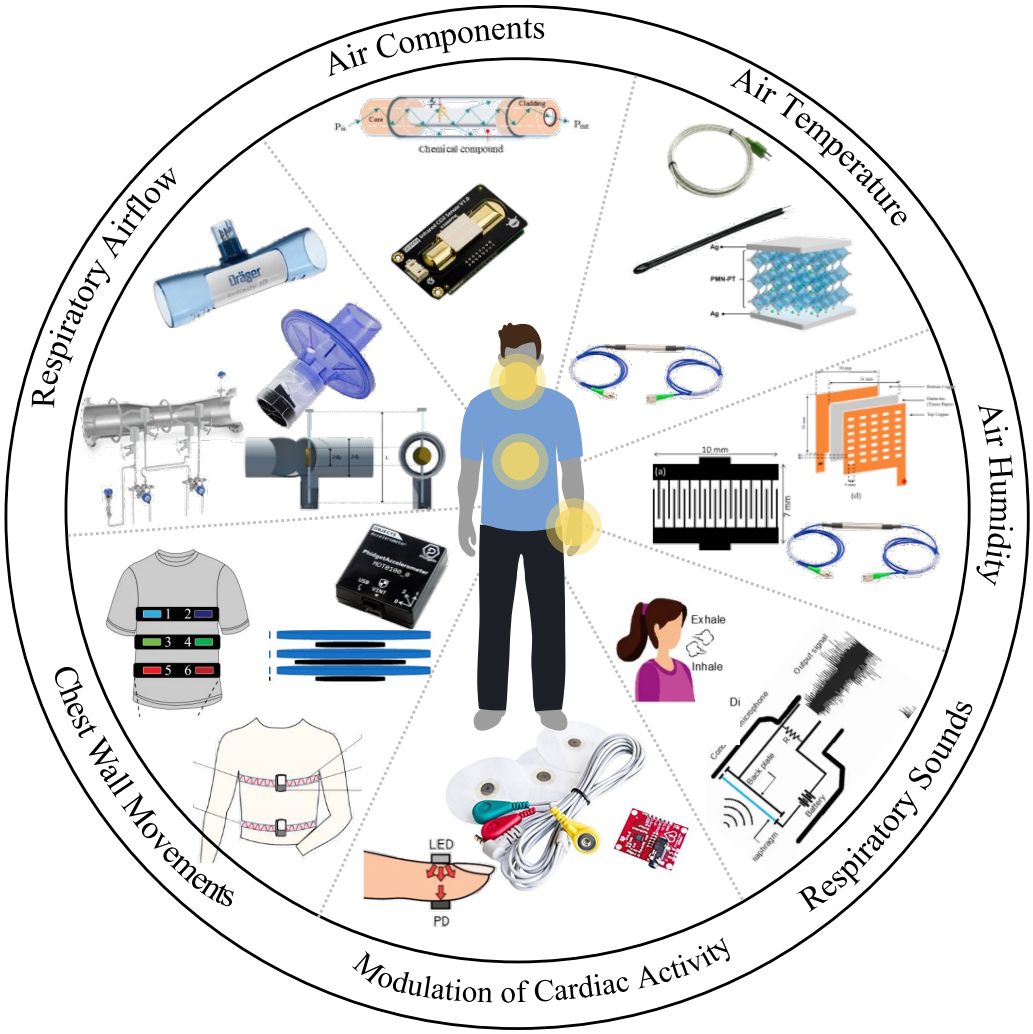

Figure 1.13. Overview of wearable solutions for breathing monitoring.

To quantify the prevalence of these sensing techniques in the scientific literature, Figure 1.14 presents the distribution of wearable respiratory monitoring technologies based on a Scopus search of peer-reviewed studies. The analysis provides information about which sensing approaches have been more extensively investigated and adopted in WDs for respiratory monitoring.

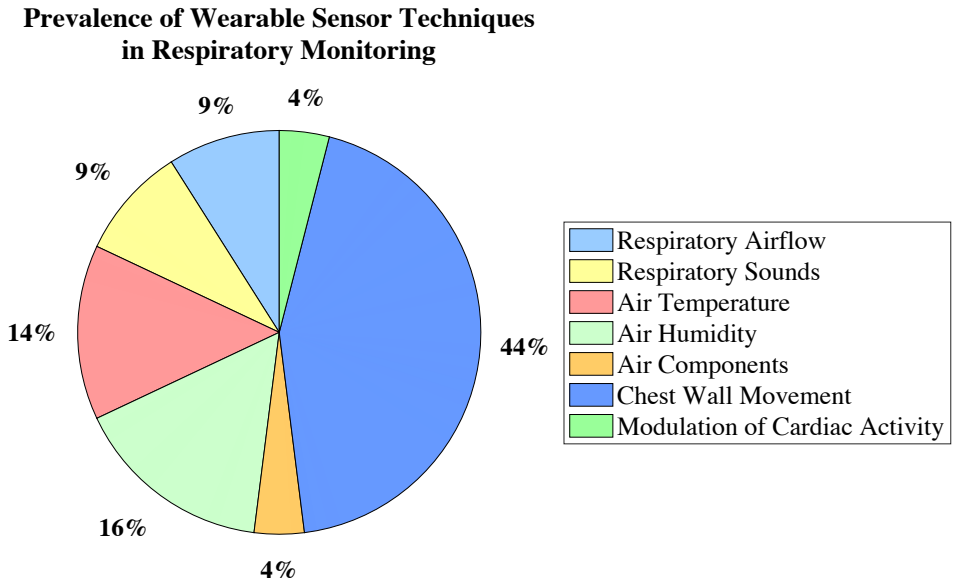

Figure 1.14. Prevalence of wearable sensor techniques in respiratory monitoring based on Scopus search results. The chart illustrates the distribution of different sensing approaches in wearable respiratory monitoring.

The pie chart illustrates the prevalence of different wearable sensor techniques for respiratory monitoring, categorized based on the type of physiological parameter they measure. Chest wall movement analysis (44 %) is the most studied technique, reflecting its widespread use in respiratory monitoring belts and strain sensors. This method is commonly used due to its non-invasiveness and ability to track breathing continuously. Air humidity (16 %) and air temperature (14 %) are also significant, suggesting a growing interest in breath analysis using environmental and gas sensors. These techniques are particularly relevant in the assessment of lung function, respiratory conditions, and exhaled breath characteristics. Respiratory sounds (9 %) and respiratory airflow (9 %) represent smaller portions, yet they remain useful in applications such as wearable stethoscopes, spirometry, and breath sound analysis for respiratory disease detection. Air component analysis (4 %) and modulation of cardiac activity (4 %) show the lowest prevalence.

The following is a brief description of the techniques listed above.

1. Techniques based on respiratory airflow

Airflow measurement technologies assess the volume and velocity of respiratory gases, enabling RR estimation. These sensors, typically integrated into facemasks or head-mounted devices, operate on different physical principles: i) differential flowmeters (DFs) measure pressure differentials generated across a resistive element. When airflow passes through this element (capillary tubes or wire meshes in pneumotachographs or fixed/variable orifices in orifice meters), it creates a pressure drop proportional to the flow rate [128]. These devices achieve response times in the tens of ms and measure flow rates from 0.1 $L \cdot min^{-1}$ to 100 $L \cdot min^{-1}$. While widely implemented also in medical devices, spirometers, and ventilators, their primary limitation stems from the additional breathing resistance they introduce, particularly significant in critical care and sports applications [129]; ii) turbine flowmeters, embedded in many spirometers and metabolic carts, measure airflow through the rotational speed of flat-bladed turbines, where angular velocity correlates directly with flow rate [130]. These devices have good dynamic response with rise times below 10 ms and maintain stability across varying environmental conditions, remaining unaffected by humidity and temperature fluctuations. Their robust performance have been demonstrated through validation in both clinical and sports science applications [131], [132]. However, these sensors present limitations due to their mechanical inertia, which can affect accuracy during rapid breathing pattern changes and may require periodic calibration due to mechanical wear; iii) hot wire anemometers (HWAs) detect airflow by measuring the cooling rate of an electrically heated wire, where the heat transfer rate correlates with air velocity [133]. These sensors achieve good dynamic responses with rise times under 1 ms and excel in detecting low flow rates, making them particularly suitable for pediatric applications. Despite their high sensitivity, HWAs present limitations in their fragile construction and require complex configurations to discriminate flow direction [134]; iv) fiber optic sensors (FOSs) represent an emerging technology in respiratory monitoring. These sensors detect airflow through

changes in optical properties, measuring variations in coupled light power caused by fiber bending from inhaled and exhaled air [135]. FOSs demonstrate good sensitivity, and show promising potential for monitoring diverse breathing patterns, including apnea and irregular respiration [136]. However, these systems require complex and expensive interrogation units, and their performance can be affected by external mechanical perturbations and temperature variations.

2. Techniques based on respiratory sounds

Acoustic sensors detect respiratory activity by measuring the sound waves generated during breathing. These devices employ microphones that transduce respiratory acoustic signals into electrical outputs [137]. The sensing can occur through two primary approaches: tracheal sound detection via sensors placed on the neck or chest [137] and direct airflow sound measurement through sensors positioned near the mouth [138]. Signal acquisition requires post-processing techniques to extract RR from the captured waveforms, particularly in noisy environments. While these sensors demonstrate effectiveness in controlled hospital settings, they present several limitations. Their performance is affected by ambient acoustic interference and exhibits high sensitivity to sensor placement. Additionally, the requirement for sensor positioning near sound generation sites (mouth, nose, or trachea) constrains their implementation primarily to facemasks or adhesive patches on the face and neck.

3. Techniques based on air temperature

Temperature-based respiratory monitoring exploits the thermal gradient between exhaled and ambient air, typically around 15°C [139]. This approach employs various sensing technologies, each based on different physical principles for temperature measurement. Thermistors function through temperature-dependent resistance changes, categorized as negative temperature coefficient (NTC) or positive temperature coefficient (PTC) devices. Their

behavior follows the Steinhart-Hart equation [130]. These sensors have advantages like affordability, simplicity, and accuracy.

Thermocouples operate based on the Seebeck effect, generating a voltage proportional to temperature differences between junctions of dissimilar metals [130]. With response times of approximately 0.5 s, they are suitable for capturing high RR values.

According to the Stefan-Boltzmann law, pyroelectric sensors detect temperature variations through changes in material polarization, producing charge outputs proportional to temperature change rates [140]. These devices achieve high accuracy (±1°C) with rapid response characteristics, particularly in microfabricated forms. Their adaptable design configurations, including cylindrical and thin-film formats, enable integration into face masks and nasal monitoring devices [141]. However, these sensors respond to temperature changes rather than absolute temperature values, making it difficult to detect very slow breathing patterns or apnea events where the temperature changes are gradual.

FBG sensors measure temperature through shifts in Bragg wavelength, exhibiting good response times (10 ms) and sensitivity (10 pm/°C) [142]. They offer advantages including small size (250 μm diameter), lightweight, and biocompatibility. However, their implementation faces challenges, including mechanical strain sensitivity and the requirement for bulky interrogation systems [143].

4. Techniques based on air humidity

Respiratory monitoring can exploit the difference in water vapor content between inhaled and exhaled air through relative humidity (RH) sensors. This approach leverages the fact that exhaled air is saturated with vapor (RH = 100%) at body temperature, while inhaled air varies with environmental conditions (RH = 40–80%) [144]. Capacitive sensors operate by detecting changes in

capacitance due to variations in the dielectric properties of hygroscopic materials between electrodes [145]. These sensors demonstrate good linearity, with an accuracy of approximately 3% and response times ranging from seconds to milliseconds [145]. However, their performance can degrade over time due to contamination and aging of the hygroscopic material, affecting long-term measurement stability. Resistive sensors measure RH through changes in electrical impedance [145]. With response times as low as 37 ms, they can track RR at high frequencies (up to 240 brpm) and have been validated for apnea detection and real-time monitoring [146]. However, these sensors exhibit temperature dependence, requiring additional compensation circuits for accurate measurements. FOSs utilize polymer or nanoparticle coatings that respond to RH through water vapor absorption or desorption, inducing changes in optical properties [147]. These sensors demonstrate good performance in controlled and clinical environments, with response times from tens of milliseconds to seconds and errors below 2% compared to reference systems [148]. However, the polymer coatings can experience hysteresis[1] effects during rapid humidity changes, potentially affecting measurement accuracy during irregular breathing patterns.

5. Techniques based on air components

CO_2 sensors measure RR by detecting the concentration difference between inhaled (0.04%) and exhaled (up to 6%) air during breathing [146]. Two main technologies use this approach: infrared sensors and FOSs.

1. *Hysteresis refers to the phenomenon where the indication of a measuring instrument depends not only on its current input but also on its history of past inputs. The instrument may provide different readings for the same measured value, depending on whether that value was approached by increasing or decreasing the input. Hysteresis error refers to differences in the measured value between an upscale sequential test and a downscale sequential test. Hysteresis is usually specified for a measurement system in terms of an uncertainty based on the maximum hysteresis error as a percentage of the full-scale output* [149].

Nondispersive infrared (NDIR) sensors operate based on the Beer-Lambert Law, measuring CO_2 absorption in the infrared spectrum. These sensors achieve high accuracy (±0.3% CO_2) with response times below 100 ms [150].

While they provide precise measurements, NDIR sensors present several implementation challenges: they require regular calibration, warm-up periods, and auxiliary components such as filters and pumps. Their power consumption and form factor also limit their application in portable devices. FOSs employ near- or mid-infrared light for CO_2 detection through absorption principles. Configurations like optical fibers with gas cells, demonstrate high precision (±0.3%) and minimal invasiveness [151]. However, these sensors often the interrogation system, and their sensitivity can be affected by fiber bending during measurements. Both technologies also share a common limitation: their performance is affected by environmental factors such as humidity and temperature variations.

6. Techniques based on chest wall movement analysis

These approaches capture the cyclic movements of the chest wall that occur during breathing, tracking its expansion and contraction. Different sensing technologies have been proposed at this aim, each using different principles to convert respiratory mechanics into measurable signals. Among them, piezoresistive sensors are based on the resistance changes due to strain. These sensors are often integrated into textiles using conductive polymers or yarns but may experience durability issues, such as performance degradation after washing, and sensitivity to motion artifacts [152]. Capacitive sensors placed on the chest detect changes in permittivity between electrodes caused by inhalation and exhalation. These sensors offer high accuracy (e.g., −0.14 brpm in COPD patients [153]). Flexible electrode designs improve body movement adaptability, but maintaining electrode contact remains an issue for signal quality [154]. Inductive sensors, commonly embedded in elastic bands, monitor changes in thoracic inductance caused by respiratory movements. These sensors are used in

systems like T-shirts and are validated across various postures and activities, with good agreement to reference methods [155]. However, their performance depends on maintaining consistent contact with the body. Loose or shifting elastic bands can introduce measurement errors. FOSs, particularly FBGs, typically embedded into polymers can measure respiratory-induced chest wall deformations with rapid response times (~10 ms), making them suitable for monitoring rapid or small chest wall movements. These sensors can be integrated into textiles or chest strap and can embed multiple FBGs. They achieved biases of −0.02 brpm when compared to motion capture systems during quiet breathing [156], [157]. Transthoracic impedance sensors measure thoracic electrical impedance changes due to variations in air volume during inhalation and exhalation. They provide a nearly linear relationship between impedance and respiratory volume, enabling RR monitoring across different postures and activities [158]. Motion sensors, including accelerometers, gyroscopes, and magnetometers, capture chest wall dynamics such as acceleration, angular velocity, and magnetic field changes. They have been used for RR monitoring in stationary conditions [159]. However, error rates increase during physical activity, such as running or walking, due to motion artifacts [106], [152], [159]–[161]. While strain and motion sensors demonstrate good potential for unobtrusive respiratory monitoring, non-respiratory movements often affect them. Hybrid solutions combining multiple sensor types can improve robustness by distinguishing between respiratory and unrelated motion [162].

7. Techniques based on the modulation of cardiac activity

RR can also be estimated using cardiovascular signals that exhibit respiratory-related variations. By analyzing periodic signal modulations in cardiac measurements, RR can be extracted through spectral analysis or tracking amplitude variations [163], [164]. Among all, ECG and PPG sensors are the most used. ECG sensors allow the collection of the heart's electrical activity, with signal modulations caused by respiratory effects such as baseline wander, amplitude modulation, and respiratory sinus arrhythmia (RSA) [165].

Techniques like ECG-derived respiration and RSA-based methods enable RR estimation, with validation studies showing errors of about 2 brpm during sleep and about 0.5 brpm in daily-life activities [166], [167]. While promising, ECG performance is affected by signal quality degradation during exercise [165]. On the other hand, PPG sensors employ light-based measurement principles to detect blood volume changes in peripheral tissues [168]. Respiratory modulations in PPG include amplitude changes, frequency shifts, and baseline wander caused by intrathoracic pressure variations [163]. Although validated in structured environments with biases below 0.07 brpm during quiet breathing [169], PPG performance declines with motion artifacts and poor sensor attachment [170]. Both ECG and PPG are favored for their low invasiveness, cost-effectiveness, and integration into wearable systems, but challenges such as sensitivity to motion and environmental factors limit their use in dynamic settings.

1.6. Key factors influencing wearable design

WDs for physiological monitoring require careful design that considers technical performance, user comfort, and application context [171]. Hence for their development sensor placement, material selection, and algorithms should be considered to ensure reliable measurements across different application environments [172].

Sensor placement is one of the most critical aspects influencing device performance and user experience. The chest and the wrist are typically the preferred locations for wearable sensors, particularly for breathing and cardiac monitoring [173]. Among the preferred locations, wrist-worn wearables are often selected for their comfort and ease of use, while the chest location is required for specific measurements. For example, accelerometers and gyroscopes to detect cardiac activity must be positioned on the chest wall to measure heart mechanics [174]–[176]. Moreover, this location allows the realization of WDs such as smart vests or shirts, enabling unobtrusive

measurements. However, chest placement is not always practical in dynamic environments like sports, where intense motion can cause considerable artifacts [174]. In these cases, alternative sensor placements must be considered. For example, sensors integrated into headphones, masks or similar accessories for breathing can directly measure airflow, avoiding the motion-related challenges inherent to chest-mounted devices. Similarly, peripheral locations like the wrist or ankle may be suitable for activity-related metrics. However, they often require compensation techniques to address the increased susceptibility to noise and motion disturbances [177].

Even with thoughtful sensor placement, recorded signals can still be affected by movement and environmental factors can still affect recorded signals. As a result, algorithms are needed to process data, manage noise, and extract relevant information [178]. For example, sports and daily life applications require adaptive algorithms capable of dynamically adjusting to changes in activity or environmental conditions. For this reason, in recent years, advancements in ML techniques have improved algorithms' adaptability and robustness [179]–[181]. These methods enable devices to tailor data processing to each person's physiology and activity level. While these considerations can improve reliability and measurement accuracy even under less controlled conditions, it is equally important to consider the computational overhead of these approaches, particularly in WDs where power and processing resources may be constrained [182]. For this reason, another option is to include multiple sensors to provide complementary information and enhance data reliability. This approach allows for a better understanding of physiological signals and movement patterns, mitigating the impact of artifacts. In this context, sensors capable of simultaneously measuring multiple parameters, such as physiological signals and movement, offer a promising solution. By combining data streams from a single sensor, these devices can reduce hardware complexity, enhancing the quality of the information provided.

1.7. Ph.D. candidate contribution

This Ph.D. thesis investigates the development of wearable monitoring systems for cardiac and respiratory monitoring across multiple application domains. The research objectives encompass the design, development, implementation, and experimental validation of wearable monitoring systems, with particular emphasis on their performance in non-laboratory conditions. The research exploits IMU sensors, textile-integrated sensors, and temperature-based sensing systems to acquire physiological parameters in daily life, clinical, and sports contexts.

The thesis is organized into this introductory chapter and four additional chapters, as described below:

Chapter 2 focuses on the design and evaluation of IMU-based and textile-based sensors for cardiac and respiratory monitoring in daily life. The chapter examines the impact of sensor positioning and configuration on measurement accuracy, as well as the development of a textile-based system for unobtrusive respiratory monitoring.

Chapter 3 explores the application of IMU-based solutions for cardiac monitoring in clinical contexts. It investigates the potential of these sensors for HRV extraction and their use in classifying patients with AS, emphasizing their clinical relevance.

Chapter 4 presents wearable systems for respiratory monitoring in sports science. It includes the design and experimental validation of a smart facemask, as well as the development of algorithms for RR estimation and motion artifact removal.

Chapter 5 summarizes the main findings of the thesis, highlighting the contributions to wearable technology for health monitoring and outlining potential directions for future research and development.

This thesis explores various wearable monitoring solutions, each tailored to meet the requirements of specific application contexts. Overall, this work addresses the challenges of moving from controlled laboratory conditions to real-world implementations by emphasizing the need for context-driven device configurations.

2

Chapter 2: Wearable Sensors for Cardiac and Respiratory Monitoring in Daily Life

2.1. Introduction

Among WDs for cardiac and respiratory monitoring, torso-worn devices have emerged as particularly effective in daily life environments due to their proximity to the heart and lungs and their non-intrusiveness [128]. By detecting thoracic deformations, these devices monitor respiratory and cardiac activities through periodic chest movements and subtle mechanical changes from heartbeats. In this context, IMU sensors represent a versatile and cost-effective option [183], [184]. Their ability to monitor both HR and RR, alongside physical activity, makes them particularly suitable for dynamic, real-life environments. Similarly, textile-based sensors offer a promising alternative, leveraging their ability to integrate into clothing, providing non-invasive and continuous monitoring, ideal for long-term use. [185], [186].

This chapter explores the applicability of IMU-based and textile-based sensors in daily life contexts. It examines the influence of IMU positioning and configuration on data accuracy, and their potential for simultaneous HR and RR monitoring. Moreover, the design and development of textile sensors embedded in a T-shirt for respiratory monitoring is presented.

2.2. IMU-based physiological monitoring

IMUs are used in WDs due to their ability to capture both cardiac and respiratory signals alongside physical activity data. The following sections examines how sensor positioning and configuration affect data accuracy, aiming to identify the most effective setup for physiological monitoring in daily life scenarios.

2.2.1. IMU sensors for cardiac and respiratory monitoring

IMU sensors, integrating accelerometers and gyroscopes, enable the simultaneous monitoring of cardiac and respiratory activity by detecting chest wall deformations. The respiratory signal, characterized by low-frequency oscillations, modulates the higher-frequency cardiac signal, allowing the extraction of information about both activities from a single device. The capability of monitoring both activities offers an advantage, particularly in daily life applications, where non-intrusive and compact monitoring systems are required.

Accelerometers have been used to measure thoracic wall motion, enabling the estimation of RR [159] as well as the identification of HR and cardiac mechanical events associated with different phases of the cardiac cycle [187]. Some studies have even explored their application in postures resembling those encountered in daily life [188], [189]. Gyroscopes, though relatively newer in this context, have been proposed for estimating cardiac parameters such as HR and valve opening/closure events [175]. However, their use for RR estimation is limited, and only a few studies have demonstrated their capability to capture respiratory signals [190]. When combined with accelerometers, gyroscopes enhance signal robustness and broaden the range of measurable physiological parameters, particularly for cardiac activity [189], [191]. Despite these advancements, several critical challenges limit the widespread adoption of SCG and GCG in real-world applications. A major limitation is the lack of standardized sensor placement, which impacts signal quality and consistency.

Studies have investigated various anatomical locations, such as the sternum [191]–[194], xiphoid process [100], [111], [195]–[197], and intercostal spaces [198], [199], but no consensus has been reached regarding the optimal placement for reliable data acquisition [200], [201]. Additionally, for both cardiac and respiratory activity, the dorsoventral axis (z-axis) of accelerometers and the vertical axis (y-axis) of gyroscopes are commonly cited as the most responsive [100], [176], [191], [194], [202]. However, these preferences are based on limited evidence, and no studies have systematically investigated or validated the optimal axes for signal acquisition across different conditions and applications.

Another challenge is the restricted scope of experimental conditions in existing research. Most studies are conducted in controlled laboratory environments, often focusing on static postures such as supine or seated positions [183], [203]. This approach neglects the dynamic and varied conditions of daily life, where individuals frequently change posture, engage in physical activities, or encounter external motion artifacts. These factors influence signal acquisition and processing, particularly for respiratory monitoring, where breathing patterns and chest wall dynamics vary widely. The effects of postural changes on most reliable axis and sensor location on the chest wall remain also underexplored, leaving a gap in understanding the robustness of SCG and GCG signals in real-world scenarios.

2.2.2. Evaluating sensor position and its impact on data accuracy using accelerometers

Building on the challenges discussed earlier, the reliability of cardiac and respiratory signal monitoring is closely linked to the mechanical patterns of these signals and the anatomical location of the sensor [204]–[206]. Sensor placement on the chest influences signal quality, determining its susceptibility to motion artifacts and postural changes, which can distort the recorded information [204]. Identifying the optimal placement and axis is thus necessary to ensure accurate and consistent measurements of both HR and RR under varying conditions.

While most studies have placed inertial sensors on the xiphoid process and a limited set of alternative locations, there is no consensus on the most effective configuration for simultaneous monitoring of HR and RR [101]. Furthermore, the effects of postural changes on signal quality are still poorly explored and a generic configuration capable of maintaining high performance in different postures and activities has not yet been established.

The following section will investigate various sensor locations of the chest to assess their effectiveness in monitoring HR and RR across typical daily life postures. This analysis aims to advance the development of WDs in different real-world scenarios.

Methodology

The study utilized a multi-sensor system consisting of five IMUs (Xsens DOT, Xsens, Netherlands), each integrating a triaxial accelerometer (full scale ±16 g, sampling frequency 120 Hz). The sensors were placed at five chest locations: the auscultation points of the aortic valve (AV), tricuspid valve (TV), pulmonary valve (PV), mitral valve (MV), and the xiphoid process (X), as represented in Figure 2.1. These positions were selected for their repeatability in positioning being of the points used in clinical practice for auscultation and for their potential to capture both cardiac and respiratory signals. IMUs were attached directly to the participants' skin using hypoallergenic adhesive tape to ensure stable contact with the chest wall and minimize motion-related artifacts. The Zephyr Bioharness 3.0 (Medtronic, USA) was used as a reference system for acquiring ECG signals and respiratory waveforms, sampled at 250 Hz and 25 Hz, respectively.

Fifteen healthy volunteers (10 males, 5 females; mean age: 26.1 ± 2.3 years; height: 174.6 ± 10.6 cm; body mass: 70.4 ± 3.0 kg) participated in the study. All participants had no history of cardiovascular or respiratory diseases. Ethical approval was obtained (protocol number ST-UCBM27/18 OSS), and informed consent was secured from all participants. The experimental protocol included

six activities, each lasting 130 s: sitting, lying, standing, walking at a natural pace, climbing stairs, and standing post-exercise. Climbing stairs phases were excluded from the HR and RR analysis, used only to assess these physiological parameters after physical activity. Linear accelerations along the x- y-, and z-axes were recorded simultaneously from the IMUs, while ECG and respiratory waveforms were collected using the reference chest strap.

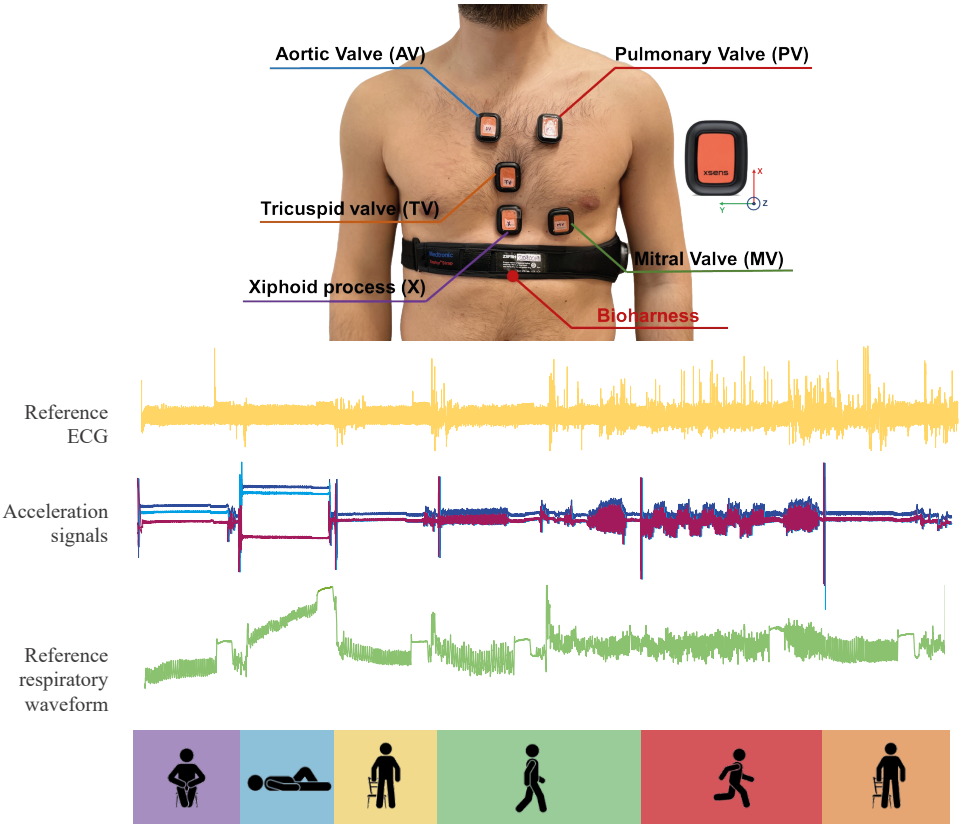

Figure 2.1: Schematization of experimental setup and protocol. Adapted from [207].

The collected accelerometer data were analyzed offline in MATLAB® with three main objectives: i) to calculate the best axis and sensor position, and to identify an optimal general-purpose configuration that performs robustly across all postures and subjects, ensuring reliable monitoring of HR and RR in diverse conditions; ii) to compare the performance of the general-purpose configuration with a posture-dependent configuration, where the optimal sensor position and axis are determined separately for each posture; iii) to validate HR and RR estimates obtained from accelerometer data against the reference values.

Different signal pre-processing was carried out to extract cardiac and respiratory activity. To extract cardiac information, a continuous wavelet transform (CWT) band-pass filter between 10 Hz and 40 Hz was applied to preserve the frequencies related to the heartbeat [98], followed by Hilbert envelope extraction and additional filtering (0.7–3 Hz) to emphasize AO events and ensure the preservation of HR frequencies between 42 bpm and 180 bpm, which typically fall within the physiological resting range in non-exertional conditions. For respiratory signals, low-frequency components (0.05–1 Hz) were isolated through a Butterworth band pass filter to capture thoracic expansions and contractions [208]. A schematization of the main steps carried out for signal processing is reported in Figure 2.2.

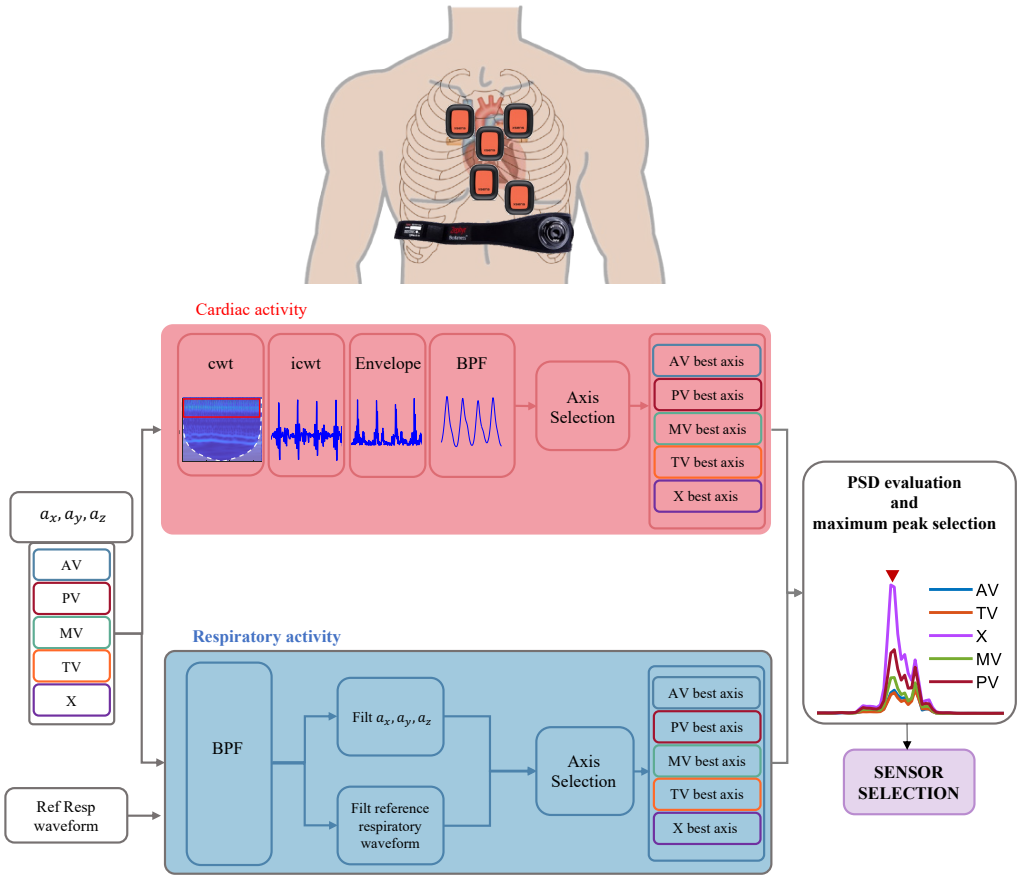

Figure 2.2: Overview of the data processing pipeline for axis and sensor selection in cardiac and respiratory monitoring. Adapted from [207].

For cardiac activity, the most informative sensor axis and position were identified by calculating the normalized power spectral density (PSD) and selecting the combination with the highest PSD peak. For respiratory activity, the best axis was determined by calculating the correlation coefficients between filtered acceleration signals and the reference respiratory waveform, followed by PSD analysis to identify the optimal sensor position. The position that showed the highest power was selected. The overall optimal sensor position and axis were defined as the most recurrent combination across all subjects.

Two configurations were analyzed: the posture-dependent configuration and the general-purpose configuration. The posture-dependent configuration determined the optimal sensor placement and axis for each posture separately, considering how different postures affect the mechanical properties of the chest wall and the resulting signals. The general-purpose configuration identified a single sensor placement and axis that performed well across all postures, making it applicable to real-world applications involving changes in posture and activity.

HR and RR were then estimated using the configuration selected from the accelerometer signals. To account for motion artefacts, the analysis was adapted according to the activity level during testing. The activity level was quantified using the vector magnitude unit (VMU), which represents the overall magnitude of body movements. The VMU was calculated as the square root of the sum of the squared accelerations along the three axes, as follows:

$$VMU = \sqrt{a_x^2 + a_y^2 + a_z^2} \tag{2.1}$$

where a_x, a_y, a_z are the accelerations along the x-, y-, and z-axes. Thresholds were defined to classify activities as low (resting, VMU < 0.2 g), medium (walking, 0.2 g ≤ VMU < 0.8 g), or high (dynamic, VMU ≥ 0.8 g), where g is the standard gravitational acceleration, equal to 9.81 m/s^2. For low-activity levels, HR was estimated by identifying consecutive AO peaks in the signal, representing individual heartbeats. The time intervals between these

peaks were calculated, and HR was derived as the inverse of the intervals, multiplied by 60 to express the value in beats per minute (bpm). Similarly, RR was estimated by detecting the local maximum peaks corresponding to the end of inhalation, which mark each respiratory cycle. The time intervals between these peaks (defined as breathing intervals, TR) were measured and the RR was calculated as the inversion of the TRs, multiplied by 60, to obtain the value in brpm. For the reference system, the ECG signal was processed using a modified Pan-Tompkins algorithm to detect R peaks [209]. Then, HR was calculated as the inverse of the R-R interval (the time between consecutive R peaks) multiplied by 60. Regarding the respiratory activity assessment, the respiratory waveform was analyzed using a time-domain peak detection algorithm. The local maxima, corresponding to the end of inhalation, were identified, and RR was calculated as $60/TR$, where TR is the time between consecutive end-inspiratory peaks.

For medium- and high-activity levels, frequency-domain analysis was used to suppress noise caused by body movements and emphasize the physiological signals. The accelerometer and reference data were segmented into 30-s moving windows with a 1 s shift (29 s overlap). The PSD was computed within each window, and the frequency corresponding to the maximum PSD peak was identified. For both HR and RR, this peak frequency was multiplied by 60 to estimate the average rate (in bpm or brpm) for the respective window.

The HR and RR values estimated from the accelerometer signals were compared to those obtained from the reference system to evaluate the accuracy of the proposed IMU-based monitoring approach. Performance was assessed using the mean absolute error (MAE), mean absolute percentage error (MAPE), and the mean of differences (MOD) with limits of agreement (LOAs) determined through Bland-Altman analysis.

Results

Results showed that, among the three axes, the z-axis was the most informative for cardiac and respiratory monitoring across all postures and activities. In fact, for cardiac activity, the z-axis was selected in 80% of cases in the general-purpose configuration, highlighting its sensitivity to dorsoventral accelerations caused by heartbeats. For respiratory activity, the z-axis was also the most effective, with a selection frequency of 47% in the general-purpose configuration. The detailed results for axis and sensor selection in cardiac and respiratory monitoring are shown in Figure 2.3.

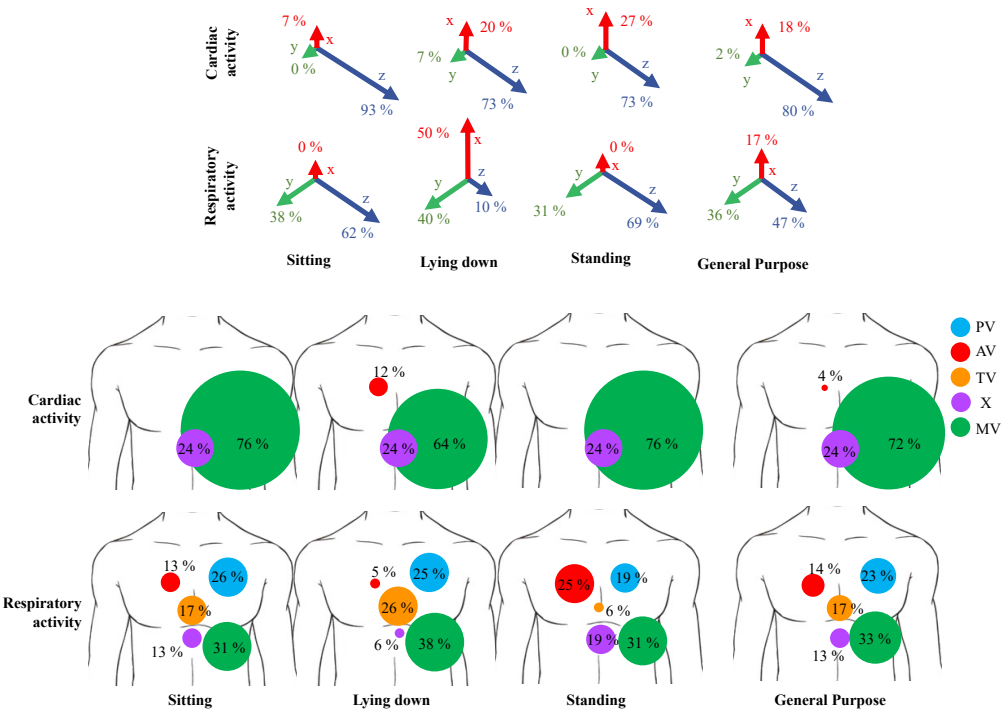

Figure 2.3: Results of axis and sensor selection for cardiac (top) and respiratory (bottom) activity. Percentages for sensor selection indicate the proportion of subjects for whom each sensor position performed best, while percentages for axis selection reflect the overall performance of each axis across all sensor positions and subjects. Standing includes both pre- and post-exercise conditions. Adapted from [207].

For sensor positions, the MV region showed the highest power in the PSD for both cardiac and respiratory signals. In the general-purpose configuration, the MV position was identified as optimal in 72% of cases for cardiac activity and 33% for respiratory activity. Its proximity to the left ventricle and sensitivity

to mechanical vibrations generated by the heart and lungs contributed to its superior performance. In contrast, the X position, often cited in the literature for cardiac signal extraction, had a much lower selection frequency (24% for cardiac activity), likely due to its suboptimal placement relative to the physiological signal sources.

The general-purpose configuration, consisting of the MV position and the z-axis, showed good agreement with the reference system for both HR and RR estimation. Across all activities, the MAE remained below 1.5 bpm for HR and 4 brpm for RR (see Figure 2.4). Bland-Altman analysis further confirmed the robustness of this configuration, with a MOD close to zero under all conditions. While, for HR, the LOAs ranged within ±4 bpm during static conditions, such as lying down, and increased to ±6 bpm during walking. For RR, the LOAs ranged from more than ±5 brpm during resting activities to about ±10 brpm during dynamic conditions.

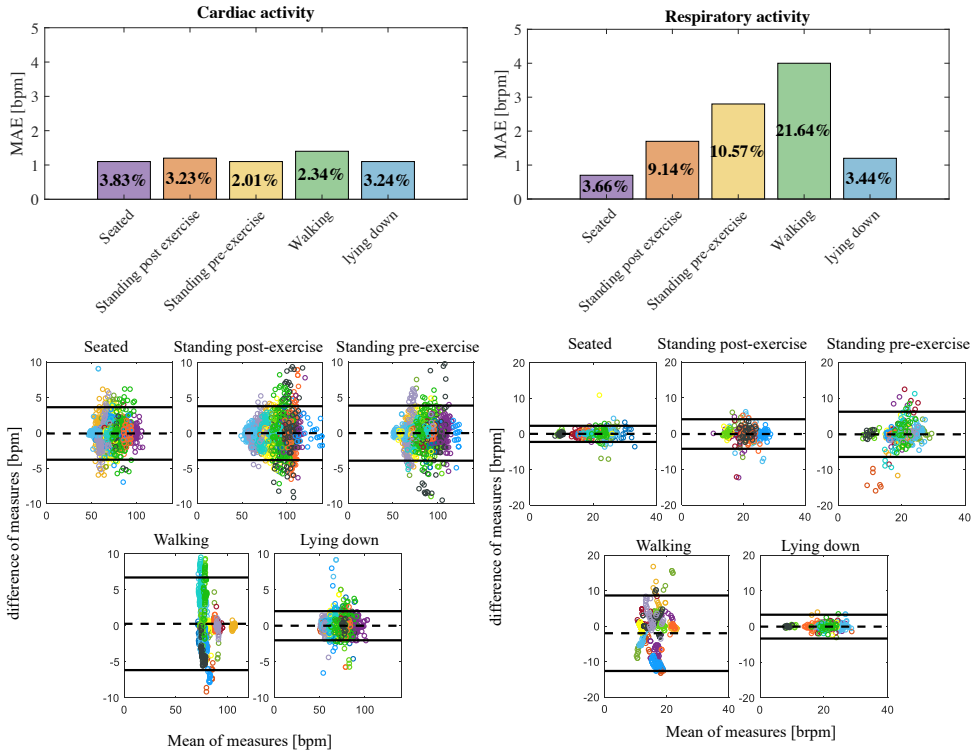

Figure 2.4: MAE values for HR (left) and RR (right) estimation across different activities. The values within the bars indicate the MAPE values for each posture. In the bottom panels the Bland-Altman plot is reported per each posture. Different colors represent different subjects. Adapted from [207].

While the general-purpose configuration provided good performance, the posture-dependent configuration showed slight advantages in specific scenarios, as illustrated in Figure 2.5. For RR, posture-dependent setup improved accuracy during standing and walking by reducing noise and motion artifacts through optimized sensor placement and axis selection. These adjustments led to lower MAEs, with differences of up to 1 brpm compared to the general-purpose. For HR, the general-purpose configuration performed equally well as the posture-dependent configuration, with MAEs below 1.5 bpm across all conditions. This result underscores the robustness of the MV-z combination for HR monitoring, regardless of posture.

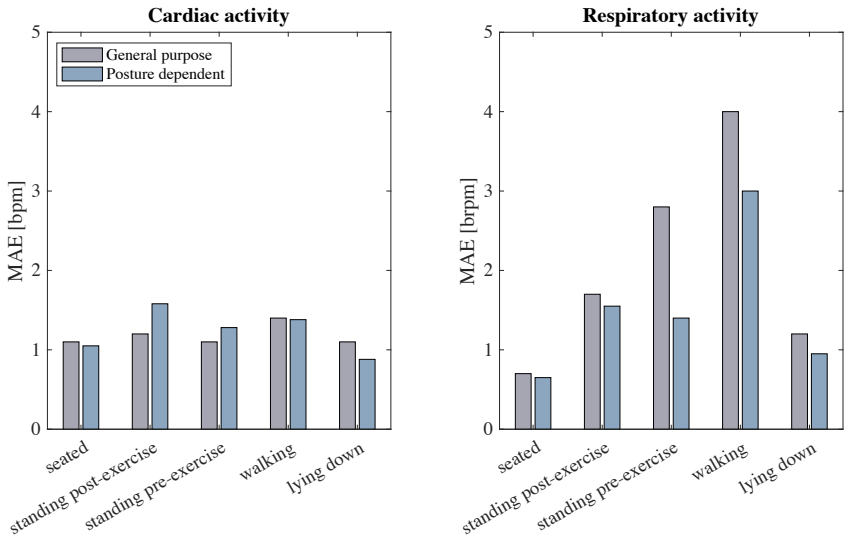

Figure 2.5: Comparison of MAE between the general-purpose and posture-dependent configurations for HR (left) and RR (right) estimation across different activities. Adapted from [207].

This study's findings highlight the importance of sensor placement and axis selection in optimizing IMU-based systems for simultaneous monitoring of HR and RR. The MV-z combination consistently provided the highest signal quality and accuracy for both parameters in all postures. The general-purpose configuration proved to be an effective solution for real-world applications, particularly in scenarios with frequent posture changes. While the posture-dependent configurations offered improvements for RR in dynamic postures, they did not significantly improve HR monitoring, confirming the reliability of the general-purpose approach.

Discussion

The study examined the use of IMU sensors placed at five chest locations for monitoring both HR and RR, proposing a generic configuration that identifies the sensor position on the MV and on the dorsoventral axis (z-axis) as the most informative. This result aligns with previous evidence indicating that the mechanical activity of the heart particularly influences the dorsoventral axis [101], [109], [210] but contrasts with studies that often suggest the X location as the preferred position [109]. The proposed configuration stands out for its ability

to use a single sensor for both functions, surpassing the traditional approach that requires multiple devices [106], [211], [212].

Regarding HR monitoring, the results showed that MAE was lower than that of previous studies. For example, the errors observed in [213] for similar configurations were ±10 bpm, while in [214] the use of an accelerometer on the AV area during walking and resting yielded less accurate results compared to those obtained in this study. This demonstrates the effectiveness of the general-purpose configuration, which complies with the accuracy limits required for medical devices (<5 bpm) [215]. For RR monitoring, the results obtained with the general-purpose configuration are comparable to those of previous IMU-based studies; however, they remain suboptimal. Posture had a notable impact on performance, particularly for RR. Specifically, seated and lying postures provided promising results, while standing and walking conditions negatively impacted estimation errors. In these dynamic scenarios, the posture-dependent configuration was beneficial for RR monitoring but did not provide notable advantages for HR.

This study contributes to the existing literature by offering clear guidance on the choice of sensor axis and position for cardiorespiratory monitoring with IMU. The proposed configuration demonstrates that a single-sensor approach can achieve accurate estimates under static and dynamic conditions, reducing complexity compared to multi-sensor technologies.

2.2.3. Influence of sensor configuration on measurement using accelerometers and gyroscopes

After identifying the optimal positioning of the chest for simultaneous monitoring of cardiac and respiratory activity, the analysis focused on the type of sensor. Specifically, we compared the performance of accelerometers and gyroscopes integrated in the same IMU system to determine which sensor technology offers superior accuracy for monitoring these two physiological

activities. In addition, we analyzed the influence that the algorithm used to extract the physiological parameter of interest has on performance. Using a frequency-domain approach in moving windows, the influence of the length of the window used for the extraction of HR and RR on the results was evaluated.

Methodology

To compare the performance of accelerometers and gyroscopes for cardiac and respiratory monitoring, the same IMU sensor from the previous section was used. This IMU integrates a tri-axial accelerometer (full scale: ±16 g) and a tri-axial gyroscope (full scale: ±2000°/s). The sensor was positioned at the fifth left intercostal space along the midclavicular line, anatomically corresponding to the MV region, as identified in the previous study. An example of the experimental setup is shown in Figure 2.6. The Zephyr BioHarness wearable chest multiparametric device was employed as the reference system to validate HR and RR estimates obtained from the IMU sensor. Data were collected from 11 healthy participants who performed three static postures: sitting, standing, and lying down. Each posture was maintained for two minutes while participants were instructed to breathe quietly. IMU data were sampled at 120 Hz and stored for offline processing. The study was conducted in compliance with the Declaration of Helsinki, and the design was approved by the Ethical Committee of the University Campus Bio-Medico di Roma (approval code: 27.2(18).20, dated 15 June 2020).

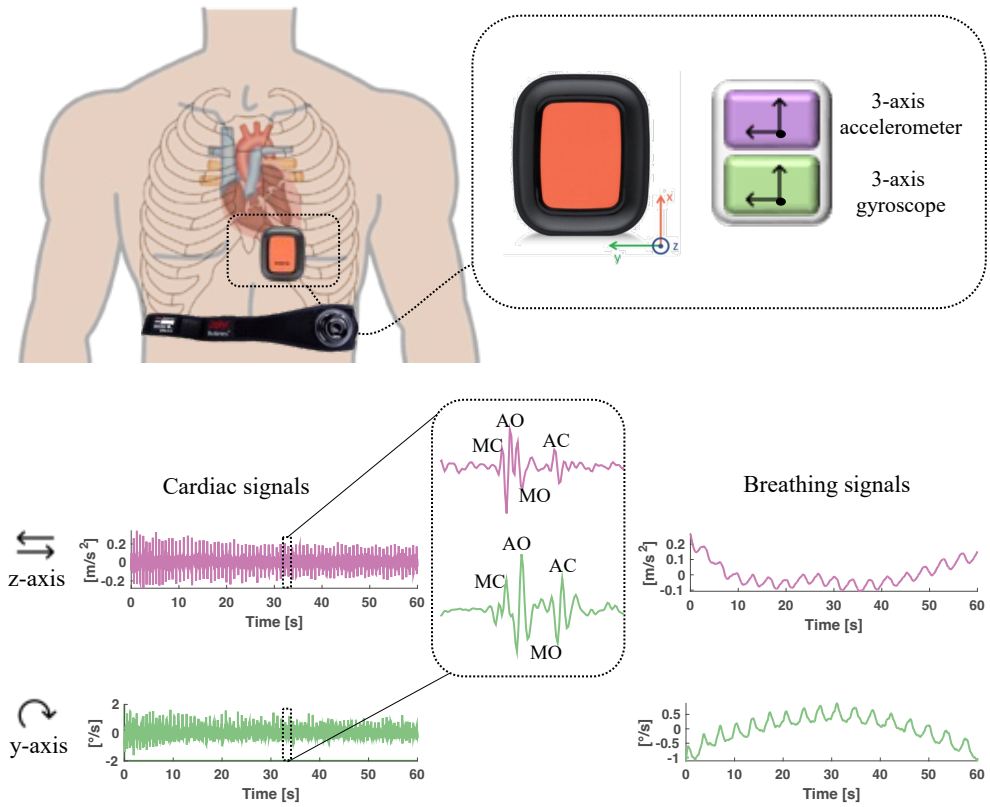

Figure 2.6: IMU sensor positioning on the subject's chest. Filtered accelerometer and gyroscope signals isolating the cardiac and respiratory components. Adapted from [216].

The raw data collected by the IMU sensor included acceleration and angular velocity signals from the chest. The z-axis of the accelerometer and the y-axis of the gyroscope, identified as the most informative axes for both cardiac and respiratory monitoring, were selected for analysis [176], [217], [218]. The pre-processing steps outlined above were applied to extract the filtered envelopes of the SCG and GCG signals and the filtered respiratory signals from both accelerometer and gyroscope data. The reference signals were also processed using the same methodology described in the previous study.

To ensure robustness against motion artefacts, a frequency domain approach in moving windows was adopted to estimate HR and RR. This method exploits the spectral characteristics of cardiac and respiratory signals to minimize the influence of noise and artefacts. To assess the impact of the temporal resolution of the moving windows on the accuracy of the estimation, windows of different

lengths (5 s, 15 s, 25 s, 35 s, 45 s and 55 s) were analyzed, all with 1 s sliding step. Within each sliding window, PSD analysis was performed using Welch's method. The peak frequency in the cardiac band (0.7-3 Hz) was identified for HR estimation, while the dominant frequency in the respiratory band (0.05-1 Hz) was selected for RR estimation. These frequency ranges were chosen to reflect typical HR and RR values observed in everyday life scenarios. The identified peak frequencies were then multiplied by 60 to obtain HR (in bpm) and RR (in brpm). This approach made it possible to follow changes in HR and RR over time. It allowed the trade-off between temporal resolution of the measurements and accuracy of the estimate to be assessed according to the length of the selected window. Longer windows provide estimates that are less affected by outliers by averaging over multiple data points, reducing noise but potentially hiding rapid fluctuations. Conversely, shorter windows, while less accurate due to fewer data points, offer greater sensitivity to dynamic changes, making the sensor more responsive but more susceptible to noise. The main steps are shown in Figure 2.7.

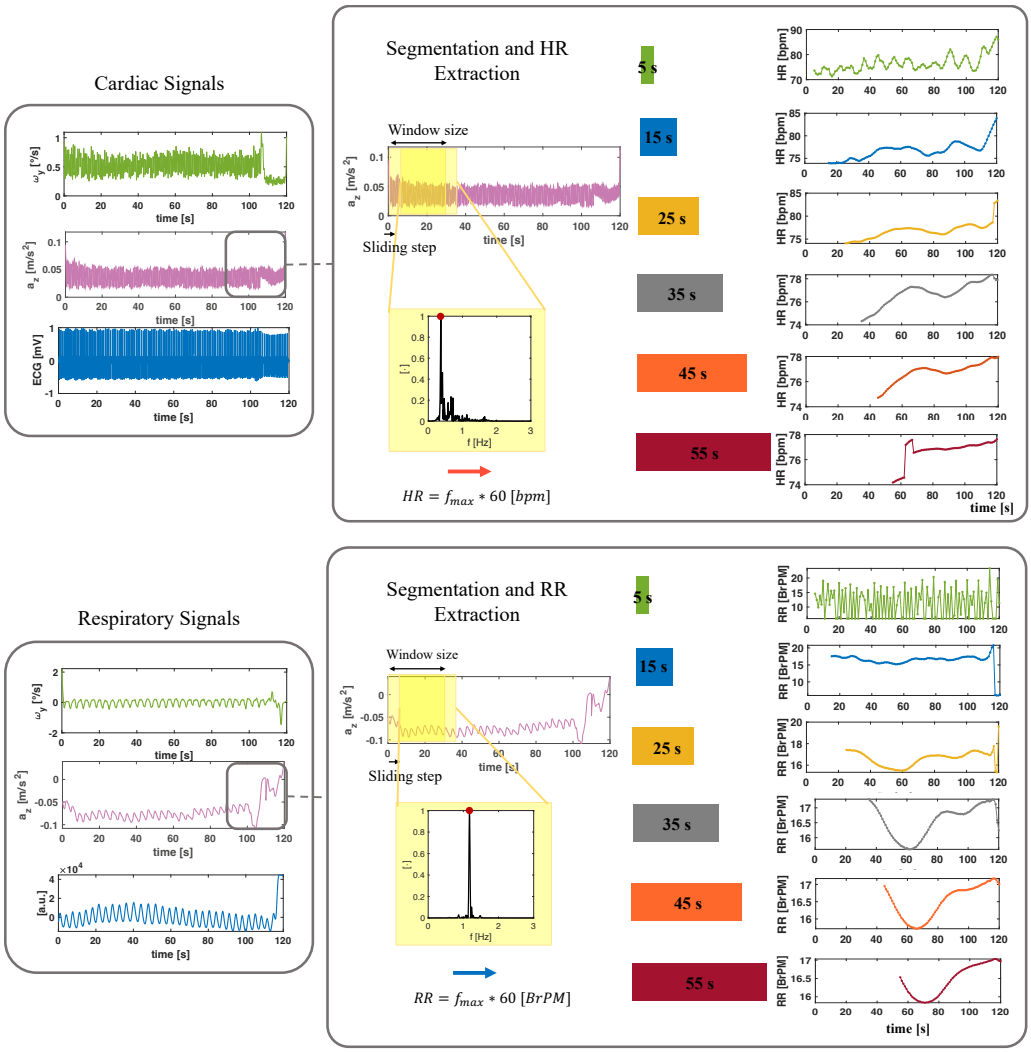

Figure 2.7: HR and RR values were extracted using frequency-domain analysis in sliding windows with six different sizes. Welch's method was applied to identify the dominant frequency, and examples of HR and RR values for one subject are shown across all window sizes. Adapted from [216].

The agreement between the IMU-based estimates and the reference system was assessed using MAE and Bland-Altman analysis.

Results

For HR estimation, accuracy improved with increasing window length, particularly between 5 s and 15 s, where MAEs decreased significantly for all postures. MAE values stabilized for window lengths between 15 s and 35 s, remaining consistently below 1 bpm, and increased slightly above 35 s,

reflecting a trade-off between improving the mean and decreasing the temporal resolution. The MAE values are shown in Figure 2.8.

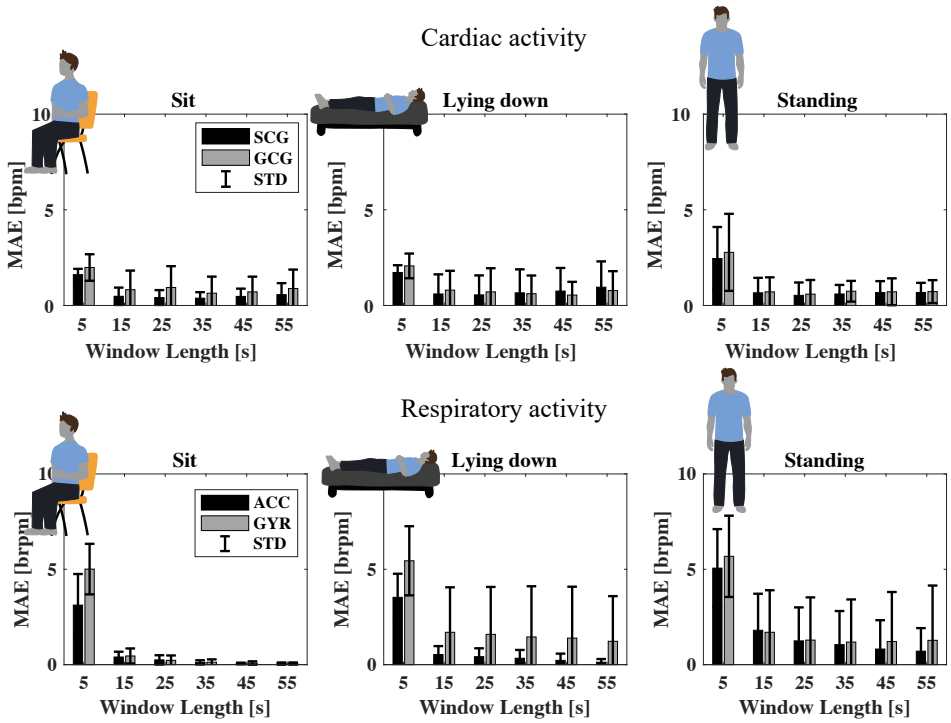

Figure 2.8: Bar graph of the MAE values for HR (top) and RR (bottom) analysis, comparing accelerometer (black) and gyroscope (grey) across different postures and window lengths. Mean MAE values and standard deviations are reported for all subjects. ACC: accelerometer; GYR: gyroscope; STD: standard deviation. Adapted from [216].

Similarly, Bland-Altman analysis (Figure 2.9) showed that shorter windows produced wider LOA, especially in the standing posture, where LOA reached 12.5 bpm for SCG and 12.8 bpm for the gyroscope with a window size of 5 s. In contrast, longer windows reduced LOA to 3.5 bpm for SCG and 3.7 bpm for the gyroscope at 55 s. Both accelerometer and gyroscope signals reliably performed for HR estimation when using window lengths of 15 s or more.

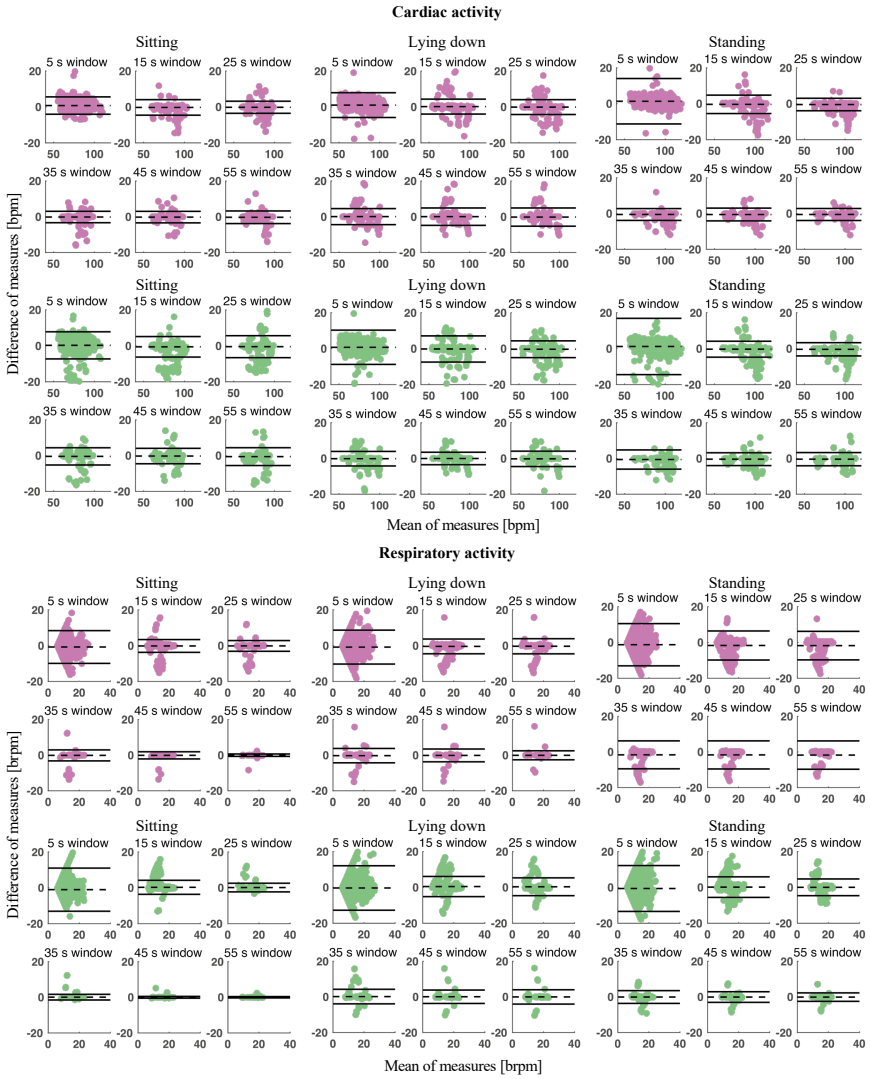

Figure 2.9: Bland Alman plots for accelerometer and gyroscope used for HR and RR estimations in different postures. Adapted from [216].

For RR estimation, shorter windows resulted in higher MAE values and less reliable estimates. In the standing posture, the LOA reached 13.8 brpm for the accelerometer and 12.9 brpm for the gyroscope with a 5 s window. However, performance improved with longer windows, reducing the LOA to 4.7 brpm for the accelerometer and 4.4 brpm for the gyroscope at 55 s.

These findings reveal a trade-off between window length and the ability to capture rapid variations in HR and RR. Shorter windows are more sensitive to dynamic changes but more noise-prone, while longer windows provide greater

stability and accuracy. For HR estimation, an optimal window length ranged between 15 s – 35 s, while for RR estimation, windows of 25 s – 55 s yielded the most accurate results. Overall, no significant differences were found between the performance of the two signals.

This study compared the performance of accelerometers and gyroscopes integrated into a single IMU sensor to simultaneously extract HR and RR. It also analyzed the influence of the window length used for HR and RR extraction and the subjects' posture on the results. The signals from the accelerometer and gyroscope did not show significant differences in the estimation of HR and RR. Regarding window length, a duration of 25 s proved optimal, balancing temporal resolution and accuracy. The posture analysis highlighted those static conditions, such as sitting or lying down, ensure greater accuracy than standing, especially for RR estimation. Unlike previous studies, which focused individually on HR or RR, this analysis demonstrated the importance of comparing different window lengths to identify optimal analysis conditions [219]–[221]. The resulting guidelines can support the practical implementation of IMU sensors for continuous cardiorespiratory monitoring.

2.3. Textile-based sensors for respiratory monitoring

Although IMU sensors have shown strong effectiveness in monitoring cardiac activity across various conditions, their use for respiratory monitoring poses considerable challenges, particularly during movement. As highlighted above (Section 2.2.2) the errors reported in respiratory monitoring are notably higher than those observed for HR extraction. This discrepancy is primarily due to the difficulty in decoupling respiratory signals from overall body movements, a challenge that becomes especially pronounced under dynamic conditions. To address these limitations, attention shifts to the use of piezoresistive textile sensors, which represent a promising alternative for respiratory monitoring during daily life activities. These sensors, integrated directly into garments such as T-shirts, leverage changes in electrical resistance caused by the mechanical

strain. During the respiratory cycle, chest wall deformations caused by inhalation and exhalation stretch and compress the sensors, resulting in measurable variations in resistance that correspond to respiratory activity.

A critical aspect of their effectiveness is the positioning of the sensors on the chest [205]. The sensor's location not only influences the amplitude of the detected signal but also affects its quality, as different regions of the chest wall exhibit varying levels of deformation and susceptibility to motion artifacts. Proper placement is important to ensure accurate signal acquisition and reduce noise, especially in dynamic conditions.

The following section details the design, development, and preliminary validation[2] of a smart T-shirt that embeds piezoresistive textile sensors for breathing monitoring in daily life. Special emphasis is placed on optimizing sensor placement and assessing the system's performance under both static and dynamic conditions.

Methodology

The development of the wearable T-shirt was structured in two distinct phases. The first phase focused on identifying the optimal placement of the sensors on the chest wall to ensure reliable respiratory signal acquisition. In the second phase, the performance of the developed system was evaluated by comparing it against a reference respiratory monitoring device in both static and dynamic conditions. The methodology for the first phase is detailed below.

2. *Validation refers to ensuring that the experimental model used is itself correct. To do this, a set of test results is compared to results obtained using another reliable method for the same conditions* [222].

- Chest wall deformation analysis for sensor placement

To investigate chest wall deformations during breathing, a motion capture system equipped with ten infrared cameras (Qualisys AB, Sweden) was used to monitor thoracic movements.

Eighty-nine photo-reflective markers were placed on the chest and back of five healthy male participants to capture chest wall motion [223]. The experimental protocol required participants to breathe quietly in a seated position on an upright cycle ergometer (Lode Corival, Groningen, Netherlands) for 30 s. A previously established geometric framework was used to map the chest wall into 82 triangular prisms connected by 279 links formed by the 89 photo-reflective markers attached to the anterior and posterior chest regions [223]. The Local Research Ethics Committee of the School of Sport and Exercise Sciences approved the study at the University of Kent, Chatham Maritime, UK (Reference Number: Prop17_2013_14). It adhered to the principles of the Declaration of Helsinki throughout all stages, and written informed consent was obtained from each participant before their involvement.

The markers were divided into two compartments: the rib cage and the abdomen, enabling a focused analysis of deformations specific to each anatomical region, as depicted in Figure 2.10. The deformation analysis aimed to identify links exhibiting highest strain (related to chest wall expansion and contraction) and the highest signal-to-noise ratio (SNR). For each marker pair, the Euclidean distance was calculated over time to represent the relative displacement, $x(t)$, caused by respiratory movements. The relative displacement signal was processed using a first-order Butterworth bandpass filter (0.01 Hz - 2 Hz) to isolate the respiratory component while eliminating unrelated low- and high-frequency noise, covering a broad range of RR values from bradypnea to tachypnea. This filtering step ensured that the deformation analysis focused exclusively on signals generated by the respiratory cycle. The average amplitude of displacement (A_{avg}) was then calculated by measuring the average difference between the maximum peaks (end of inhalation) and

minimum peaks (end of exhalation). These amplitudes were used to compute the strain (ε) for each link, using the following equation:

$$\varepsilon(\%) = \frac{A_{avg}}{l_0}\ x\ 100 \tag{2.2}$$

where l_0 is the baseline distance between markers at the end of the first inhalation. A schematization of the experimental protocol is depicted in Figure 2.10.

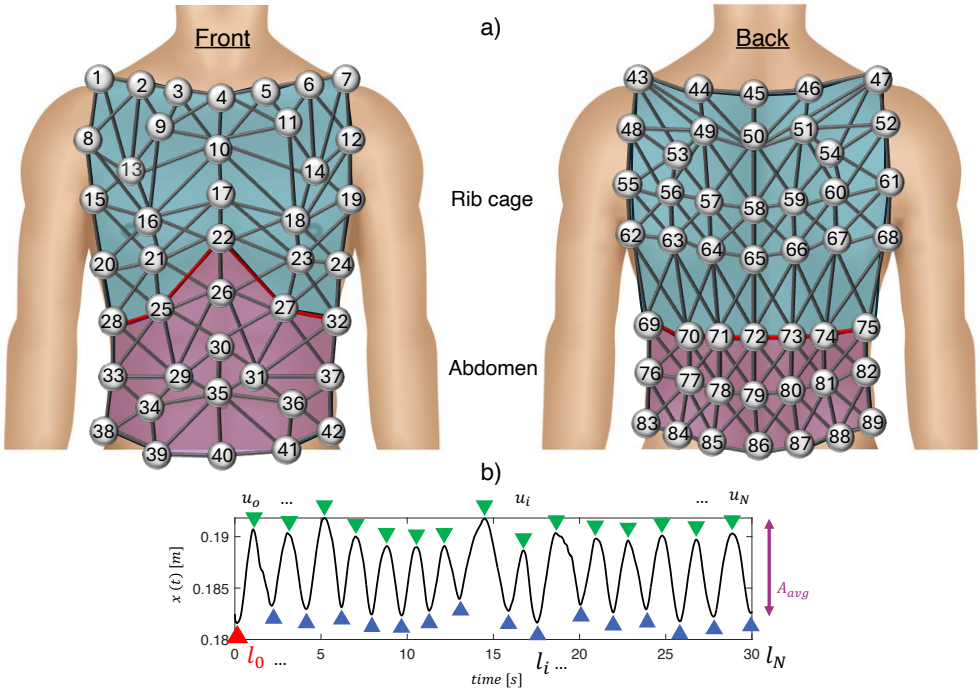

Figure 2.10: (a) Illustration showing the placement of 89 photo-reflective markers on the chest wall, divided into two sections: the abdomen (marked in violet) and the rib cage (marked in blue). The diagram also shows the connections between the pairs of markers. (b) A graph representing the relative displacement signal (i.e., x) between two markers over time, highlighting maximum peaks (end of inhalation, shown as green triangles) and minimum peaks (end of exhalation, shown as blue triangles). Adapted from [224].

The strain values were normalized for each compartment, yielding a dimensionless measure of chest wall deformation. Also, to ensure comparability across participants with different chest sizes, the strain values were normalized within each subject and averaged across all participants. This process produced

an averaged normalized strain value (ε_{norm}^{avg}) for each link, ranging from 0% (minimum deformation) to 100% (maximum deformation) within each compartment.

Moreover, SNR of the displacement signals was analyzed to ensure that the observed deformations were attributable to respiratory activity. At this aim, the RR for each subject was determined from the PSD of the displacement signals. Then, frequencies within a band of ±10% around RR were classified as the signal, while frequencies outside this range were classified as noise. The SNR for each link was calculated as the ratio of the PSD values in the signal band to those in the noise band.

Normalized strain (i.e., ε_{norm}^{avg}) and SNR values averaged across subjects, were combined into a composite metric (U_{norm}^{avg}) corresponding to the sum of the two values to rank the reliability of each link for respiratory monitoring. The obtained values are reported in Figure 2.11. The analysis identified two optimal positions on the rib cage: the link between markers m25–m28 ($\varepsilon_{avg} = 5.0 \pm 2.3\ \%, l_0 = 83.1\ mm\ \varepsilon_{avg} = 5.0 \pm 2.3\ \%, l_0 = 83.1\ mm$) and the link between markers m66–m67 ($\varepsilon_{avg} = 0.68 \pm 0.22\ \%, l_0 = 73.3\ mm\ \varepsilon_{avg} = 0.68 \pm 0.22\ \%, l_0 = 73.3\ mm$).

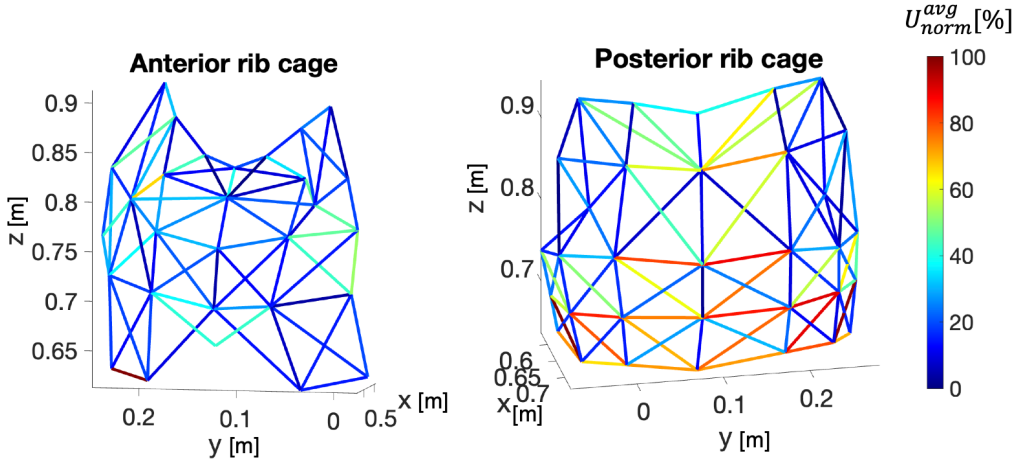

Figure 2.11: Representation of the connections between markers positioned on the anterior and posterior rib cage. The colormap indicates U_{avg}^{norm} values, which combine deformation metrics with normalized SNR values. Adapted from [224].

The sensor locations were selected on the same side of the chest to ensure uniformity and to leave one side of the T-shirt sensor-free. This facilitated the implementation of a size adjustment system to accommodate different body types. The results from this phase provided information for determining the piezoresistive sensors' dimensions, positioning, and expected deformation behavior.

- Sensors design and development

After identifying the optimal sensor placement on the chest wall, the WD was developed, integrating piezoresistive textile sensors into a T-shirt to monitor respiratory activity. This phase involved the design and implementation of the system, its metrological characterization to assess sensor performance, and experimental testing to validate its accuracy in real-world scenarios.

The design and development of two piezoresistive textile sensors were carried out based on the results of the previous analysis. The sensors were fabricated using a conductive piezoresistive textile (MedTex P130) with a sheet resistance of 0.15 Ω/square. The sensor geometry was designed with a central rectangular section 10 mm in height and lengths of 83.1 mm and 73.3 mm for the two sensors (defined as sensor A and sensor B, respectively). Additional rectangular sections (20 mm in height and 10 mm in length) were included on the sides to improve adhesion to the WD. The sensors were then embedded into a T-shirt using a 3 mm-thick polymer matrix made of Ecoflex 00-30 (Smooth-On, Inc., Macungie, PA, USA). This integration enhanced sensor robustness and reduced the influence of external factors, such as moisture. Two molds were fabricated from polylactic acid (PLA) for embedding the sensors using a 3D printer (Creality Ender-3 V2). The molds were designed to fit the specific sensor dimensions and positioned on a sports fabric T-shirt at the locations identified in the previous analysis. The Ecoflex 00-30 mixture (1:1 ratio of part A to part B) was degassed using a vacuum/pressure pump (VCP 130, VWR International, LLC, PA, USA) to remove air bubbles. The mixture was then poured into the

3D molds to a height of 1.5 mm, followed by a curing period of 1 hour. The piezoresistive textiles were subsequently placed inside the molds, and an additional 1.5 g of Ecoflex 00-30 was added to reach a total mold height of 3 mm. The final curing process lasted 3 hours. The resulting sensors, integrated into the WD, exhibited unloading resistances of 23 Ω (sensor A, position m25–m28) and 22 Ω (sensor B, position m66–m67). The final shape of the two sensors is depicted in Figure 2.12, highlighting the steps involved in their realization and integration.

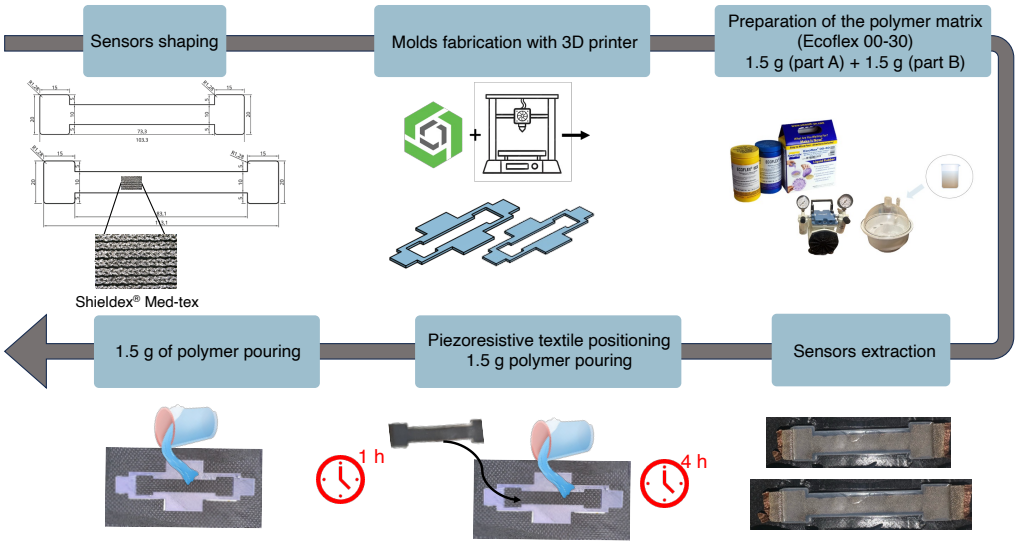

Figure 2.12: Schematization of the main steps involved in the fabrication of the two piezoresistive textile sensors and their integration into the WD using a polymer matrix. Adapted from [224].

- Sensors metrological characterization

After integration into the WD, the sensors were metrologically characterized to evaluate their performance under static tensile loads and cyclic loading and unloading conditions. A mechanical tensile testing machine (model 3365, Instron, MA, USA) equipped with a 500 N load cell was used to apply strain to the sensors, with data recorded at an acquisition frequency of 100 Hz. Resistance changes (ΔR) in the sensors were converted into voltage variations (V_0) using a voltage divider circuit with a fixed resistor of 30 Ω. The voltage variations were captured using an external data acquisition board (NI – DAQ

6009, National Instruments, USA). Two custom PLA anchoring clamps were fabricated using 3D printing technology to ensure proper attachment during testing. Static characterization involved applying a quasi-static tensile load to the sensors to measure their response to strain. Each sensor was placed between the clamps of the tensile machine and subjected to strain values ranging from 0% to 10% of their initial lengths (83.1 mm for sensor A at position m25–m28 and 73.3 mm for sensor B at position m66–m67). A 5 mm/min displacement rate was used, and resistance changes were recorded over five consecutive trials. The calibration[3] curve ($\Delta R\ vs\ \varepsilon$) was obtained by processing the collected data in MATLAB®. From the calibration curve, static sensitivity[4] (S_ε) was calculated as in equation 2.3.

$$S_\varepsilon = \frac{\Delta R}{\varepsilon_{max}} \tag{2.3}$$

Moreover, the gauge factor (GF) was calculated as follows:

$$GF = \frac{\frac{\Delta R}{R_0}}{\varepsilon_{max}} \tag{2.4}$$

For sensor A, S_ε was found to be 9.4 Ω/% with a GF of 6.0 at a maximum strain of 5%, while, at 10% strain, S_ε decreased to 7.2 Ω/%, with a corresponding GF of 4.7. For sensor B, S_ε was slightly lower, measuring 9.1 Ω/% and 5.8 for the GF at 5% strain, and 5.3 Ω/% with a GF of 3.2 at 10% strain.

3. *Calibration refers to the operation that, under specified conditions, in a first step, establishes a relation between the quantity values with measurement uncertainties provided by measurement standards and corresponding indications with associated measurement uncertainties and, in a second step, uses this information to establish a relation for obtaining a measurement result from an indication. The calibration curve is the expression of the relation between indication and corresponding measured quantity value* [222].

4. *Sensitivity is defined as the quotient of the change in the indication of a measuring system and the corresponding change in a value of a quantity being measured.* [222].

These GF values are higher compared to other sensors reported in the literature, such as capacitive strain sensors [225] (GF below 1.5 with 100% strain), weft-knitted strain sensors [226] (GF of about 1 with 20% strain), and strain-sensing threads [227] (GF of about 2.5 with 50% strain). The sensors underwent 30 loading and unloading cycles to simulate chest wall movement during breathing.

A maximum strain of 5% of the initial length (4.2 mm for sensor A and 3.7 mm for sensor B) was applied. The tests were performed at four speeds corresponding to RR values of 6 brpm (bradypnea), 12 brpm (eupnea), 24 brpm (tachypnea), and 36 brpm (tachypnea).

The hysteresis span ($\%e_H$) was calculated as:

$$\%e_H = \frac{e_{max}}{r_{FS}} \cdot 100 \tag{2.5}$$

Where e_{max} represents the maximum resistance difference during loading and unloading, and r_{FS} is the sensor's full scale for the loop [149]. These values were calculated to evaluate the difference between loading and unloading resistance changes at the same strain level. For sensor A, the hysteresis span decreased with increasing RR, measuring 24.9% at 6 brpm, 23.0% at 12 brpm, 20.8% at 24 brpm, and 20.4% at 36 brpm. Similarly, sensor B exhibited hysteresis spans of 25.3% at 6 brpm, 25.1% at 12 brpm, 21.4% at 24 brpm, and 21.2% at 36 brpm. Curves for static and cyclic metrological characterization are reported in Figure 2.13.

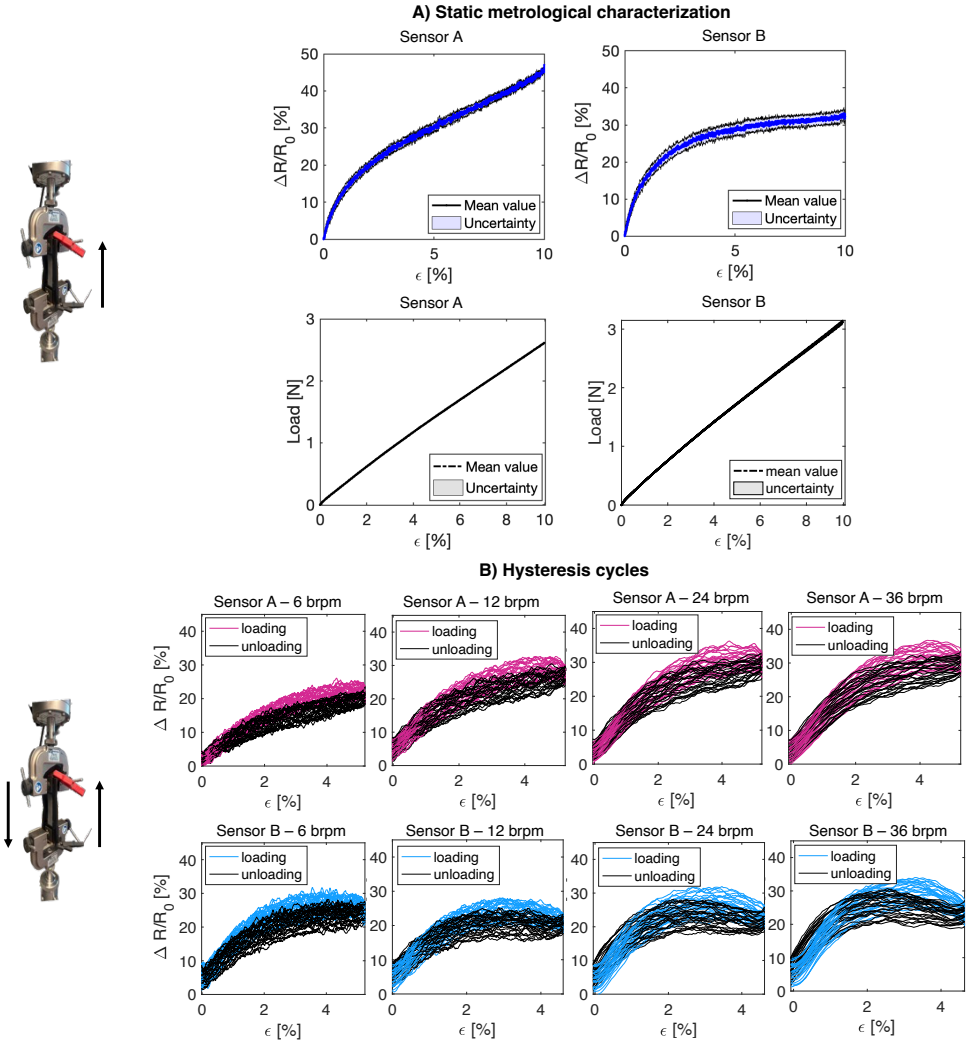

Figure 2.13: (A) Illustration of the output response of the sensors integrated into the WD under a quasi-static tensile load, with strain levels reaching up to 10% of their initial length. (B) Visualization of the hysteresis cycles produced by the sensors when subjected to cyclic loading at different simulated breathing frequencies: 6 bpm, 12 bpm, 24 bpm, and 36 bpm. Adapted from [224].

These results highlight the sensors' ability to respond accurately to both static and dynamic loading conditions, maintaining consistent performance across trials and demonstrating their suitability for applications involving cyclic strain, such as respiratory monitoring.

- Pilot study on healthy volunteers

A pilot study was carried out on eight healthy volunteers (two men and six women) to evaluate the performance of the WD during various conditions,

including sitting, standing, and walking. The system consists of the two flexible piezoresistive sensors embedded in the T-shirt, a signal conditioning board for resistance-to-voltage conversion, and a data acquisition module (Feather M0 Adalogger Adafruit, USA). The signal conditioning board was connected to the data acquisition module that was used to store data at an acquisition frequency of 25 Hz. The conditioning and acquisition boards were enclosed in a PLA 3D-printed case, placed on the back of the T-shirt. Flexible cables connected the sensors to the conditioning board, maintaining a lightweight and wearable design. The experimental setup also included the BioHarness chest strap to collect reference respiratory waveforms with an acquisition frequency of 25 Hz. Volunteers wore both the wearable and Bioharness systems during the protocol. Synchronization was achieved using a 10 s apnea period at the beginning of the protocol, followed by three testing phases: i) quiet breathing (60 s) and tachypnea (60 s) in a sitting position; ii) quiet breathing (60 s) and tachypnea (60 s) in a standing position; iii) quiet breathing (60 s) during walking. A schematization of the experimental setup and protocol is shown in Figure 2.14.

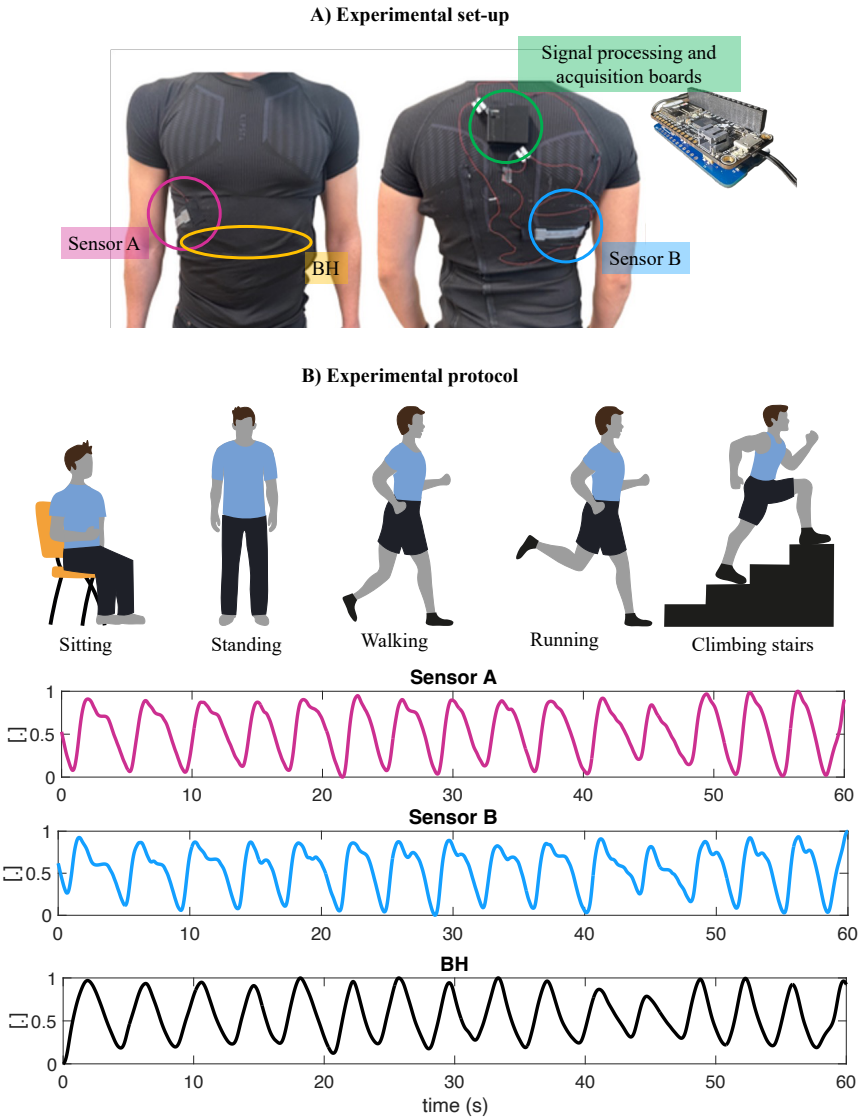

Figure 2.14: Experimental setup with flexible sensors integrated into the WD and a PLA case housing the signal conditioning and data acquisition modules. The protocol included quiet breathing and tachypnea in sitting, standing, and walking conditions, with signals compared to those from the BH reference system. Adapted from [224].

Data collected from the flexible sensors and the Bioharness system were first synchronized by aligning the inhalation endpoints after the apnea phase. Non-respiratory components of the signals were attenuated using a first-order Butterworth bandpass filter with cutoff frequencies of 0.01 Hz and 1.5 Hz, ensuring the preservation of respiratory-related signal components across a wide range of RR values, from bradypnea to tachypnea. The filtered signals were then analyzed to determine the mean RR during each trial. For the flexible sensors

positioned at the m25–m28 (sensor A) and m66–m67 (sensor B) rib cage links and the reference system, the PSD was estimated with a resolution of 0.01 bpm. The peak frequency in the PSD was multiplied by 60 to calculate RR in brpm. This calculation was performed for each phase of the protocol, considering the signals from each sensor individually. Also, the combined signal obtained by summing the outputs of the two sensors was considered in the analysis. The errors between the wearable and reference systems were calculated for each protocol phase by averaging results across all subjects. These errors were analyzed for individual sensors and the combined signal to evaluate the system's performance. RR values per each posture calculated across subjects are reported in Figure 2.15.

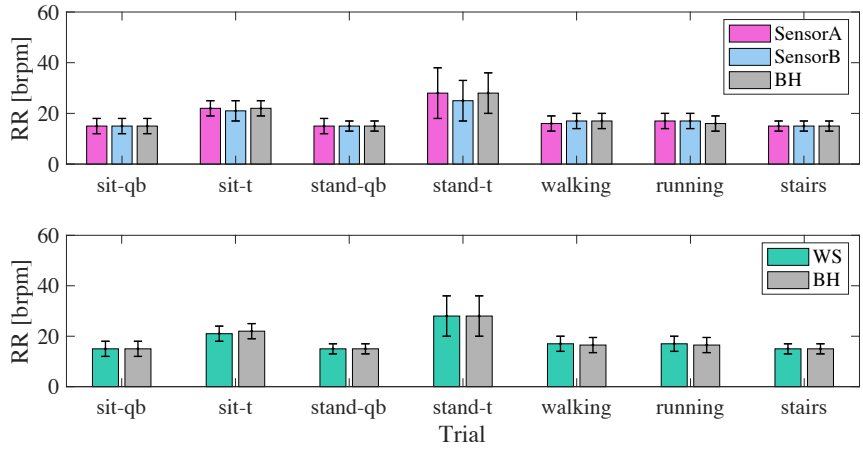

Figure 2.15: Bar charts display the mean RR values across all subjects for Sensor A, Sensor B, and the WS, representing the summed signal from both sensors. The results are shown for all phases of the experimental protocol, along with their respective standard deviations. Adapted from [224].

The WD demonstrated good agreement with the BH reference system in measuring RR. When analyzed individually, sensor A outperformed sensor B in sitting and standing conditions, with maximum errors of 0.1 brpm and 0.3 brpm, respectively. During walking, sensor B exhibited better performance, with a maximum error of 0.1 brpm compared to 1.9 brpm for sensor A. The use of the combined signal (referred to as WS) improved accuracy. In all subjects, the maximum error with the combined signal was 0.5 brpm during sitting tachypnoea, lower than the maximum error of 3.1 brpm observed for sensor B

during standing tachypnoea. The combined signal provided a more valid estimate of RR, as it exploited data from two different points of the rib cage, reducing the impact of potential artefacts from misalignment or movement.

Conclusion

The study describes the development of a smart T-shirt with flexible sensors for monitoring RR. The design is based on analyzing chest wall deformations during breathing using an optical system with reflective markers to identify the optimal placement for piezoresistive sensors. Two positions were selected on the anterior rib cage, considering the amplitude of deformations and the SNR. Based on these findings, two flexible sensors were developed and integrated into the T-shirt. Subsequently, the sensors underwent static characterization and repeated load cycles. The metrological characterization of the piezoresistive sensors, performed post-integration, demonstrated favorable GF values of 6.0 and 5.8, surpassing comparable sensors in literature including capacitive strain sensors (GF < 1.5) [225], weft knitted sensors (GF ≈ 1) [226], and strain sensing threads (GF ≈ 2.5) [227].

A pilot study involving eight volunteers tested the system's feasibility under static conditions (sitting, standing) and dynamic activities (walking, running, climbing stairs) while simulating different breathing patterns. The results showed a MAE of 0.32 bpm when combining the signals from the two sensors, which was lower than the MAE for the individual sensors (0.53 bpm and 0.78 bpm). The dual-sensor configuration demonstrated advantages when one of the sensors failed to adhere properly to the chest due to non-respiratory movements.

This study's strength lies in optimizing sensor placement, considering both the amplitude and reliability of signals. Additionally, integrating sensors using a polymer matrix enhanced their robustness and reduced the impact of external factors such as humidity. This approach could be further enhanced by integrating inertial sensors to assess the quality of respiratory data based on the subject’s activity level. It is worth noting that preliminary tests for sensor placement

optimization were conducted exclusively on male participants, while the final evaluation of the T-shirt included both male and female subjects. Although this second testing phase ensured evaluation across different body morphologies, potential gender-related differences in chest wall deformation were not explicitly analyzed. Future studies could further investigate these aspects to better tailor the system for diverse body morphologies.

2.4. Conclusions

IMU sensors have been demonstrated to be feasible for monitoring cardiac and respiratory parameters, highlighting their reliability for real-life health monitoring applications. However, the accuracy of RR estimation remains a challenge, particularly in dynamic conditions where movement artifacts and postural changes significantly impact performance. The study showed that physiological monitoring with IMU sensors is highly dependent on sensor positioning and orientation, and identified the z-axis (dorsoventral) and MV position as the best configuration for extracting raw cardiac and respiratory signals, outperforming other axes and investigated regions of the torso. This result is particularly relevant for monitoring cardiac activity where, while the z-axis is widely used for this purpose in the literature [101], [109], [210], recent reviews suggest that the X position remains the most frequently utilized anatomical landmark for cardiac signal extraction [109]. For HR estimation, the observed errors were lower than those reported in similar studies [213], [214], highlighting the robustness of the proposed configuration for real-world scenarios.

A comparison between accelerometers and gyroscopes placed in the MV region was then conducted across different daily life activities, such as sitting, standing, and walking. No significant differences in HR and RR estimation were observed between the two sensors. However, the analysis revealed that the choice of window length in frequency-domain analysis impacts performance. Specifically, windows longer than 15 s yielded more stable and accurate

estimates for both HR and RR. While the performance for HR estimation is promising, RR estimation errors remain relatively high compared to those achieved with other WDs, confirming the current limitations of IMUs for respiratory monitoring, particularly in dynamic conditions.

To address these limitations, the study explored the use of piezoresistive textile sensors as an alternative for respiratory monitoring. Integrated into garments such as T-shirts, these sensors measure chest deformations during breathing. Unlike IMUs, which are influenced by movements along three axes, they have been shown to provide more accurate respiratory monitoring under static and dynamic conditions. Additionally, embedding these sensors into a polymer matrix has improved their durability and reduced external influences such as humidity and mechanical stress, making them more suitable for long-term monitoring in daily life. By leveraging data from two distinct chest wall locations, this system achieved good agreement with reference measurements in both static and dynamic scenarios, with MAE values for RR estimation approximately 80% lower than those obtained with IMUs. Despite these advancements, textile sensors also present some limitations. While they improve RR monitoring, their performance could still benefit from further optimization, particularly in highly dynamic contexts. Furthermore, their performance in measuring act-act RR should be evaluated.

In conclusion, this chapter highlights the strengths and limitations of WDs, including IMUs and textile-based systems, for monitoring cardiac and respiratory parameters during daily-life activities. The analysis focuses on their performance in real-world conditions, particularly on the influence of sensor positioning, configuration, and the challenges posed by motion artifacts and postural changes. The primary aim of this chapter is to identify the most suitable sensor configurations to maximize monitoring reliability. The findings contribute to a better understanding of how WDs can be optimized for specific applications, providing a foundation for further developments of such technologies.

3

Chapter 3: IMU-Based Solutions for Cardiac Monitoring in Clinical Applications

3.1. Introduction

Cardiovascular diseases (CVDs) are a leading cause of morbidity and mortality worldwide, driving the need for advanced technologies to improve cardiac monitoring and diagnostics [228], [229]. Traditional approaches, such as ECG, primarily target the heart's electrical activity and are used to detect arrhythmias and assess cardiac function [51], [230]. However, these methods offer limited insights into cardiac mechanics, which represent an equally important aspect of cardiac performance [110]. Cardiac mechanics includes the forces and movements generated by the heart, providing information about its functional capacity and aiding in the diagnosis of conditions such as heart failure and valvular pathologies [231]–[233]. While conventional techniques like echocardiography and MRI remain the gold standard for evaluating mechanical activity [234], [235], their application is often limited by high costs, the need for specialized infrastructure, and their inability to provide continuous monitoring.

WDs, particularly IMUs, present an alternative approach to measure heart mechanics [101], [109]. By leveraging the capability of SCG and GCG to capture the mechanical activity of the heart through chest vibrations and rotational movements, researchers have been able to derive information about cardiac function [109], [175], [176]. These signals are especially valuable for

quantifying characteristic CTIs, such as LVET and IVCT, which are useful for diagnosing and monitoring various cardiovascular pathologies [101]. Several studies have explored the utility of SCG and GCG in assessing cardiovascular health. For instance, reductions in SCG amplitudes have been associated with systolic dysfunction, offering a non-invasive means of evaluating left ventricular contractility [236]–[238]. Similarly, alterations in GCG waveforms have been linked to irregularities in the rotational mechanics of the heart, which are observed in conditions such as hypertrophic cardiomyopathy and AS [191], [239]. [126] demonstrated that SCG-based measurements of pre-ejection period (PEP) and LVET correlated well with echocardiographic findings, supporting their use as alternatives to imaging-based assessments. The combination of SCG and GCG signals has enabled a more comprehensive evaluation of cardiac mechanics [111], [240]. Furthermore, these signals have been used to study HRV, which reflects autonomic function and has applications in evaluating conditions such as heart failure and arrhythmias [241]–[243]. For example, [244] demonstrated that SCG signals could effectively monitor HRV in ambulatory settings, suggesting their potential for long-term cardiovascular monitoring.

Recent advances in data processing have further enhanced the application of SCG and GCG. Algorithms for feature extraction and pattern recognition, including ML techniques, have been employed to classify individuals with cardiovascular conditions, such as myocardial infarction and left ventricular hypertrophy [240], [245], [246]. These methods allow for less costly and less invasive diagnostics that do not require controlled environments, broadening their applicability in real-world settings.

This chapter delves into two applications of IMU sensors in cardiac monitoring. The first investigates their use in HRV extraction, leveraging the mechanical signals captured by IMUs to derive HRV indexes. The second examines the role of IMUs in classifying AS, a prevalent valvular pathology requiring timely diagnosis to prevent disease progression. These studies highlight how IMUs can be used in conjunction with conventional diagnostic

methods to provide a more thorough examination of cardiac health by providing understanding of the mechanical components of cardiac function.

3.2. IMU sensors for HRV extraction

The analysis of HRV is increasingly recognized in the clinical field as a diagnostic tool for assessing cardiovascular health. HRV is the temporal variations between consecutive heartbeats, known as inter-beat intervals (IBIs), reflecting the balance between the sympathetic and vagal (or parasympathetic) branches of the autonomic nervous system [247], [248]. These components regulate HR: the first drives the "fight or flight" response by increasing HR, blood pressure, and blood flow to muscles. Conversely, the parasympathetic nervous system governs the "rest and digest" response by slowing HR and promoting recovery. Together they maintain homeostasis by adapting to physiological demands and are indexes of overall cardiac health. For instance, a reduced HRV has been correlated with heightened risks of arrhythmias, heart failure, and sudden cardiac death, underscoring its clinical relevance [249]–[251]. Research shows HRV correlates with HR turbulence (HRT) and ventricular arrhythmias, reflecting sympathovagal balance on cardiac dynamics [252]. Additionally, HRV and HRT serve as predictive tools for post-myocardial infarction risk assessment [253], [254]. In rehabilitation, HRV changes correlate with improved exercise capacity after revascularization procedures [255]. HRV also indicates stress resilience, with higher values associated with better stress management and lower anxiety and depression risks [256].

Traditionally, HRV measurement relies on ECG signals, calculating IBIs from the time between consecutive R-peaks. Recent technological advances have introduced new approaches, such as IMU sensors [242], [257]. These sensors bring advantages like portability, affordability, and simple integration into WDs. These features make them appropriate for continuous HRV monitoring in both clinical and everyday settings. In the literature, various HRV indexes have been proposed, including linear metrics (time-domain and

frequency-domain) and non-linear methods. While few studies have explored the estimation of linear indexes using IMUs, non-linear indexes remain largely unexplored in this context. This section investigates the use of IMU sensors for the extraction of both linear and non-linear HRV indexes, providing an evaluation of their potential in estimating IBIs and associated metrics across different postures.

Methodology and Results

Twenty-one healthy volunteers (18 males, 3 females, height: 177±9 cm, body mass: 74±15 kg) participated in the study. None of the participants had cardiovascular or other systemic diseases that could affect HRV. Each participant provided written informed consent before the experiment. An IMU sensor (Xsens Technologies B.V., Enschede, Netherlands) was positioned at the xiphoid process, the most used location according to literature. This sensor was used to record mechanical signals, including SCG and GCG (full scale: ±16 g for accelerometer, and ±2000°/s for gyroscope), which capture vibrations and angular movements associated with cardiac activity [101]. The IMU sensor was positioned with the x-axis aligned with the cranio-caudal direction, y-axis aligned with the latero-lateral direction, and z aligned with the antero-posterior (or dorsoventral) direction. A wearable chest strap (Zephyr Bioharness™) recorded the reference ECG signal, providing R-peak intervals as ground truth for the IBI calculation. Data collection occurred in two positions: a seated posture and a supine posture. The IMU sensors sampled data at 120 Hz, while the ECG device recorded at 250 Hz. Figure 3.1 shows the experimental setup and protocol.

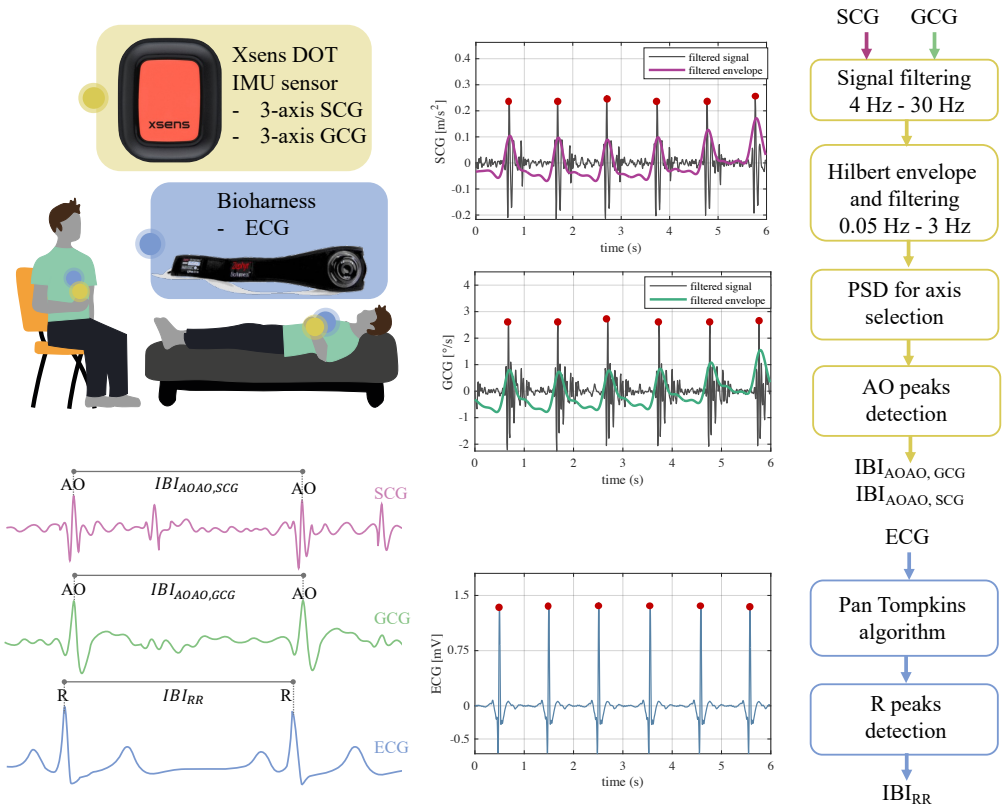

Figure 3.1: Schematization of experimental setup, protocol, and main steps carried out for data analysis. Adapted from [258].

Each participant underwent a 120 s data acquisition session in each posture. Using the IMU sensor, SCG and GCG signals were collected along the three axes. The data underwent preprocessing and analysis to extract IBI values for HRV analysis. A schematization of the main steps carried out for data analysis is shown in Figure 3.1. The first step involved bandpass filtering the SCG and GCG signals with a Butterworth filter (cutoff frequencies: 4 Hz – 30 Hz) to isolate cardiac vibrations while reducing noise [98]. IBIs were calculated from AO peaks, the most prominent feature in SCG and GCG signals, indicative of the aortic valve opening (see Figure 3.1). To enhance these peaks, the Hilbert envelope of the filtered signals was computed using a 330 ms sliding window. This envelope underwent additional filtering between 0.05 Hz and 3 Hz to include typical cardiac activity frequencies.

To identify the most informative axis, the PSD of the envelope was computed for each axis using a 30 s window with a 50% overlap. The axis with the highest signal power in the 0.05–3 Hz frequency range was selected for further analysis. Using this axis, AO peaks were detected through an algorithm with specific time and amplitude thresholds: a minimum interval of 500 ms between consecutive peaks and exclusion of peaks below 60% of maximum signal amplitude. The IBIs were then calculated as the time intervals between successive AO peaks, separately for both SCG ($IBI_{AOAO,SCG}$) and GCG signals ($IBI_{AOAO,GCG}$).

For the ECG signals, the Pan-Tompkins algorithm was used to detect R peaks, as the reference for IBI calculations [209]. The IBIs were subsequently computed as the time intervals between consecutive R-peaks in the ECG signal (IBI_{RR}).

Bland-Altman analysis was performed to compare the IBI values calculated from SCG and GCG with those from the reference system, as shown in Table 3.1. Moreover, the Pearson correlation coefficient (i.e., R) was calculated per each posture and signal collected with IMU sensor. The R value provides a measure of the linear relationship between the IBIs derived from the IMU signals and those obtained from the reference ECG, with values closer to 1 indicating stronger positive correlations and, therefore, higher agreement between the methods.

Table 3.1: Bland Altman analysis results and R coefficients for IBI calculated from SCG and GCG, compared with those calculated with ECG

	IBI analysis			
	Seated		Supine	
	SCG	GCG	SCG	GCG
R	0.96	0.93	0.99	0.99
MOD±LOAs [ms]	-0.47±75.41	-0.18±105.34	-0.15±33.71	-0.13±26.43
Number of detected beats	2464	2464	2274	2274

The correlation analysis revealed strong linear relationships across all cases, with R values exceeding 0.93 for all conditions. The supine posture yielded better results compared to the seated position, likely because it reduced motion artifacts and provided more stable sensor placement.

Subsequently, both linear and non-linear HRV indexes were calculated to assess autonomic nervous system activity. Figure 3.2 shows the classification of HRV indexes from the analysis. The indexes fall into two main categories: Linear indexes (subdivided into time-domain and frequency-domain methods) and Non-Linear indexes.

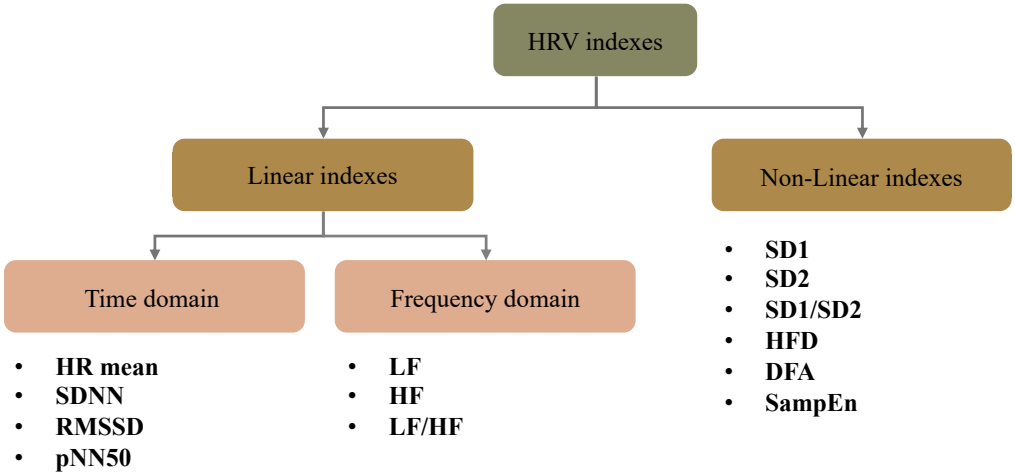

Figure 3.2: Classification of HRV indexes into Linear and Non-Linear categories. Linear indexes are further divided into time-domain and frequency-domain methods. Adapted from [258].

The linear indexes were calculated using time-domain and frequency-domain analyses. The time domain, the parameters included:

- Mean HR: The average HR throughout the recording period.
- Standard deviation of all IBIs (SDNN): This is a measure of overall HRV, capturing both sympathetic and parasympathetic influences. It reflects long-term HRV and is informative on heart's ability to adapt to slow changes (e.g., circadian rhythms). Higher SDNN

values suggest a healthy, responsive cardiac system, whereas lower values can indicate health risks. This index is calculated as follows.

$$SDNN = \sqrt{\frac{1}{N-1}\sum_{i=1}^{N}(IBI_i - \overline{IBI})^2} \tag{3.1}$$

where IBI_i represents the i-th inter-beat interval, $\overline{IBI}$ is the mean of all IBIs, and N is the total number of IBIs.

- Root mean square of successive differences (RMSSD): reflects short-term HRV, primarily driven by parasympathetic activity, and is sensitive to rapid changes in HR. This index is calculated as in Equation 3.2.

$$RMSSD = \sqrt{\frac{1}{N-1}\sum_{i=1}^{N-1}(IBI_{i+1} - IBI_i)^2} \tag{3.2}$$

- Percentage of successive IBIs differing by more than 50 ms (pNN50): highlights parasympathetic modulation and short-term variability. Like RMSSD, higher pNN50 values indicate greater parasympathetic modulation and healthy short-term variability. It is calculated as in Equation 3.3.

$$pNN50 = \frac{N_{50}}{N_{TOT}} \cdot 100 \tag{3.3}$$

where N_{50} represents the number of successive IBIs that differ by more than 50 ms, and N_{TOT} is the total number of IBIs in the dataset.

To further assess HRV, frequency-domain indexes were calculated, measuring the power distribution across specific frequency bands. These bands include:

- Very Low Frequency (VLF): reflect slower oscillations in HR, in range 0.003 Hz–0.04 Hz. It provides information on slow physiological processes. High VLF power is generally interpreted as indicative of increased sympathetic activity or factors related to thermoregulation and hormonal influences.

- Low Frequency (LF): represent oscillations in HR with frequencies ranging from 0.04 Hz to 0.15 Hz. It represents a combination of sympathetic and parasympathetic activity.

- High Frequency (HF): correspond to oscillations in HR with frequencies ranging from 0.15 Hz to 0.4 Hz. HF power is a marker of parasympathetic activity and is influenced by respiratory sinus arrhythmia, where HR naturally fluctuates with the breathing cycle. High HF values are commonly observed during restful states, such as relaxation, meditation, or recovery after physical activity, highlighting a state of physiological rest and recovery.

Additionally, the LF/HF ratio was calculated to assess the balance between sympathetic and parasympathetic contributions. Higher LF/HF values indicate increased sympathetic dominance, whereas lower values suggest parasympathetic predominance.

Non-linear indexes were computed to analyze complex patterns in HRV using the Poincaré plot. These included:

- SD1 (short-term variability): The standard deviation of points perpendicular to the line of identity of the Poincarè plot, reflecting short-term HRV driven by parasympathetic activity. Hence, Higher SD1 values indicate stronger parasympathetic modulation.
- SD2 (long-term variability): The standard deviation of points along the line of identity. It reflects the long-term HRV, regulated by both sympathetic and parasympathetic activity. High SD2 values indicate

adaptability of the cardiovascular system to slower regulatory changes.

- SD1/SD2 ratio: A measure of the balance between short-term and long-term variability, revealing the interplay of autonomic nervous system regulation.

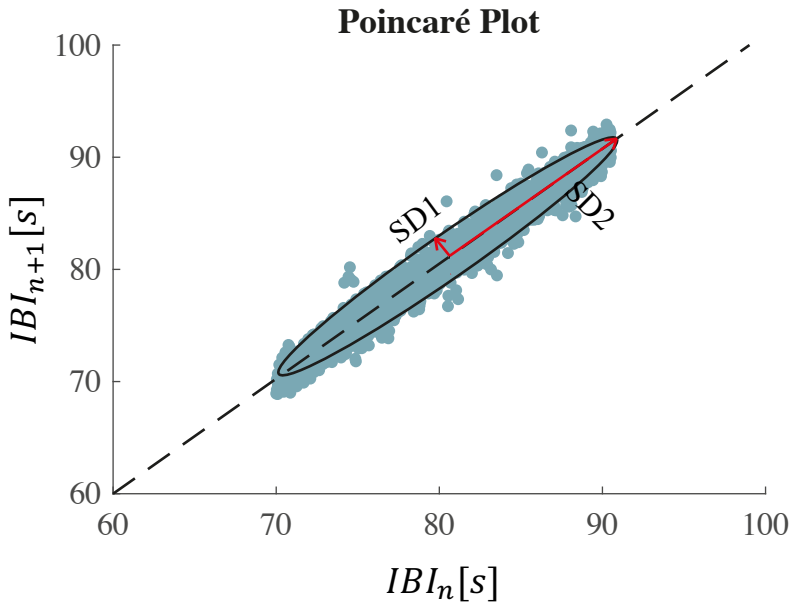

Figure 3.3: A representative Poincarè plot. n: number of IBIs

Other non-linear indexes were calculated to evaluate the complexity, scaling properties, and irregularity of the RR interval series. These included:

- Higuchi Fractal Dimension (HFD): quantifies the fractal dimension of HRV over time, and the dynamical behavior of IBIs. Higher HFD values indicate a higher level of complexity and variability in heart dynamics, often associated with healthy physiological states. Conversely, lower HFD values suggest a loss of complexity, which can be a marker of pathological conditions or reduced autonomic control [259].
- Detrended Fluctuation Analysis (DFA): evaluates the fractal-like scaling properties of HRV by analyzing the existence of patterns across varying time windows. The α-scaling exponent characterizes

the signal: anti-correlated patterns showing randomness ($\alpha < 0.5$), typical of acute stress or disfunctions; fractal-like behavior ($0.5 < \alpha < 1$), indicating healthy systems; and strongly correlated or pathological dynamics ($\alpha > 1.0$), often associated with chronic conditions or the effects of aging [260].

- Sample Entropy (SampEn): measures how irregular and unpredictable a signal is by calculating the likelihood that similar patterns will stay consistent over time. Higher SampEn values indicate greater complexity, while lower values indicate more regularity, which often suggests pathological conditions or reduced physiological flexibility [261].

Mean and standard deviation values for all HRV indexes were derived across the 21 volunteers. To assess statistical significance, one-way ANOVA test was assessed, comparing ECG values with those from SCG and GCG. *p*-values below 0.05 were considered to indicate statistically significant differences between groups. Table 3.2 and Table 3.3 summarize the mean and standard deviation values of HRV indexes derived from ECG, SCG, and GCG measurements, including both linear (time and frequency domains) and non-linear metrics.

Table 3.2: Mean and standard deviation of HRV linear indexes calculated with time domain (SDNN, RMSSD, pNN50) and frequency domain (LF,HF,LF/HF) analysis. *:statistically significant (*p <0.05)*

HRV index	Seated			Supine		
	ECG	SCG	GCG	ECG	SCG	GCG
HR mean [bpm]	71.33±9.93	71.30±9.96	71.32±9.93	68.29±9.11	68.29±9.10	68.29±9.10
SDNN [ms]	67.32±33.66	80.28±35.44	81.21±50.85	65.50±32.42	71.02±35.64	66.75±31.77
RMSSD [ms]	55.00±35.26	81.44±46.21	84.31±72.18	58.85±34.50	69.73±45.47	58.40±34.70
pNN50 [%]	30.06±22.76	41.77±24.14	40.64±23.77	26.87±23.36	36.77±25.09	32.36±22.94
pLF [%]	56.27±20.80	46.40±18.28	50.42±22.43	55.59±18.91	48.36±19.16	54.12±17.89
pHF [%]	43.72±20.80	56.80±17.85	49.57±22.43	44.40±18.91	51.63±19.16	45.87±17.89
LF/HF	2.26±2.78	0.96±0.73*	1.47±1.23	1.69±1.19	1.24±0.92	1.54±1.05

Table 3.3: Mean and standard deviation of HRV non linear indexes. *:statistically significant ($p < 0.05$)

HRV index	Seated			Supine		
	ECG	SCG	GCG	ECG	SCG	GCG
SD1 [s]	0.05±0.03	0.05±0.03	0.05±0.05	0.04±0.02	0.04±0.03	0.04±0.02
SD2 [s]	0.09±0.04	0.09±0.04	0.09±0.05	0.08±0.04	0.08±0.04	0.08±0.04
SD1/SD2	0.59±0.24	0.54±0.16	0.58±0.26	0.43±0.17	0.56±0.23	0.49±0.21
HFD	1.92±0.09	1.90±0.09	1.90±0.09	1.84±0.10	1.89±0.09	1.87±0.10
DFA	0.69±0.22	0.74±0.21	0.74±0.25	0.90±0.26	0.77±0.26	0.84±0.28
SampEn	1.72±0.38	1.76±0.45	1.83±0.48	1.53±0.28	1.83±0.49	1.64±0.29

The supine posture demonstrated stronger agreement with the reference ECG, with HRV indexes from SCG and GCG showing closer alignment to the reference values for both linear and non-linear metrics. The only statistically significant difference was observed in the seated posture, where SCG showed a discrepancy in the calculation of the LF/HF ratio compared to ECG.

Moreover, R values were calculated using ECG-derived HRV indexes as the reference, as shown in Figure 3.4. To evaluate performance, the HRV indexes were calculated both using both our optimized axis selection presented above (Figure 3.4a), and the conventional axes from literature (z-axis for SCG and y-axis for GCG, as shown in Figure 3.4b).

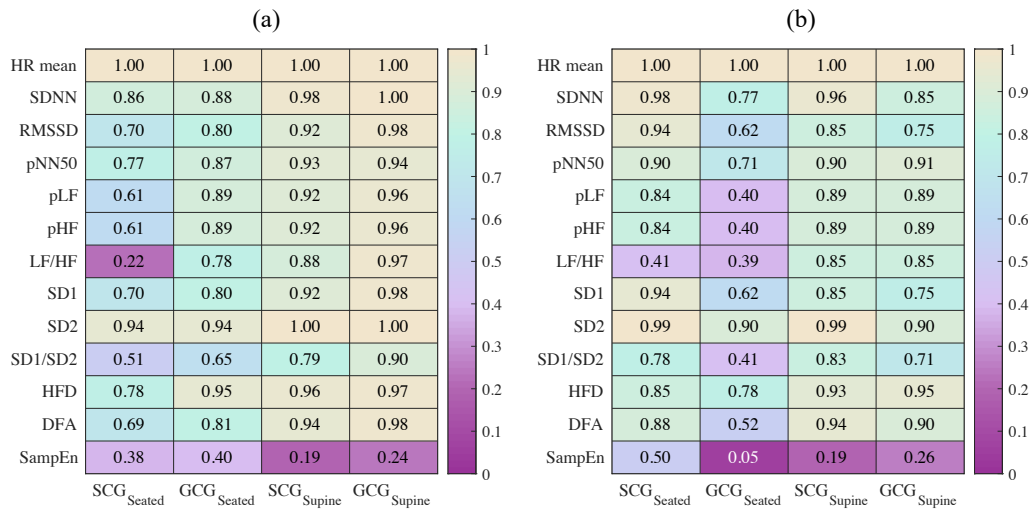

Figure 3.4. Correlation coefficients (R) calculated using ECG-derived HRV indexes as the reference. Panel (a) shows the results from the optimized axis selection described above, while panel (b) represents the conventional axes used in the literature, with the z-axis selected for SCG and the y-axis for GCG. Adapted from [258].

For the optimized axis selection, all measurements showed positive R values, with higher correlations found in the supine compared to seated position. Also, GCG signals showed higher correlations compared to SCG in both postures. Linear HRV indexes from both SCG and GCG correlated with reference values, with SCG showing the lowest R value of 0.92 in supine position and 0.22 in seated position. Non-linear indexes also demonstrated strong correlations, except for the SampEn, which ranged from 0.19 to 0.40. Among other non-linear measurements, the SD1/SD2 ratio showed the lowest correlations in both seated and supine posture. Considering the comparison with the analysis conducted using conventional axes, it emerged that selecting optimized axes resulted in stronger correlations with reference ECG values than those achieved with literature-based axes, particularly in the supine position.

The findings presented in this section highlight the potential of IMU sensors for capturing mechanical signals and deriving both linear and non-linear HRV indexes. The subsequent section explores another application of IMU-based measurements in clinics: the classification of AS.

3.3. IMU applications for aortic stenosis classification

AS is among the most common valvular heart diseases, particularly affecting the elderly population [262]–[264]. This condition is defined by a progressive narrowing of the aortic valve, which obstructs blood flow from the heart into the systemic circulation. Clinically, it manifests with symptoms such as fatigue, chest pain (angina), and heart failure [265], [266].

Traditionally, AS diagnosis is primarily based on imaging techniques such as Doppler echocardiography, which allows for the quantification of parameters to classify disease severity [264], [267]. According to clinical guidelines, AS severity is classified as [268]–[270]:

- *Mild*: blood flow velocity < 3.0 m/s, the mean pressure gradient < 20 mmHg, and the aortic valve area (AVA) > 1.5 cm^2.
- M*oderate:* blood flow velocity between 3.0 m/s and 4.0 m/s, the mean pressure gradient between 20 mmHg and 40 mmHg, and AVA is between 1.0 and 1.5 cm^2.
- *Severe:* blood flow velocity > 4.0 m/s, a mean pressure gradient > 40 mmHg, and an AVA < 1.0 cm^2.

Although these diagnostic methods are robust and widely adopted, they have inherent limitations. These include high costs, reliance on specialized equipment and trained operators, and operator dependency, where diagnostic outcomes can vary depending on the individual conducting the procedure [271]. Their limited portability makes them less accessible for widespread or point-of-care use. Furthermore, AS is frequently diagnosed at advanced stages, emphasizing the need for more accessible and portable diagnostic systems to facilitate early detection [272].

In this context, IMU sensors offer a promising approach for evaluating cardiac mechanics and valve function through wearable technology. While these sensors have demonstrated utility in diagnosing various cardiac conditions including valve disorders, myocardial infarction, atrial fibrillation, and heart failure [202], [240], [273], [274], research specifically on AS classification remains limited. Current studies primarily rely on sensors placed on straps or bands around the thoracic cage, typically at the center of the sternum [246], [275]–[277]. This approach presents challenges in reproducibility across studies and is susceptible to placement errors and displacement during measurements. Furthermore, existing research on AS classification using cardio-mechanical recordings has consistently required synchronized ECG signals to interpret SCG and GCG patterns [246], [275]. This dependency limits the understanding of how SCG and GCG could be used independently for AS diagnosis. Previous research has also overlooked the potential benefits of exploring multiple sensor positions on the ribcage for signal acquisition.

This section introduces a novel approach employing multi-site SCG and GCG signal recordings from skin-interfaced IMU sensors placed at five thoracic locations. The method uses ML and DL techniques to distinguish AS patients from healthy controls, determine the best sensor positions, and explore whether combined SCG and GCG signals could provide ECG-independent AS diagnosis.

Methodology

Two distinct groups of participants were enrolled: 15 healthy individuals (4 males and 11 females, age: 26 ± 3 years, body mass: 61 ± 10 kg, BMI: 21 ± 2 kg/m²) and 15 patients diagnosed with AS (8 males and 7 females, age: 80 ± 12 years, body mass: 72 ± 14 kg, BMI: 26 ± 5 kg/m²). Among the AS patients, 14 had severe AS, and one had moderate AS, as determined through echocardiographic evaluations by specialized clinicians. Following established clinical guidelines, these assessments included hemodynamic measurements during left heart catheterization.

Cardiac-induced accelerations and angular velocities were recorded using commercial IMU sensors (Xsens Technologies B.V., Enschede, Netherlands) positioned at five cardiac auscultation points on the thorax: the AV, PV, MV, TV, and X. An expert physician placed all sensors to ensure consistent positioning across subjects. Each sensor embeds a triaxial accelerometer and a triaxial gyroscope, allowing simultaneous recording of SCG and GCG signals along three axes: x (cranio-caudal), y (latero-lateral), and z (antero-posterior or dorsoventral). The sampling rate was 120 Hz.

Data for the healthy group were collected at the University Campus Bio-Medico di Roma. Participants were instructed to lie supine while SCG and GCG signals were recorded for 120 s. For the AS group, data acquisition occurred during cardiac catheterization procedures before transcatheter aortic valve implantation (TAVI) at the Cardiology Unit of the Fondazione Policlinico Universitario Campus Bio-Medico di Roma. Signal acquisition coincided with intracardiac pressure measurements. From the one-hour recordings, 120 s

segments were selected, ensuring both minimal motion artifacts and clear cardiac peaks. A schematization of the experimental setup and protocol is depicted in Figure 3.5.

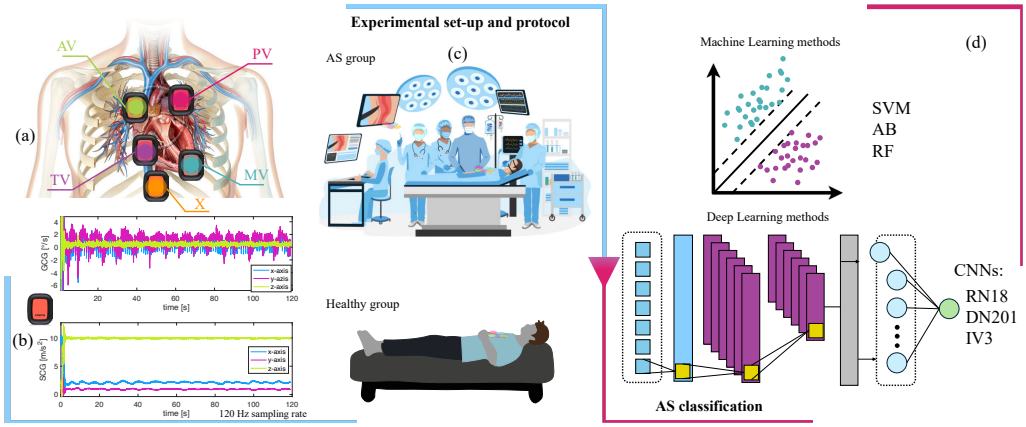

Figure 3.5. Experimental setup (a) and protocol (b) used for testing AS patients and the healthy group. Additionally, the ML and DL techniques employed for data analysis are illustrated (d). Adapted from [278].

The SCG and GCG signals underwent preprocessing using MATLAB 2023a. A finite impulse response (FIR) band-pass filter with cut-off frequencies of 0.1 Hz and 30 Hz was applied to isolate cardiac mechanical activity [98]. The filtered signals were then resampled to 60 Hz, reducing computational complexity. For analysis, the signals were segmented into overlapping frames using 10 s windows with 80% overlap, resulting in a 2 s shift between consecutive segments. This process divided each 120 s recording into 56 frames, with each frame containing data from all three axes. These frames served as independent samples for subsequent analysis.

Frequency and time-frequency domain features were extracted from the segmented signals. PSD analysis provided frequency-domain features, while the short-time Fourier transform (STFT) generated time-frequency representations. The STFT employed a frequency resolution of 1/3 Hz and subframes of 3 s with a 98% overlap, producing three-dimensional tensors containing time-frequency and amplitude information across all axes. The PSD features comprised 90 components, while the STFT representations were structured as 3D tensors.

For classification between AS patients and healthy controls, both classical ML and DL techniques were employed. Classical ML methods included support vector machines (SVMs) with Gaussian kernels and ensemble-based techniques such as random forests (RF) and AdaBoost (AB), which were applied to PSD-derived features from SCG and GCG signals. For DL analysis, convolutional neural networks (CNNs) were trained on STFT-derived features. Pre-trained architectures, including ResNet18, InceptionV3, and DenseNet201, were fine-tuned for binary classification. Transfer learning was employed to adapt these networks, modifying their final layers for the task at hand and fine-tuning preceding layers with the training data. A score-fusion strategy was implemented to combine SCG and GCG data. Separate networks were trained on each signal, and their normalized prediction scores were averaged to produce a single classification decision for each frame.

Results

This study aimed to evaluate how well SCG and GCG signals could classify AS patients versus healthy individuals, using the signals both separately and together. A 5-fold cross-validation approach was employed to ensure the robustness of the results and the generalizability of the developed models. In each fold, the data were split into three parts: 70% for training (21 subjects), 10% for validation (3 subjects), and 20% for testing (6 subjects). The testing set remained separate from the training and validation data.

Table 3.4: Recognition performance, in terms of accuracy (mean ± standard deviation, in %), for a single frame lasting 10s used as a probe, considering SCG and GCG sensors placed at different positions, and different classifiers. The best-performing results for each input type and sensor position are highlighted in bold.

Signal	Position	Classifier					
		SVM	RF	AB	RN18	IV3	DN201
SCG	PV	**80.8±5.6%**	77.7±6.0%	77.3±6.8%	78.1±6.2%	75.7±7.7%	77.5±6.8%
	AV	**77.7±7.1%**	67.4±6.0%	69.4±6.9%	72.9±5.6%	68.7±6.8%	69.1±7.8%
	X	**74.5±6.9%**	67.1±5.9%	62.7±8.5%	69.1±6.6%	67.3±7.1%	62.7±7.6%
	MV	**92.3±3.9%**	86.2±2.7%	84.6±3.3%	86.5±3.9%	84.1±3.6%	85.8±4.3%
	TV	75.5±6.6%	72.9±6.3%	75.9±6.2%	**77.4±6.1%**	73.7±7.4%	73.4±6.7%
GCG	PV	**92.1±3.4%**	82.1±3.8%	82.4±5.5%	84.1±4.6%	83.2±3.9%	84.5±4.2%
	AV	**83.4±6.8%**	79.1±5.2%	78.5±5.8%	79.6±4.7%	78.9±4.0%	78.1±5.2%
	X	**84.7±5.4%**	78.4±7.3%	75.4±8.0%	79.2±3.3%	78.9±3.8%	81.9±3.6%
	MV	74.9±4.5%	72.4±2.6%	76.2±3.5%	**78.3±6.3%**	78.1±7.7%	75.5±8.7%
	TV	83.9±3.4%	79.5±6.2%	79.0±4.8%	**85.1±4.9%**	84.8±5.3%	83.8±5.6%
SCG+GCG	PV	**92.8±3.2%**	83.1±3.4%	85.5±4.7%	85.7±5.1%	89.8±4.1%	86.9±4.4%
	AV	**84.6±5.6%**	79.8±5.4%	78.7±5.7%	82.3±4.8%	82.8±4.5%	81.2±5.4%
	X	**85.0±4.9%**	80.2±5.8%	78.4±7.2%	79.6±3.8%	81.4±4.1%	79.9±4.2%
	MV	**93.5±2.6%**	86.8±1.9%	87.1±2.8%	87.6±4.5%	85.5±4.2%	86.7±4.8%
	TV	84.1±3.6%	81.9±4.9%	84.6±4.4%	86.1±4.1%	**87.6±5.9%**	86.4±5.8%

Table 3.4 shows that SCG signals achieved the highest classification accuracy at the MV position, while GCG signals performed best at the PV position. GCG signals generally outperformed SCG signals across most sensor locations. Combining SCG and GCG data enhanced classification performance and reduced positional variability. The PV and MV positions proved most effective, integrating accelerometer and gyroscope data achieving consistent performance across all placements.

Statistical analysis using ANOVA and Tukey's honest significant difference (HSD) tests revealed several findings. For SCG signals at the MV position, ANOVA showed significant differences ($p = 2.18\%$) between the SVM classifier and other methods. Similarly, for GCG signals at the PV position, ANOVA ($p = 1.15\%$) indicated significant differences between SVM and other classifiers. Combined SCG and GCG data analysis at PV and MV positions ($p = 1.84\%$ and 2.79%, respectively) showed significant differences between SVM and RF at PV and between SVM and all classifiers except RN18 at MV.

Further ANOVA testing examined sensor placement effects on classification accuracy. SCG signals showed significant differences ($p = 0.14\%$) between MV and other positions, while GCG signals revealed significant

differences (p = 1.45%) between PV and MV positions. Combined SCG-GCG data analysis (p = 1.28%) showed significant differences between PV/MV and AV positions, emphasizing the importance of optimal sensor placement.

A final enhancement attempt combined SVM and RN18 classifiers by normalizing and summing their independent prediction scores. As detailed in Table 3.5, this approach improved classification performance, particularly at PV and MV positions. ANOVA testing (p = 0.96%) confirmed significant performance differences between PV/MV and AV positions.

Table 3.5: recognition performance, in terms of accuracy (mean ± standard deviation, in %), for a single frame lasting 10 s used as probe, jointly exploiting SCG and GCG signals, and both SVM- and RN18-based classifiers.

Position	Accuracy	Precision	Recall	F1-score
PV	93.9±3.2%	95.37±2.0%	92.1±4.8%	93.5±3.5%
AV	85.2±5.1%	86.35±6.1%	87.1±5.6%	85.6±4.5%
X	87.2±5.7%	86.03±5.9%	89.5±4.9%	87.7±5.4%
MV	93.7±2.7%	96.18±2.1%	90.9±4.4%	93.3±2.9%
TV	87.5±3.8%	87.24±5.1%	89.2±3.3%	87.8±4.0%

Subsequently, how higher acquisition durations affected classification accuracy was evaluated. While previous results used 10 s SCG and GCG frames (obtained through signal windowing), calculating prediction scores with longer-duration frames enhanced model robustness. Figure 3.6 shows that 40 s acquisitions achieved classification accuracies above 95% for data from PV and MV positions. X and TV positions reached accuracies above 90% at this duration, while the AV position showed consistently lower classification performance. These results show that longer recording durations and optimal sensor positioning are important for accurate diagnostic results.

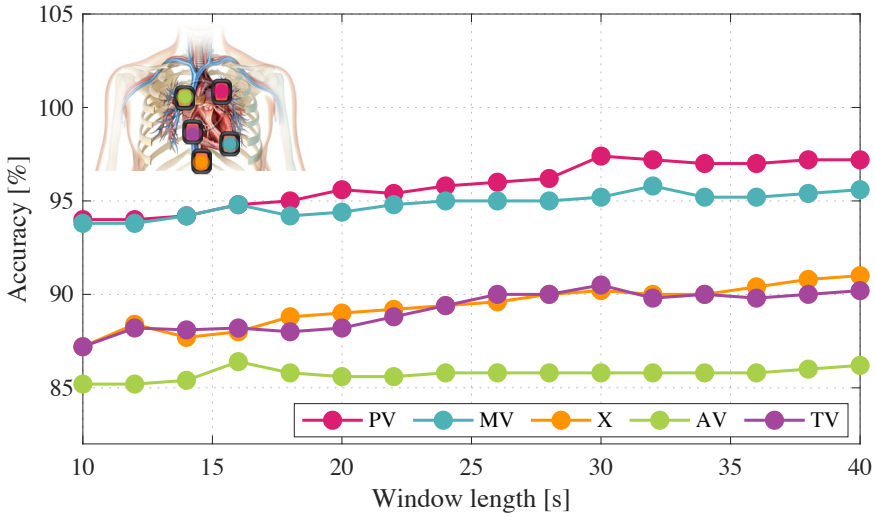

Figure 3.6. Mean recognition accuracies obtained from cross-validation tests for increasing probe durations, leveraging SCG and GCG signals as inputs to SVM- and RN18-based classifiers. The results from different frame analyses are combined at the score level. Adapted from [278].

3.4. Conclusions

This chapter explored the potential of IMU sensors in cardiac monitoring in clinical field, focusing on two applications: HRV analysis and the classification of AS.

In HRV analysis, the findings demonstrated that IMU sensors can derive both linear and non-linear HRV indexes from mechanical signals. The results revealed strong correlations with ECG-derived reference values, particularly in the supine posture. These results highlight the feasibility of IMUs for continuous HRV monitoring, with potential applications in evaluating autonomic nervous system function, stress resilience and cardiovascular rehabilitation.

In AS classification, IMU sensors placed at different locations on the chest wall demonstrated significant diagnostic potential by integrating ML and DL techniques. When analyzing SCG and GCG signals individually, the highest classification performance was achieved at the PV and MV locations using SVM and RN18 with a measurement duration of 10 s. Combining SCG and GCG

signals led to a slight enhancement in classification performance, with the best results still observed at PV and MV using SVM with a 10 s measurement window. Additionally, extending the measurement duration further increased classification accuracy. The best overall results were obtained with a 40 s measurement window, leveraging both SCG and GCG signals jointly at the PV and MV locations, using a combination of SVM and RN18. The classification of AS in this study was based on comparisons between subjects with severe stenosis and healthy individuals, which limits the assessment of its ability to distinguish AS from other cardiovascular conditions. While the results highlight the potential of IMU sensors for AS detection, further studies are required to validate their diagnostic capabilities across a broader spectrum of cardiac disorders. Expanding the dataset to include individuals with mild to moderate AS, as well as those with other cardiac pathologies, would provide a more comprehensive evaluation of the method's specificity and clinical applicability.

4

Chapter 4: Wearable Sensors for Respiratory Monitoring in Sports Science

4.1. Introduction

Respiratory monitoring holds significance in sports science, providing information about athletes' physical performance, recovery, and overall well-being. The RR, in particular, although often overlooked, has gained recognition as an important physiological variable due to its strong association with perceived exertion and exercise tolerance [279], [280]. Unlike other parameters such as HR or oxygen uptake, RR responds rapidly to changes in exercise intensity, providing real-time feedback on physical effort, especially during intermittent and high-intensity activities [131], [281]. This makes RR particularly relevant for sports characterized by variable workloads, such as cycling, soccer, and other team sports. Additionally, RR is modulated by non-metabolic factors and is considered the behavioral component of minute ventilation, offering information from tidal volume that is, instead, influenced by metabolic inputs [67], [282], [283]. Despite its many advantages, monitoring respiratory activity has been often neglected in sport due to the limited availability of devices capable of measuring it without impeding the athlete's movement. Furthermore, many commonly available commercial devices fail to provide sufficiently accurate measurements.

The increasing availability of WDs has transformed how respiratory parameters are monitored in sports. WDs can measure continuously RR in real-world settings, overcoming the traditional limitations of laboratory-based methods [127], [284]. Among the various approaches, sensors that measure breathing activity from chest wall movements, such as strain-based, capacitive, or inductive sensors, are gaining popularity [17], [186], [285]–[289]. They are commonly integrated into garments or straps, providing an unobtrusive way to monitor RR during physical activities.

Despite their promise, the use of WDs for respiratory monitoring in sports presents several challenges. Motion artifacts caused by dynamic activities, such as running or sudden changes in direction, can affect signal quality. Furthermore, different sports introduce challenges to sensor performance, requiring sport-specific validation of these technologies. Additionally, WDs often struggle to capture breath-by-breath rapid RR variations during training sessions with fluctuating intensity, limiting their effectiveness in dynamic sports scenarios. This issue becomes increasingly relevant with the growing interest in voluntary modulation of breathing patterns during exercise, where breath-by-breath RR estimation plays an important role in understanding performance adaptations [290], [291].

This chapter delves into the development and application of WDs for respiratory monitoring in sports, with a particular emphasis on overcoming the challenges posed by dynamic, real-world scenarios. These challenges are tackled through two distinct approaches.

The first approach (presented in Section 4.2) involves the development of a smart facemask designed to minimize the influence of motion artifacts on the respiratory signal. The objective of this approach is to propose a system that ensures high accuracy in RR measurement by minimizing the impact of motion artifacts. This is achieved by positioning the sensor close to the airways, allowing the system to monitor airflow directly rather than relying on body

deformations that are more susceptible to noise. Additionally, the design prioritizes user comfort, ensuring minimal interference with athletic performance and making it suitable for real-world sports applications. However, due to its placement, it may be less practical for extended use due to potential discomfort during prolonged or high-intensity activities.

The second approach (presented in Section 4.3) focuses on improving signals collected with chest-worn devices, which are widely used in sports due to their accessibility and comfort. These devices, however, often fail to provide useful information, such as breath-by-breath RR, and their measurements can lack accuracy. To address these limitations, new algorithms have been developed and implemented, extending the devices' capability to provide more accurate RR values.

Through these complementary solutions, the chapter outlines a strategy to address the limitations of respiratory monitoring in sports contexts, offering advancements for dynamic, real-world applications.

4.2. Design and development of a smart facemask for respiratory monitoring in sports

The accurate monitoring of RR during physical activities is useful for understanding an athlete's physiological responses and optimizing performance. While traditional methods for RR measurement are effective in controlled laboratory environments, their limitations in real-world sports settings have driven the development of new wearable solutions. Among these, facemasks equipped with integrated sensors offer an advantage by positioning the sensing elements close to the airways [292], [293]. This placement enables direct monitoring of airflow, reducing the susceptibility to motion artifacts that affect chest-mounted devices [127].

The development of a smart facemask for sports applications requires a consideration of both sensor performance and user comfort. To ensure minimal

interference with athletes' performance, the facemask design must balance accuracy with ergonomic principles, enabling athletes to wear the device during high-intensity activities without discomfort. This section details the design and working principle of a smart facemask, the laboratory bench tests performed to assess its performance, and the validation studies conducted with cyclists under real-world conditions. These steps aim to demonstrate the effectiveness of the facemask in providing reliable RR measurements during dynamic and demanding sports scenarios.

4.2.1. Design and working principle

The system comprises four main units, as shown in Figure 4.1, and as detailed below.

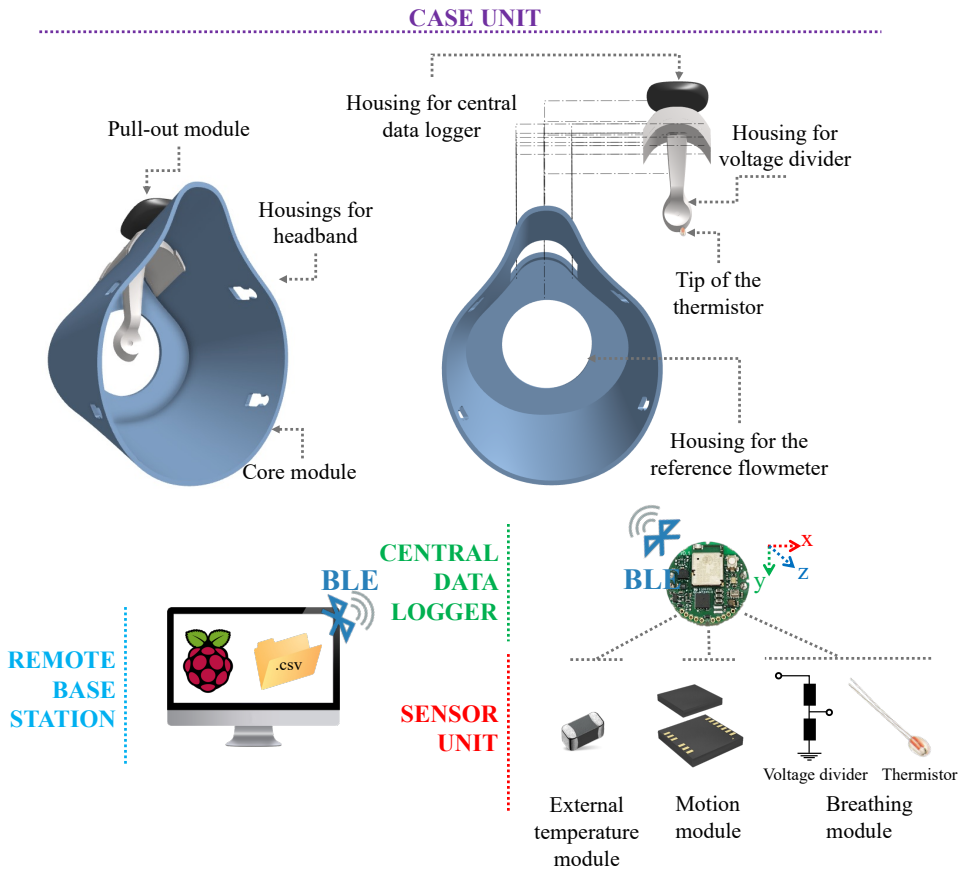

Figure 4.1: Diagram of the system architecture showing the main components (remote base station, central data logger, sensor unit, and case unit) along with their respective modules. Adapted from [294].

1. Sensor Unit: comprising three modules:

- A breathing module featuring an NTC (negative temperature coefficient) radial glass thermistor (G10K3976B1), designed to monitor respiratory activity by measuring the temperature of exhaled air (T_{Exp}).
- A motion module with a triaxial accelerometer (Bosch BMI160).
- An external temperature module consisting in a temperature sensor (NCP15XH103F03RC) to record ambient temperature (TE).

2. Central Data Logger: a lightweight electronic board that integrates Bluetooth Low Energy technology, the motion module, and the external temperature module. Also, it has an internal memory to store data collected at a sampling frequency of 50 Hz.

3. Remote Base Station: a Raspberry Pi system for managing the central data logger and store data.

4. Case Unit: designed with two detachable modules:

- The pull-out module, a 3D-printed 'spoon-shaped' housing for the sensor unit and data logger.
- The core module, a 3D-printed facemask made from thermoplastic polyurethane (TPU), was designed to hold the pull-out module. It has been realized with a 40 mm diameter front hole to minimize airflow resistance. It is washable and equipped with adjustable headbands for a proper fit.

The subsequent discussion focuses solely on the components related to the respiratory monitoring, excluding the motion module.

The operating principle relies on monitoring breathing by detecting temperature variations experienced when breathing module is exposed to the respiratory airflow. At this aim, the smart facemask integrates a temperature sensor embedded into the pull-out module. Its design ensures that most of the

exhaled airflow is channeled directly toward the temperature sensor, maximizing its interaction with the respiratory airflow and enabling the detection of temperature variations caused by it. The sensor operates based on its resistance (R), which varies inversely with temperature (T). In the absence of T_{Exp}, such as when the facemask is not worn or during apnea, the respiratory module is exposed solely to TE, resulting in stable T and R signals. During exhalation, the sensor detects airflow at a temperature close to the T_{Exp}, approximately 37 °C. The functional behavior of the facemask during the expiratory phase can thus be described as follows:

- If $T_{Exp} > T_E$, the resistance of the respiratory module decreases.
- If $T_{Exp} < T_E$, the resistance of the respiratory module increases.
- If $T_{Exp} = T_E$, the resistance of the respiratory module remains stable.

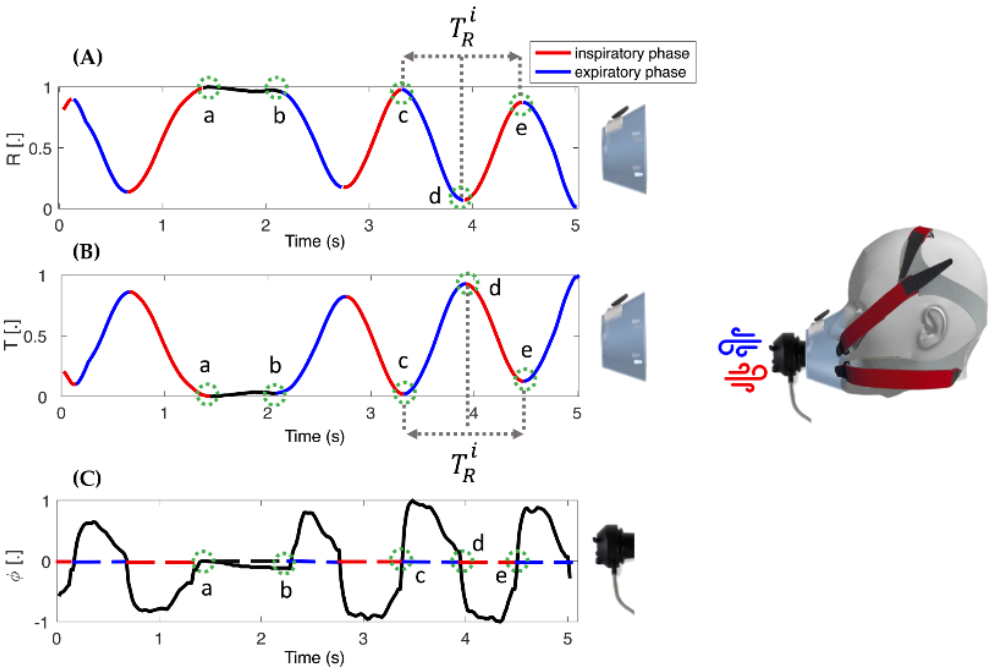

Figure 4.2: Example of a normalized resistance signal (A) and the corresponding normalized temperature signal (B) recorded during breathing with the smart facemask. The normalized signal (C) was collected from the reference flowmeter used for validation. In all signals, the segment a–b shows the end-inspiratory apnea, c–d represents the expiratory phase, and d–e marks the inhalation phase. Adapted from [294].

During the inhalation phase, the temperature sensor is once again exposed to TE, making this a 'passive' phenomenon. A schematization of the main characteristics of the R and T signals is reported in Figure 4.2.

4.2.2. Laboratory bench test

To validate the feasibility of the smart facemask for RR monitoring, preliminary tests were conducted under controlled laboratory conditions to simulate a wide range of RR values. Specifically, the system's performance was examined at different simulated respiratory flows ranging from 5 brpm to 75 brpm in steps of 10 brpm. Per each imposed frequency 10 breaths were simulated. A mechanical ventilator (SERVO VENTILATOR 300, SIEMENS) generated airflow simulating the breaths. This airflow was then heated and humidified using a humidifier (MR850ALU, Fisher&Paykel HEALTHCARE), ensuring a temperature of 37 °C and 100% relative humidity.

The system was set up by enclosing the facemask in a polylactic acid (PLA) box, as schematized in Figure 4.3. To maintain stable conditions and minimize the influence of external temperature, it was kept constant at approximately 25°C. Airflow from the mechanical ventilator and humidifier entered through the front opening of the box, interacted with the thermistor in the facemask, and exited through the rear opening connected to a lung simulator. The simulator captured and returned the flow to the ventilator, creating a closed-loop system.

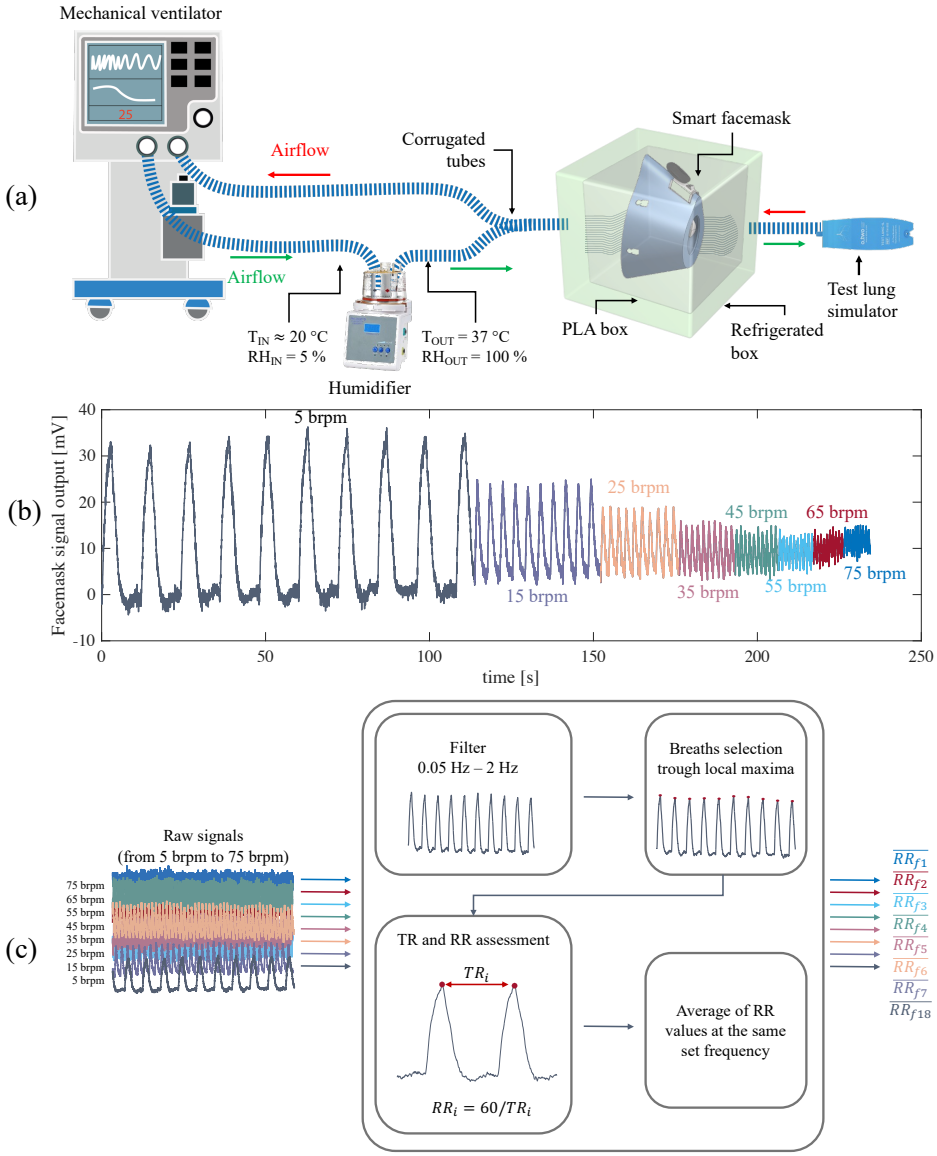

Figure 4.3: schematization of the experimental setup (a) used for the in-laboratory testing of the smart facemask. Also, the signal collected during the bench test (b) and the signal processing steps (c) are reported. brpm: breaths/min Adapted from [294].

The signal collected with the facemask was band pass filtered between 0.01 Hz and 2 Hz, a range that captures typical RR values (from 0.6 brpm to 90 brpm) while reducing low-frequency drift and high-frequency noise. Then end-expiratory peaks, identified as local maxima in the T signal, were detected using amplitude and time thresholds. Peaks exceeding 2% of the maximum peak-to-peak amplitude and separated by at least 0.5 s were classified as valid breathing events. The respiratory period (TR) was calculated as the time interval between

consecutive events, and the breath-by-breath RR was determined as 60/TR. Then, the average RR for each test was calculated and compared to the target values set on the mechanical ventilator. The measured values were reported as:

$$RR_{measured} = \overline{RR} \pm \delta RR \quad (4.1)$$

where $\overline{RR}$ represents the average value of the measurements, and δRR is the uncertainty[5] calculated using Student's distribution at a 95% confidence level[6].

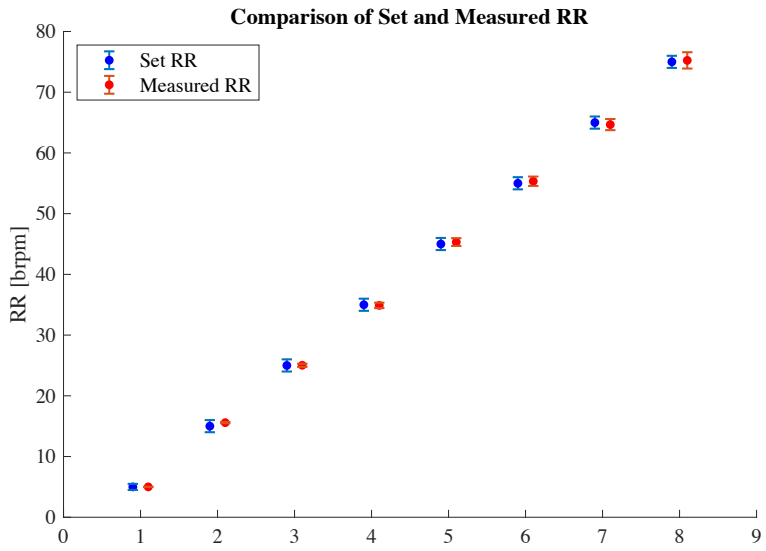

Figure 4.4: Comparison between RR values set on a mechanical ventilator (Set RR) and those measured by the smart face mask (Measured RR). Error bars represent mean±uncertainty; brpm: breaths/min. Adapted from [294].

The results presented in Figure 4.4, indicate a strong agreement between the RR values set on the mechanical ventilator and those measured by the smart facemask.

5. *According to the Guide to the Expression of Uncertainty in Measurement (GUM), uncertainty is defined as "a parameter associated with the result of a measurement that characterizes the dispersion of the values that could reasonably be attributed to the measurand."* [295].

6. *Confidence level is defined as the value (1 − α) of the probability associated with a confidence interval or a statistical coverage interval* [295].

Across all tested frequencies, the measured values closely align with the set reference values, exhibiting minimal uncertainty and no noticeable discrepancies. These findings validate the accuracy and reliability of the smart facemask in measuring RR, establishing a basis for its further evaluation under real-world conditions

4.2.3. Validation during cycling

Indoor experiments

To assess the performance of the wearable system in a real scenario, the smart facemask was tested on ten healthy, trained male cyclists (mean ± standard deviation: age 25 ± 6 years, body mass 68 ± 6 kg, height 174 ± 5 cm). The validation tests were carried out indoors on a cycle ergometer (WattBike Pro, Nottingham, UK) at an average ambient temperature of about 26°C. A gold-standard flowmeter (Quark PFT, COSMED S.r.l., Rome, Italy) was integrated into the mask's core module as the reference device for measuring respiratory airflow (sampling frequency 50 Hz). The experimental setup and protocol are illustrated in Figure 4.5.

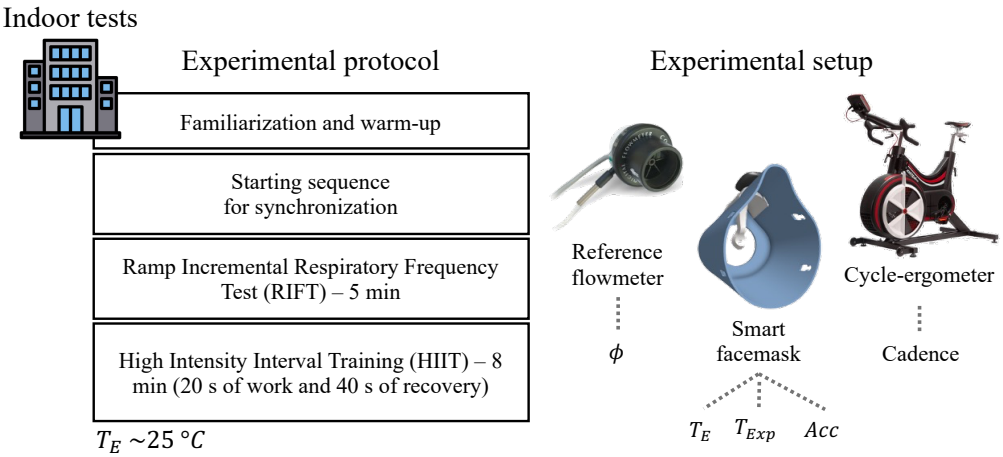

Figure 4.5: experimental setup and protocol carried out during the indoor tests of the smart facemask on cyclists. Adapted from [294].

After the warm-up and synchronization phases, the participants completed two exercise protocols separated by a recovery period lasting 3 min:

1. Ramp Incremental Respiratory Frequency Test (RIFT): Participants synchronized their breathing to a metronome that progressively increased the RR from 20 brpm to 75 brpm in an exponential pattern over a 5 minute test. During this protocol, they cycled at a self-selected pedaling cadence and power output while adhering to the prescribed breathing rhythm.

2. High-Intensity Interval Training (HIIT): this protocol consisted of eight repetitions of 20 s of high-intensity work followed by 40 s of recovery. During the work phase, cyclists self-selected their power output to reach a perceived exertion level of approximately 19 on Borg's 6–20 scale by the final repetition [296].

Before data analysis, the signals recorded by the smart facemask were synchronized with the reference flowmeter signal, by cutting them from the third deep breath in the starting sequence. The reference signal generates a pseudo-periodic waveform, where the negative phase represents inspiration, and the positive phase corresponds to expiration (see Figure 4.2C). To align its pattern with the waveform produced by the facemask sensor, the reference signal was integrated to derive a similar volume signal. Both reference and facemask signals were then processed using two different algorithms for RR extraction:

- the first algorithm identifies TRs using the same method based on amplitude and time thresholds as described in the bench tests. These TRs are then used to calculate breath-by-breath RR values across the entire signal.
- the second algorithm builds on the first approach by applying it within non-overlapping 30 s windows. Hence, within each window, it calculates breath-by-breath RR values and then computes the average RR for that specific window.

While this last method reduces the influence of outliers or artifacts in the signal, it comes at the cost of losing detailed information, making it less effective for capturing sudden changes in RR.

For both the algorithms, the performance of the smart facemask was assessed considering the MOD and the LOA values found through Bland-Altman analysis. Moreover, MAE and MAPE values, were calculated, as reported in Table 4.1 and Table 4.2.

Table 4.1: Breath-by-breath analysis results: (A) RIFT test and (B) HIIT test

(A) Breath-by-breath analysis – RIFT test					**(B) Breath-by-breath analysis – HIIT test**				
Cyclist	#breathing events	Bias [MOD ± LOAs] [brpm]	MAE [brpm]	MAPE [%]	Cyclist	#breathing events	Bias [MOD ± LOAs] [brpm]	MAE [brpm]	MAPE [%]
1	173	-0.02±2.57	0.89	2.30	1	320	-0.04±3.85	1.00	2.54
2	177	-0.01±2.50	0.93	2.48	2	271	-0.01±1.68	0.60	1.29
3	174	-0.23 ±4.84	1.02	2.60	3	416	0.00±2.00	0.68	1.22
4	175	-0.01±2.92	1.10	2.74	4	290	-0.03±2.26	0.85	2.33
5	179	-0.03±4.62	1.75	4.50	5	245	-0.01±2.31	0.77	2.58
6	174	-0.02±2.58	0.75	1.82	6	283	0.00±1.40	0.50	1.43
7	179	-0.01±2.08	0.66	1.72	7	306	-0.04±1.32	0.48	1.13
8	179	-0.12 ±2.68	1.05	2.74	8	331	-0.03±1.85	0.59	1.48
9	174	-0.11 ±2.87	0.98	2.34	9	362	-0.06±3.43	0.75	1.67
10	174	-0.02±2.52	0.84	2.31	10	377	0.00±2.25	0.66	1.28
Overall	**1758**	**-0.05±3.37**	**1.00**	**2.56**	**Overall**	**3301**	**-0.02±2.37**	**0.69**	**1.64**

Table 4.2: Window analysis results: (A) RIFT test and (B) HIIT test

(A) Window analysis – RIFT test					**(B) Window analysis – HIIT test**				
Cyclist	#breathing events	Bias [MOD ± LOAs] [brpm]	MAE [brpm]	MAPE [%]	Cyclist	#breathing events	Bias [MOD ± LOAs] [brpm]	MAE [brpm]	MAPE [%]
1	10	-0.03±0.31	0.10	0.28	1	16	-0.13 ±0.28	0.14	0.38
2	10	-0.01±0.26	0.10	0.34	2	16	-0.01±0.14	0.06	0.13
3	10	-0.10±0.42	0.17	0.58	3	16	-0.06±0.43	0.09	0.16
4	10	-0.04±0.29	0.10	0.27	4	16	-0.03±0.15	0.07	0.19
5	10	-0.02±0.54	0.18	0.62	5	16	0.00±0.20	0.08	0.27
6	10	-0.05±0.12	0.06	0.20	6	16	0.00±0.10	0.04	0.13
7	10	-0.02±0.15	0.06	0.19	7	16	0.04±0.53	0.12	0.30
8	10	-0.16 ±0.22	0.09	0.27	8	16	-0.02±0.13	0.06	0.15
9	10	-0.04±1.16	0.30	0.75	9	16	0.01±0.78	0.19	0.39
10	10	0.00±0.19	0.07	0.25	10	16	-0.07±0.28	0.09	0.19
Overall	**100**	**-0.02±0.45**	**0.12**	**0.37**	**Overall**	**160**	**-0.03±0.37**	**0.09**	**0.23**

Outdoor experiments

Outdoor tests were conducted to assess whether the reduced temperature gradient between TE and T_{Exp} affects the performance of the smart facemask. A subset of participants underwent RIFT and HIIT protocol. These tests took place in an environment where TE is about 32 °C, a value closer to the exhaled air temperature compared to the indoor setting. A schematization of the experimental setup and protocol used during the outdoor tests on cyclists is reported in Figure 4.6.

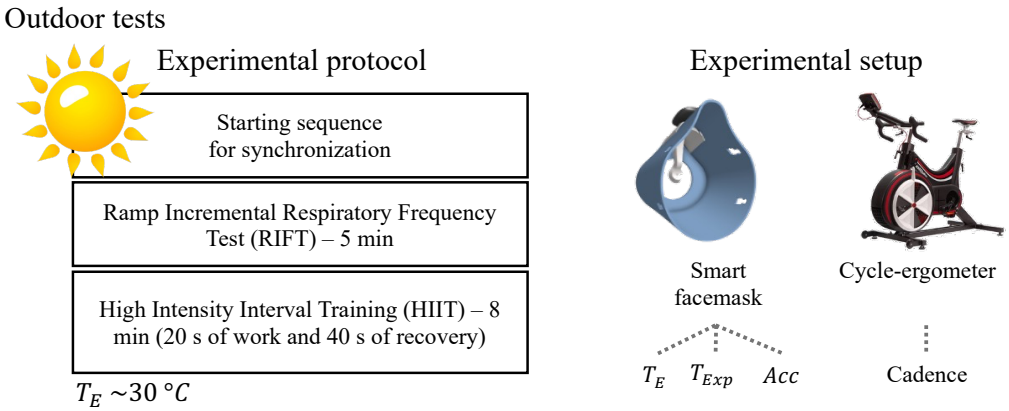

Figure 4.6. experimental setup and protocol carried out during the outdoor tests of the smart facemask on cyclists. Adapted from [294].

To evaluate the impact of TE on the facemask's performance, the amplitude (A) of the output signal recorded during the RIFT was compared between indoor and outdoor trials. For each test, A was calculated using the following formula:

$$A\,[mV] = \frac{1}{N}\sum_{i=1}^{N}(max_i - min_i) \qquad (4.2)$$

Where N is the number of respiratory cycles, while max_i and min_i represent the maximum and minimum voltage values of the i-th breath, respectively. In Figure 4.7 data for one volunteer across both settings are showed.

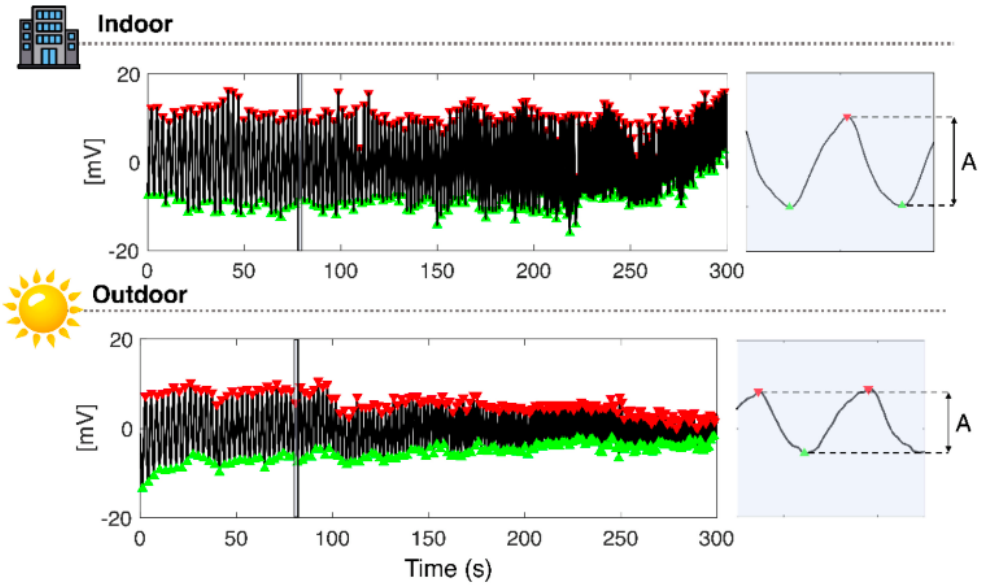

Figure 4.7: experimental setup and protocol carried out during the outdoor tests of the smart facemask on cyclists. Adapted from [294].

The figure above shows that although A was higher in the indoor trials due to the higher T gradient, the respiratory signal quality remained consistent in the outdoor environment. Figure 4.8 summarizes the mean values of TE, and A collected in the indoor and outdoor tests.

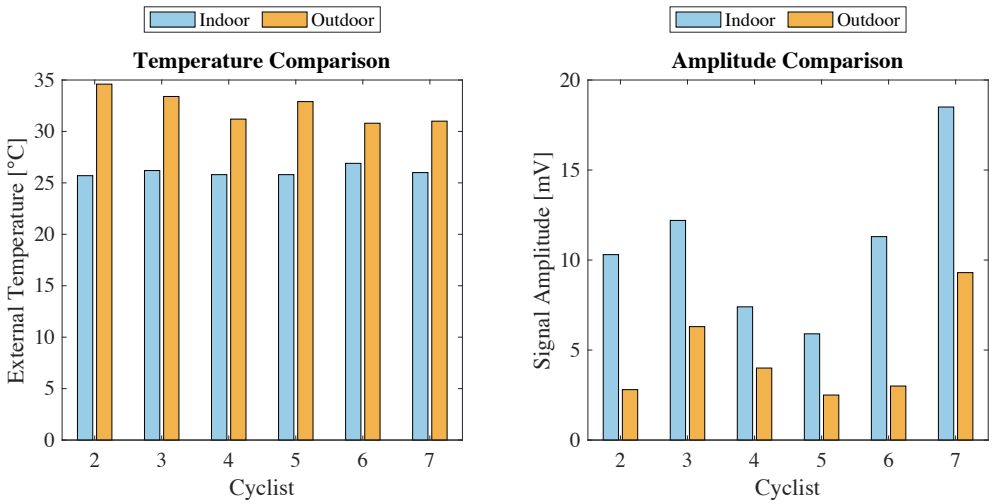

Figure 4.8: Average values of external temperature (TE) and signal amplitude (A) for each volunteer during indoor and outdoor tests.

Breath-by-breath RR values were calculated using the previously described first algorithm. During the outdoor RIFT test, the absence of a reference system

necessitated an initial evaluation of participants' ability to adhere to the target RR. In fact, deviations from the imposed RR could result from either the participants' inability to maintain the target or measurement errors from the test system. In the indoor trials, the Root Mean Square Error (RMSE) was computed for both the test system and the reference system. Comparable RMSE values between the two systems indicated that deviations were primarily attributable to participants' difficulty in adhering to the target RR rather than inaccuracies in the test system (see Figure 4.9A). Subsequently, RMSE values were calculated for the outdoor trials and compared with those from the indoor trials for the facemask (see Figure 4.9B and Figure 4.9C). This comparison facilitated an assessment of the test system's performance in outdoor conditions while accounting for participants' variability in maintaining the target RR.

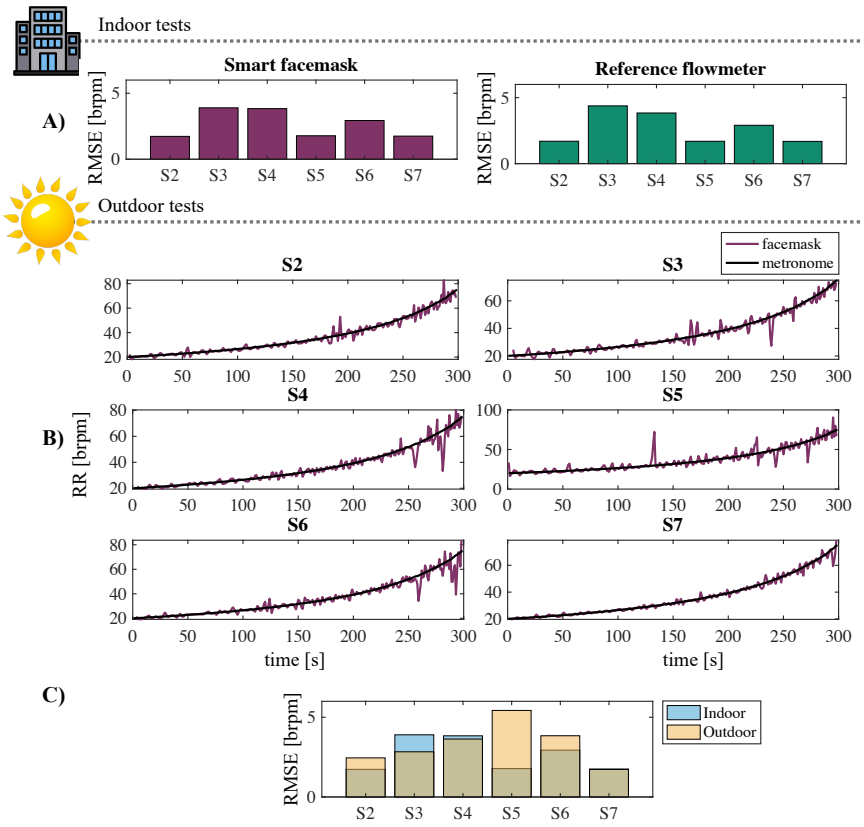

Figure 4.9. (A) RMSE values using the smart facemask and the reference system against the metronome during the RIFT in indoor tests; (B) RR values trend calculated using the smart facemask and the metronome during RIFT in outdoor tests; (C) RMSE values using the smart facemask against the metronome during RIFT in indoor and outdoor tests. Adapted from [294].

The RR responses observed during the RIFT tests, conducted both indoors and outdoors across all participants, demonstrated the facemask's ability to capture high-quality data. Specifically, the RR trends recorded during the RIFT tests closely matched the target RR imposed by the metronome. Additionally, the HIIT test results were analyzed, showing recorded RR patterns that accurately reflected the expected physiological responses to work and recovery phases (Figure 4.10) [283], [297].

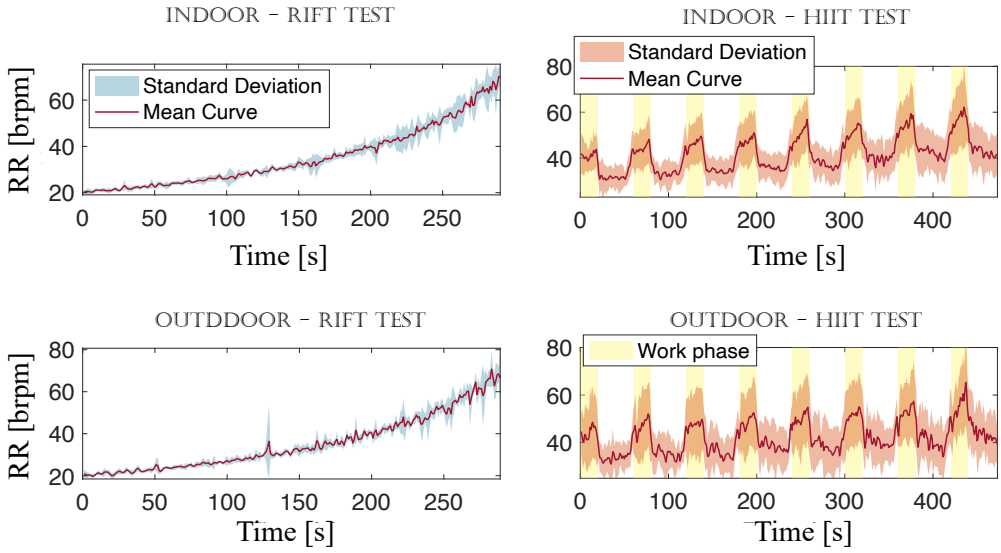

Figure 4.10: mean and standard deviation of RR values over time during RIFT and HIIT tests in indoor and outdoor setting. All the volunteers were considered inhis analysis. Adapted from [294].

The smart facemask addresses critical challenges in respiratory monitoring during high-intensity exercise, as evidenced by its performance in validation tests. These tests demonstrated low error rates, with a MAE below 1 brpm and a MAPE up to 2% for breath-by-breath analysis, even in dynamic conditions such as HIIT. Such levels of accuracy are rarely reported in validation studies of WDs, including commercial systems like the Zephyr™ BioHarness™ and the Hexoskin® smart shirt [298]–[300], as well capaciflector sensors and custom-made differential pressure sensor [301], [302]. Moreover, during HIIT, the facemask achieved MAPE values of 1.64% for breath-by-breath measurements

and 0.23% for 30 s averages, outperforming the previously reported values of 4.03% and 1.77%, respectively [302].

The smart facemask presented in the previous section offers high accuracy in RR monitoring by directly measuring airflow, enabling RR monitoring in real-world conditions, beyond controlled environments. However, its use in real-world sports settings can be limited by practical constraints, such as discomfort during prolonged and daily sports activities. These limitations highlight the need for alternative wearable solutions that prioritize comfort without compromising measurement accuracy. Chest-mounted devices, widely adopted in sports due to their unobtrusive design, represent a viable option; however, their reliance on signals derived from torso movements makes them more susceptible to motion artifacts.

Addressing this challenge requires the development of algorithms capable of extracting robust RR measurements. The next section explores the role of such algorithms in enhancing the performance of chest-mounted WDs, focusing on their impact during high-intensity sports and the development of a novel approach for motion artifact removal through signal morphology analysis.

4.3. The role of algorithms in respiratory frequency estimation in sports

In sports science, the accuracy of RR monitoring often depends on the robustness of signal processing algorithms, especially when WDs are used in dynamic and high-intensity activities. Unlike controlled laboratory settings, real-world sports scenarios involve challenges such as motion artifacts, rapid fluctuations in RR, and irregular breathing patterns. These factors complicate the extraction of high-quality respiratory signals, particularly for chest-mounted devices that rely on torso movements to infer respiratory activity.

Despite these limitations, chest-mounted wearables remain widely used in sports due to their comfort and practicality. However, their dependence on raw

respiratory signals highlights the need for algorithms to reduce noise and enhance accuracy. By analyzing the morphological characteristics of the respiratory signal, such algorithms can improve breath-by-breath RR estimation, which is important for understanding performance adaptations and optimizing training in sports with varying intensity, such as soccer.

This section investigates the impact of algorithms on RR estimation accuracy in sports, starting with a comparative evaluation of commercial chest-mounted devices during soccer-specific movements. Furthermore, an algorithm is introduced to remove motion artifacts by analyzing the morphological characteristics of the respiratory signal, enabling high-quality RR measurement even in the most challenging conditions. These advancements aim to bridge the gap between comfort and accuracy, enhancing through algorithms the performance of chest-mounted wearables for respiratory monitoring in sports applications.

4.3.1. Comparative evaluation of torso-worn wearables for breathing monitoring in soccer

Soccer greatly benefits from technological advancements. While GPS technology is widely used at elite levels to track metrics such as distance, speed, and changes in direction, individual responses to exercise are better captured by physiological variables, which reflect how players adapt to external loads [303]–[305].

Sensors that measure respiratory-induced torso movements are well-suited for monitoring breathing in soccer, as they can be integrated into straps or clothing worn during training and competitions. For instance, soccer players often wear vests equipped with GPS units, which can be integrated with strain sensors to monitor RR [306]. Various commercial strain sensors have been tested during exercise, including running [300], [307]–[309]. However, their effectiveness in measuring RR during soccer-specific activities has not been investigated. This is important because the quality of respiratory signals from

strain sensors is impacted by motion artifacts, which vary depending on the sport. In particular, soccer poses challenges due to rapid directional changes, torso rotations, and unorthodox movements, which can degrade signal quality [297]. Additionally, the dynamic nature of soccer requires breath-by-breath validation of sensors, as RR can fluctuate over short periods, making traditional window-based RR analysis approaches insufficient.

Experimental setup and protocol

Three different commercial WDs were investigated. Specifically, the Zephyr Bioarness™ (BH) strap (Medtronic, Boulder, CO, USA), the TymeWear™ (TW) vest (TymeWear™, Boston, MA, USA), and the ComfTech® (CT) vest (Howdy Senior, ComfTech s.r.l.®, Monza, Italy) were included. The wearable smart facemask presented in the previous section was used as reference device. Fifteen healthy male amateur soccer players (mean ± standard deviation: age 23 ± 4 years, height 176 ± 5 cm, body mass 69.1 ± 6.1 kg) were enrolled. All participants were free of recent injuries that could affect their performance. The study was approved by the Institutional Review Board of the University of Rome "Foro Italico" (CAR 149/2023) and conducted in accordance with the Declaration of Helsinki, with written informed consent obtained from all participants.

A validation protocol lasting 30 min was designed to assess the performance of the three devices during soccer-specific activities. Synchronization between the commercial sensors and the reference signal was ensured asking the volunteers to perform three fast, deep breaths followed by 5 s of apnea performed before each phase of the protocol. This last consisted of four main phases:

1. RIFT test (5 min): participants ran at a moderate self-paced speed while following a metronome-paced breathing track, with RR ranging from 15 brpm to 75 brpm. The inspiratory and expiratory phases were differentiated by distinct tones, delivered through in-ear headphones connected to a smartphone.

2. Ball warm-up (5 min): this phase simulated typical soccer movements, such as passing and running with the ball, to evaluate the devices' performance during classical soccer activities.

3. Shuttle run intermittent test (9 min): consists of 12 shuttle runs with 15 s of work followed by 30 s of passive recovery. The phase was designed to assess the devices' ability to capture rapid changes in RR during alternating work-rest periods typical of soccer.

4. Cool-down phase (5 min): a slow recovery run was included to evaluate the devices' performance during a period of gradual recovery.

Data analysis and results

All the signals were synchronized with the reference device by cutting them from the end of the apnea performed during the synchronization maneuvers. Then a first order Butterworth bandpass filter (cutoff frequencies 0.01 Hz – 2 Hz) was applied on both reference and chest-worn wearables, to retain the frequency range typical of respiratory activity during exercise and remove noise.

To extract breath-by-breath RR values, algorithms were used to identify respiratory cycles based on time and amplitude thresholds, as detailed above. Since the signal amplitude varied across trials, a 12 s moving window with a 2 s overlap was applied to normalize and detrend the signal, removing unrelated drifts. The windows were used solely for signal processing, and no averaging of RR values was performed within the windows; instead, breath-by-breath RR values were computed. An example of the main steps of data analysis is reported in Figure 4.11.

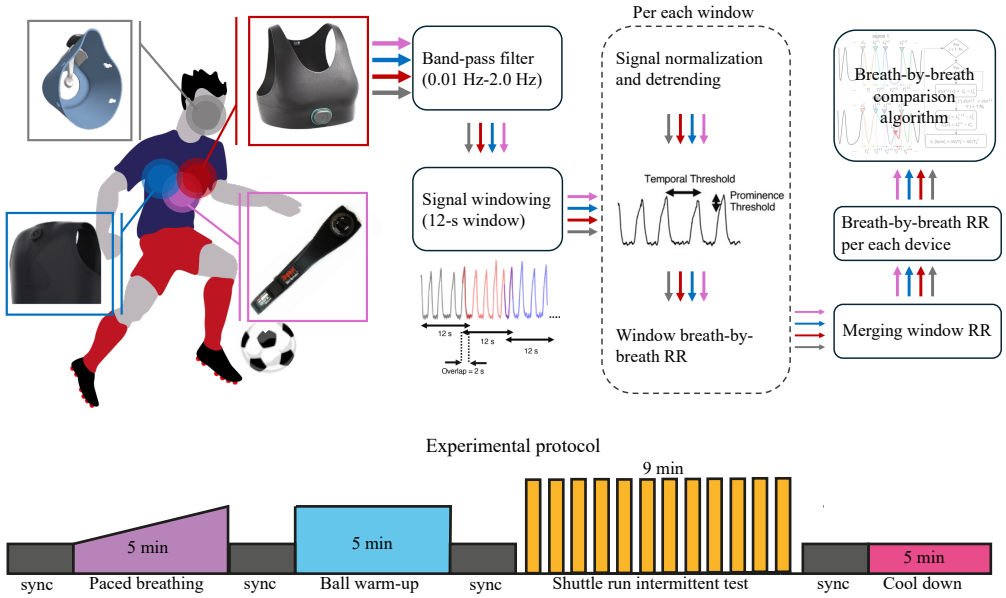

Figure 4.11: Experimental setup, protocol and main steps carried out for data analysis. Adapted from [310].

The temporal threshold was set at 0.5 s, while the amplitude criterion (based on peak prominence thresholds) was fixed at 2% for the reference device, as supported by prior research. However, for the WDs, the amplitude threshold required further investigation due to variability in signal characteristics. Different thresholds (i.e., 1%, 2%, 5%, 10%, 15%, and 20%) were tested to assess their impact on measurement accuracy. For each threshold, RR values were extracted breath-by-breath across the entire validation protocol. The MAPE was then calculated for each tested threshold. Moreover, false positives and false negatives were assessed to select an optimal threshold per each device under test.

To determine false positives and false negatives, a new method was developed based on the comparison between the breaths detected by the tested device with those identified by the reference system. This method ensured that only true positives, breaths identified by both systems, were considered as reliable breaths. It excluded false positives (breaths detected only by the device) and false negatives (breaths detected only by the reference system). By aligning the number of breaths analyzed in both systems, this approach resolved common

issues of misalignment, where a breath detected by one system might not correspond to its counterpart in the other. This alignment made it possible to compare RR values breath by breath more accurately, helping to calculate MAPE reliably across different thresholds and better evaluate each device's performance against the reference. To implement this approach the following procedure was used: for each event (i.e., breathing cycle identified as inspiratory peak) in the reference signal (denoted as L_R^i , where $i = 1, \dots, NR$), the time distance ($dist_{i,j}$) between this event and all events in signal 2 (L_D^j , where $j = 1, \dots, ND$) was calculated. Signal 2 refers to the generic device under test. The event in signal 2 with the smallest distance (j^* such that $dist_{i,j^*} < dist_{i,j},\ j = 1, \dots, ND$) was selected for comparison with L_R^i. NR is the number of breaths on the reference device, while ND is the number of breaths on the generic device under test.

TRs were then calculated for both signals. For the reference device the period was computed as $T_R^i = L_R^{i+1} - L_R^i$, while for the device it was $T_D^{j^*} = L_D^{j^*+1} - L_D^{j^*}$. Hence the algorithm classified events into the following categories:

- True positives: a breath is considered as true positive if there is a breath in the device signal that fell within the interval $[L_R^i - T_R^i/2\ , L_R^i + T_R^i/2\ ]$.
- False positives: a breath is considered as false positive if there is a breath in the device signal, but it doesn't fall within the previously mentioned interval or if it was not the closest match for any reference breath.
- False negative: a breath is counted as false negative if, considering an event in the reference signal, no corresponding breath in the device fell in the interval $L_R^i - T_R^i/2, L_R^i + T_R^i/2]$.

Using this method, threshold values were identified by balancing the trade-off between minimizing false positives, and false negatives, while maintaining low MAPE values.

The results show that increasing the prominence threshold generally reduced the MAPE for the BH and CT devices, as shown in Figure 4.12A. This reflects more accurate breath detection at higher thresholds for these devices. In contrast, the TW device exhibited an increase in MAPE at higher prominence values, with the lowest MAPE observed at thresholds between 2% and 5%.

The rise in MAPE for the TW device at higher thresholds was primarily due to an increase in false negatives, as valid breaths were missed by the device (Figure 4.12B). Meanwhile, false positives (extra breaths detected only by the device) were higher for the TW device at lower thresholds (1%–2%) but decreased as the prominence increased (Figure 4.12C). The BH system shows a decreasing MAPE and fewer false positives as the prominence threshold increases, but with a rise in false negatives. Conversely, the CT system maintains a stable MAPE, with consistently low false negatives and slightly decreasing false positives, outperforming BH in reliability across all thresholds.

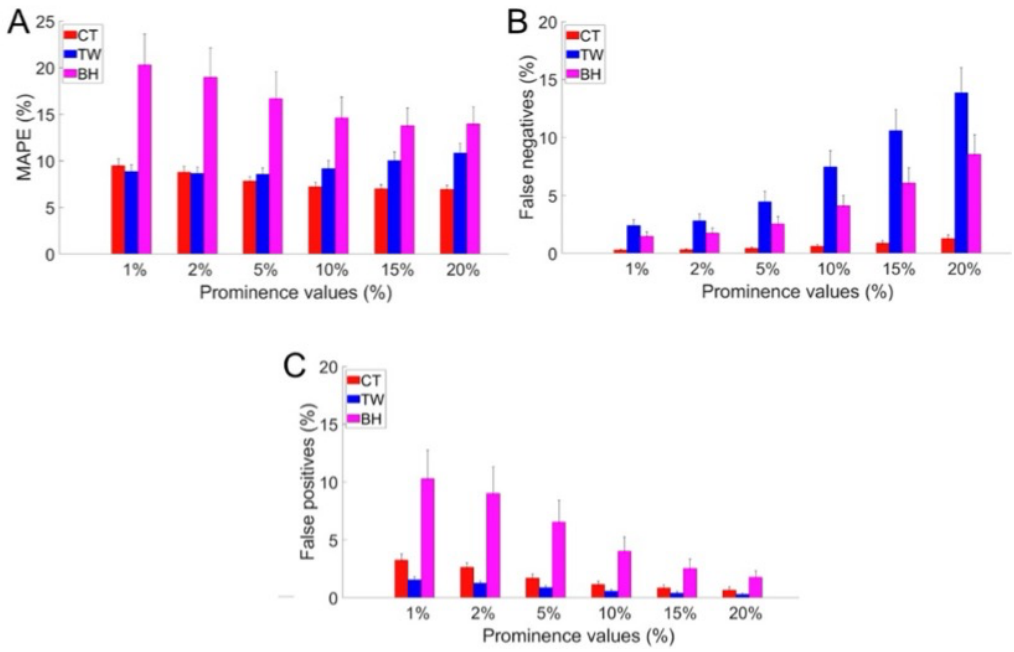

Figure 4.12: MAPE (A), false negative (B) and false positive (C) values found per each prominence values. All WDs under test and all the protocol phases were considered in the analysis separately. Adapted from [310].

Based on the results, the optimal identified thresholds were 10% for CT, 2% for TW, and 10% for BH. These findings demonstrate the need for tailored configurations to maximize the reliability of each device in RR monitoring. They also highlight the variability in device performance and the importance of customizing signal processing parameters to match the specific characteristics of wearable sensors.

Using the optimal thresholds, the breath-by-breath RR values of the WDs were extracted and compared against the reference system.

Figure 4.13 and Figure 4.14 present the breath-by-breath RR values measured by the commercial devices compared to the reference system during the RIFT and HIIT protocols. The RR trends closely followed those of the reference system, although greater interindividual variability was observed for the BH device during paced breathing, as evidenced by its higher standard deviation (SD) values.

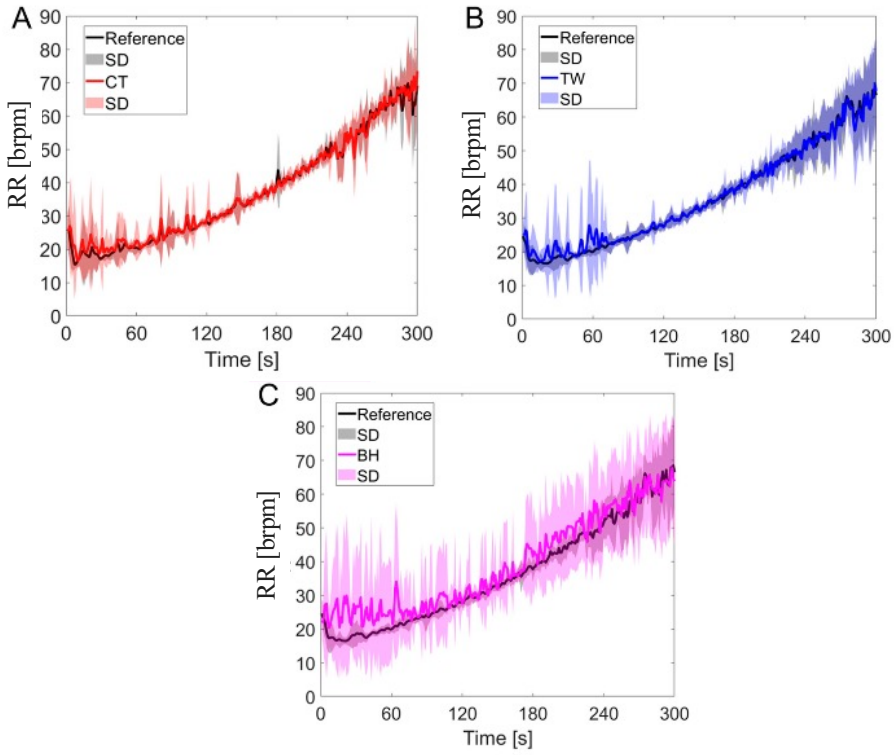

Figure 4.13: mean and standard deviation of RR values during the RIFT test considering all subjects and the three WDs under test. Adapted from [310].

During the HIIT, the RR time course measured by the CT vest closely matched the reference system. In contrast, the TW vest and BH strap showed a slight underestimation of RR, particularly at values exceeding 60 brpm.

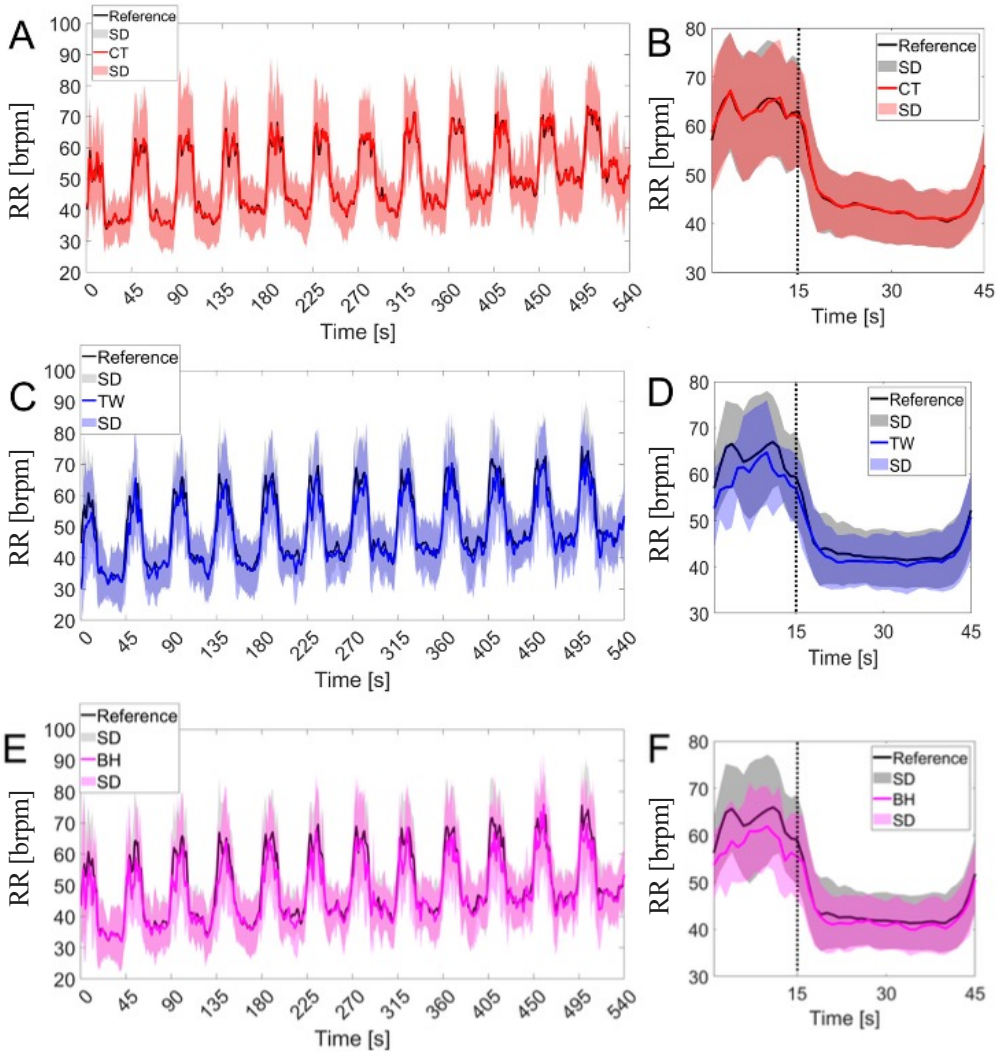

Figure 4.14: mean and standard deviation of RR values during the HIIT test considering all subjects and the three WDs under test. Adapted from [310].

This section highlights differences in device performance across individuals and conditions. The CT vest demonstrated the highest consistency, while the TW and BH devices showed limitations at higher RR levels. Additionally, the identification of false positives and false negatives was influenced by the morphology of the respiratory waveform, which varied between devices.

To further analyze system performance, RR values were averaged over 5 s, 10 s, 20 s, 30 s, and 60 s windows. This analysis investigated how window length affects RR extraction performance, as windowing is a common method for extracting breathing information. The results were also compared to those obtained through breath-by-breath RR extraction.

As shown in Figure 4.15, MAPE values varied with the length of the window used for RR extraction. The highest MAPE values occurred during breath-by-breath comparisons, while the lowest were observed with 60 s windows. Across all validation phases, the CT vest consistently outperformed the BH strap, demonstrating lower MAPE values. The TW vest performed comparably to the CT vest in most phases but showed higher MAPE values during the intermittent test. These results underline the importance of selecting appropriate window lengths and highlight the variability in device performance across different conditions.

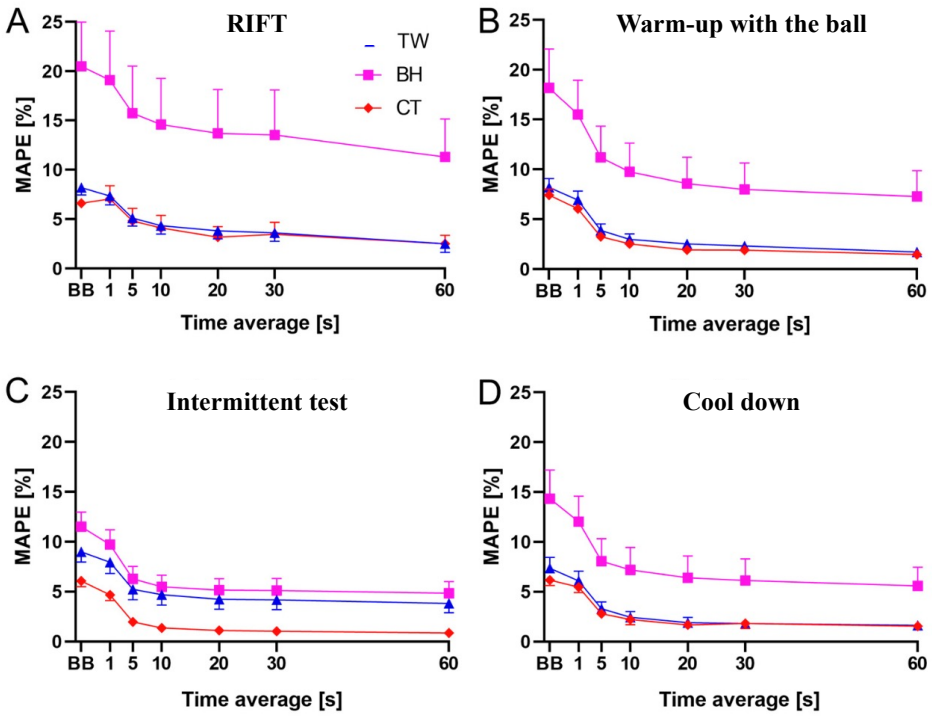

Figure 4.15: MAPE values per each window length used to calculate the average RR over time. Data are reported per each phase of the protocol and WD under test. Adapted from [310].

Considering both the breath-by-breath and windowed analyses, the CT and TW devices demonstrated better accuracy compared to the BH strap throughout the entire validation protocol. This was evident in the lower MOD and LOA values for CT and TW, as shown in Table 4.3. Among the devices, the CT vest exhibited the best overall performance, with low error rates and high signal quality, even at high RR values (>60 brpm). The TW vest also performed well but was more prone to false negatives, particularly during intense exercise. In contrast, the BH strap showed the highest error rates and was the most affected by motion artifacts.

Table 4.3: Values of MOD and LOA obtained from Bland Altman analysis of RR extracted using breath-by-breath and window-based analyses

Wearable	**Breath-by-breath analysis**		**Window analysis**	
	MOD	LOA	MOD	LOA
CT vest	0.2 brpm	12.0 brpm	0.3 brpm	2.9 brpm
TW vest	-0.3 brpm	15.7 brpm	-0.4 brpm	5.0 brpm
BH strap	1.0 brpm	24.4 brpm	0.7 brpm	10.8 brpm

Adjusting parameters like prominence thresholds and window lengths was important for improving RR monitoring accuracy. Tailoring these parameters for each device helped balance false positives and false negatives, enhancing device performance. However, these adjustments alone were not sufficient to fully mitigate the impact of motion artifacts, especially in highly dynamic environments where errors remained higher compared to other technologies, such as head-worn systems presented in the section above.

These findings highlight the limitations of current commercial devices, particularly the BH strap, in managing motion artifacts effectively. This challenge led to the development of a custom algorithm designed to identify and remove motion artifacts from respiratory signals collected by torso-mounted sensors. The next section details the design and validation of this algorithm, using the BH strap as the test device.

4.3.2. Development of an algorithm for improving the estimation of breath-by-breath RR during sports and exercise

Accurate RR monitoring in dynamic conditions is challenging due to motion artifacts, especially in WDs mounted on the torso. While optimizing parameters such as prominence thresholds and window lengths can enhance performance, these adjustments alone often fail to fully address errors caused by motion-induced noise. This limitation is especially evident in commercial devices like the BH strap, which struggle to maintain reliability in highly dynamic environments.

To overcome these challenges, this section introduces a custom algorithm specifically designed to identify and mitigate motion artifacts in respiratory signals. The algorithm was developed and validated using data collected with the BH strap, aiming to improve the accuracy of RR measurements during motion-intensive activities. The following subsections outline the algorithm's design, its implementation, and the evaluation of its effectiveness in reducing errors compared to traditional methods.

Algorithm Workflow

The algorithm was developed for data collected from strain-based wearable sensors, which measure breathing by detecting chest deformation. These sensors produce a characteristic signal pattern: an increase during inhalation and a decrease during exhalation. The algorithm's workflow comprised five main steps, starting with signal preprocessing:

1. Signal preprocessing:
    - A first-order Butterworth bandpass filter with cut-off frequencies of 0.01 Hz and 2 Hz was applied to remove noise and retain the respiratory frequency range [311].

- The derivative of the filtered signal was then calculated and scaled to fit within the range $[-1,1]$, ensuring that the signal was centered around zero and free of baseline shifts.
- To handle variations in signal amplitude, the upper ($e_{superior}$) and lower ($e_{inferior}$) root mean square envelopes ($y(t)$) were computed. Finally, a min-max normalization was then applied to retrieve a signal ($y'(t)$):

$$y'(t) = \frac{y(t) - e_{inferior}(t)}{e_{superior}(t) - e_{inferior}(t)} \quad (4.3)$$

2. Respiratory peak detection via sliding window analysis:
   - the normalized signal was segmented into 12 s sliding windows with a 2 s overlap.
   - Within each window, peaks were identified by applying both amplitude and timing thresholds.
3. Breaths' segmentation:
   - individual breaths were identified as the sections of the signal between two consecutive maximum peaks.
   - The amplitude and duration of each breath were scaled to a range of [0,1] to standardize the data.
   - An average breath template was created by calculating the mean shape from the segmented breaths, providing a reference for further analysis.
4. Exclusion of unreliable breaths:
   - The similarity between each breath and the average breath template was assessed using Pearson's correlation coefficient ($\rho_{A,B}$).
   - For each breath (A_i) compared to the average template (B), the coefficient was calculated as:

$$\rho_{(A_i,B)} = \frac{1}{N-1}\sum_{j=1}^{N}\left(\frac{A_j^i - \mu_A}{\sigma_A}\cdot\frac{B_j - \mu_B}{\sigma_B}\right) \quad (4.4)$$

Where μ and σ are the mean and standard deviation of each signal, and N is the number of samples of both waveforms.

- Breaths with a correlation coefficient below a threshold (ρ = 0.6,0.7,0.8, or 0.9 were investigated) were excluded, ensuring high-quality data for further analysis.

5. Breath-by-breath RR estimation:
   - After unreliable breaths were excluded, the TR for each reliable breath was calculated as the time interval between two consecutive peaks
   - The RR was then calculated as 60/TR, and any RR values associated with excluded breaths were disregarded.

An outline of all the steps carried out is shown in Figure 4.16.

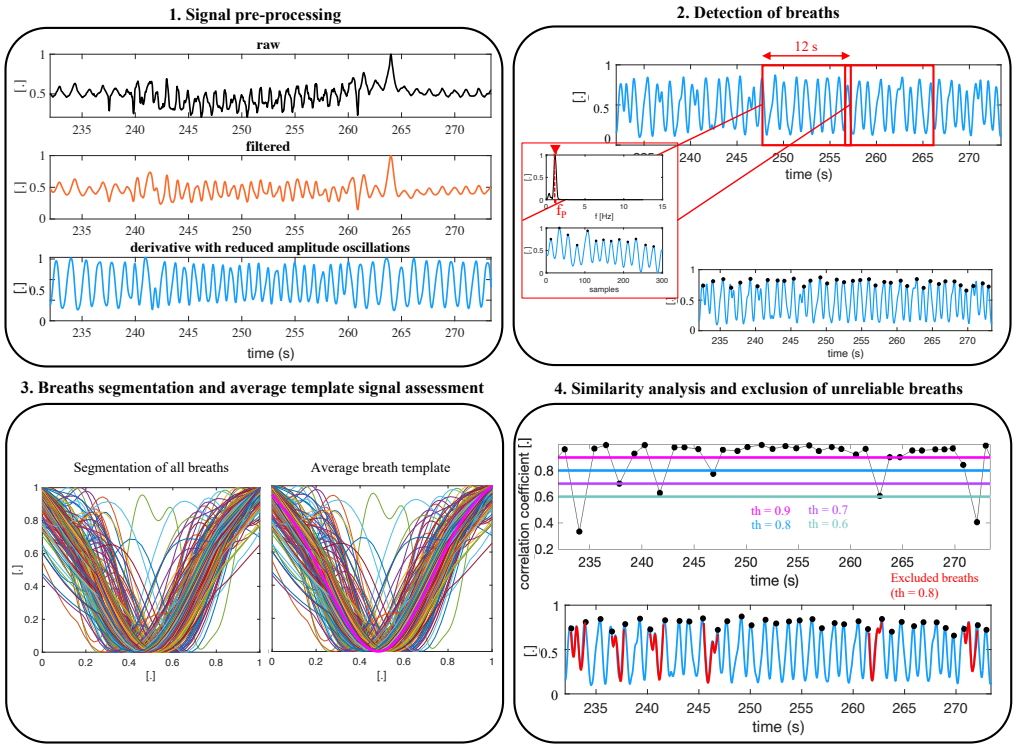

Figure 4.16: Outline of the primary steps in the SQI-based algorithm designed to exclude unreliable breaths: (a) signal preprocessing; (b) breath detection; (c) segmentation of breaths and assessment of the average template signal; (d) similarity analysis and elimination of unreliable breaths. Adapted from [312].

Algorithm Validation

a. Experiments During Running

The algorithm was tested on 33 volunteers to assess its performance during walking and running at various speeds, as well as during motionless trials. The experiments were conducted using the BH chest strap, and a flowmeter (SpiroQuant P fromEnviteC, Honeywell, North Carolina, USA) as the reference device. The protocol began with a familiarization phase, followed by a warm-up lasting 3 min on a treadmill (RHC500 Treadmill, Air Machine S.r.l., Cesena, Italy) on which also the following tests were performed. Participants then executed the synchronization sequence involving three deep breaths and a brief apnea. The experimental protocol included 60 s of quiet breathing in an upright resting position, followed by walking at 3 km/h and 6 km/h (60 s each), and running at 9 km/h and 12 km/h (60 s each). A schematization of the experimental setup and protocol is reported in Figure 4.17. The study was approved by the

Institutional Review Board of the University of Rome "Foro Italico" (CAR 112/2021) and the Ethical Committee of University Campus Bio-Medico of Rome (code: 27.2(18).20 dated June 15, 2020). All procedures adhered to the principles of the Declaration of Helsinki, and participants provided written informed consent before taking part in the study.

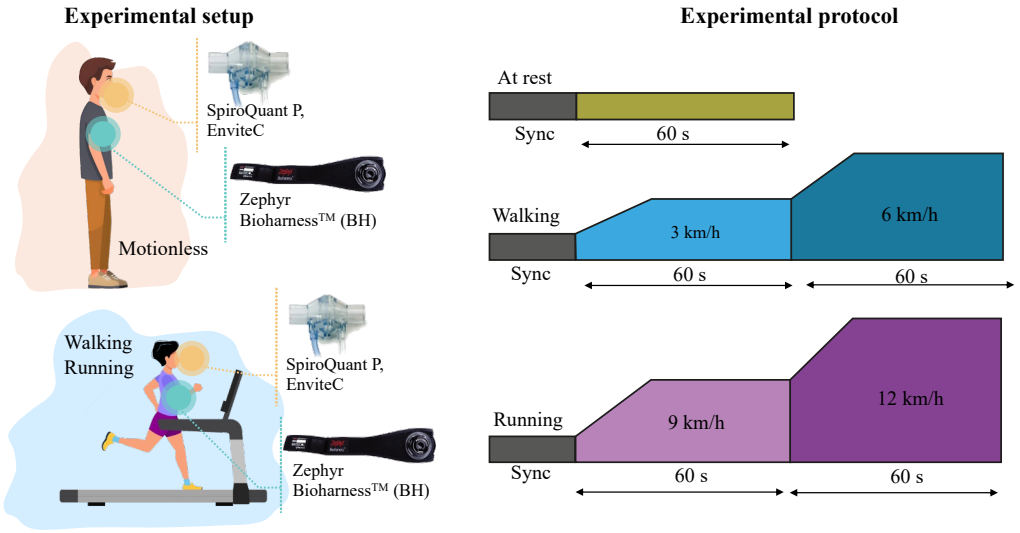

Figure 4.17: Schematization of the experimental setups (a) and protocols (b) during walking and running tests. Adapted from [312].

b. Experiments During Cycling

The algorithm was further evaluated on a group of cyclists using a cycle ergometer (WattBike Pro), paired with BH chest strap and the Quark PFT flowmeter, which served as the reference device. After the warm-up and the synchronization phase, the cyclists were asked to complete two distinct experimental trials. Firstly, they were asked to perform a RIFT, with the RR increasing exponentially from 20 brpm to 75 brpm. Then, the algorithm was tested on respiratory signals collected during HIIT, to evaluate its performance in scenarios with abrupt changes in RR. During the work phases of the HIIT, the cyclist self-selected a power output to reach approximately a score of 19 on Borg's 6–20 ratings of perceived exertion scale by the final repetition. A schematization of the experimental setup and protocol is presented in Figure 4.18.

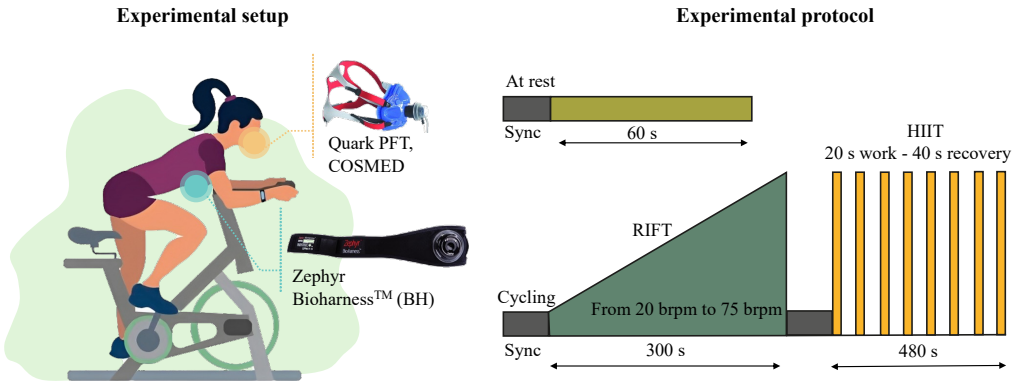

Figure 4.18: Schematization of the experimental setup (a) and protocols (b) during cycling tests. Adapted from [312].

Data analysis and results

To evaluate the performance of the proposed algorithm, RR values extracted from the BH device were compared to those from the reference system. As explained in Section 4.3.2, estimating breath-by-breath RR values involves identifying inspiration (or expiration) peaks within the signal. For a direct comparison, it is important to align the number of breaths identified in both the reference and test device signals (BH in this study). To address this challenge, the method described in the previous section was applied.

After aligning the signals and extracting RR values, different correlation threshold was investigated to provide the optimal balance between improving the MAPE improvement rate (MAPE IR, as defined in Equation 4.5) and minimizing the percentage of excluded breaths.

$$MAPE\ IR\ \% = \frac{MAPE_{noex} - MAPE_{ex}}{MAPE_{noex}} \cdot 100 \qquad (4.5)$$

MAPE IR increased across most activities when the correlation threshold was raised from 0.7 to 0.8 (see Figure 4.19). Moreover, the percentage of excluded breaths remained below 2.2% across all activities at these thresholds. At a higher threshold of 0.9, performance improved further for resting (3.2%) and running (13.0%) but declined for walking (-1.4%) and cycling (-0.1%). This

higher threshold also led to an increase in excluded breaths, reaching 10.9% for cycling and 6.7% for walking.

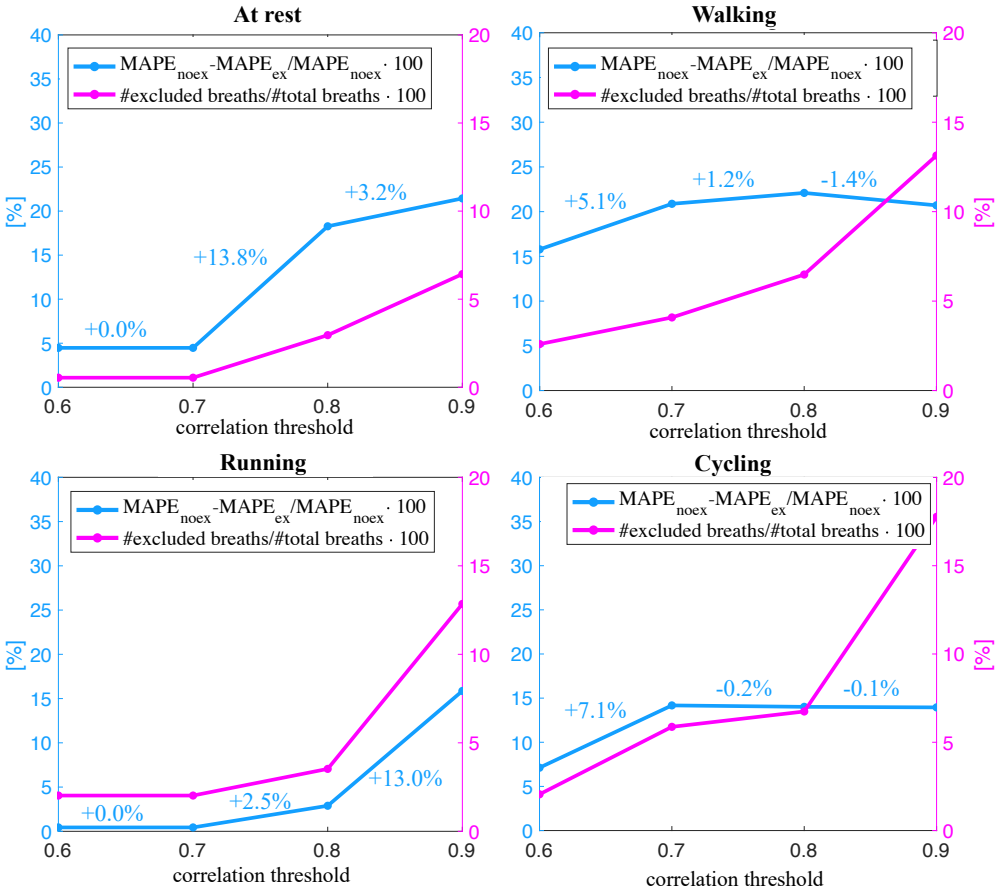

Figure 4.19: MAPE improvement rate and percentage of excluded breaths per each threshold and each protocol phase. Adapted from [312].

Based on these findings, a correlation threshold of 0.8 was selected as the most effective balance, achieving the greatest performance improvements across all activities. Figure 4.20 reports the MAPE values for all protocol activities using the selected threshold.

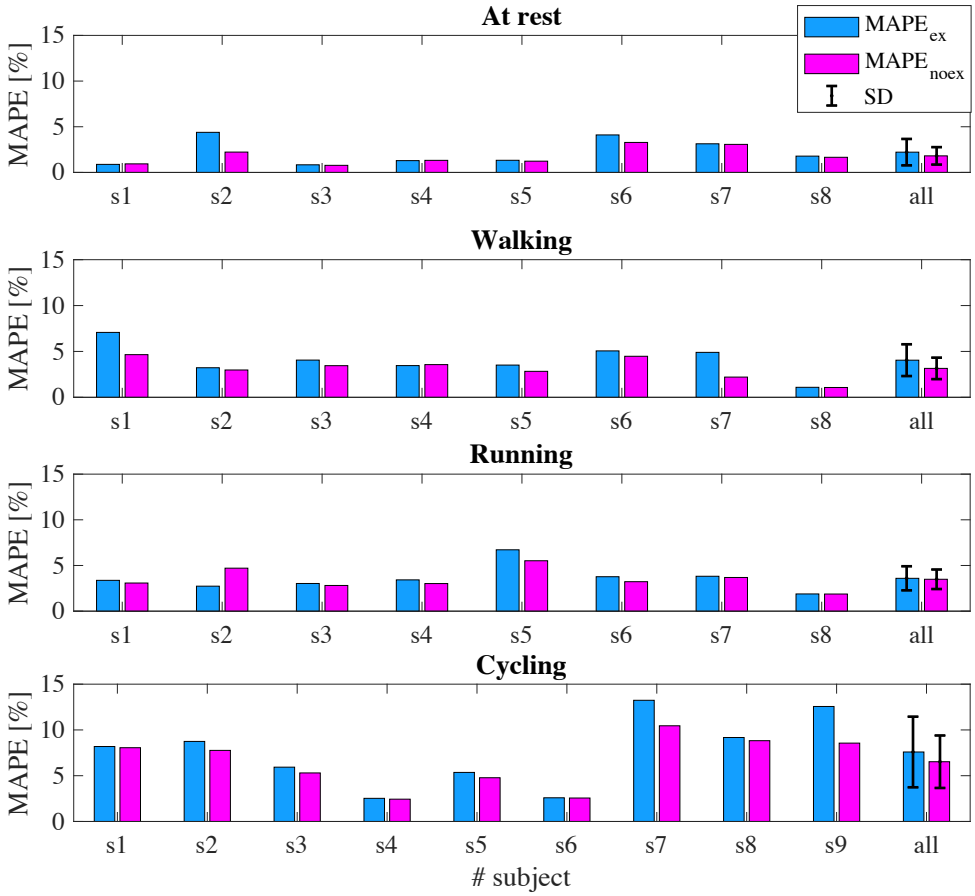

Figure 4.20: MAPE values for all subjects and all protocols using 0.8 as correlation threshold. Adapted from [312].

Focusing on HIIT, a context marked by rapid physiological fluctuations and pronounced motion artifacts, the robustness of the SQI algorithm becomes especially clear. Applying a correlation threshold of 0.8 reduced MAPE by 30.7%, while excluding only 4.4% of the total breaths. Figure 4.21 illustrates an example of a raw respiratory signal recorded during HIIT, along with RR values calculated over time both with and without the application of the exclusion algorithm.

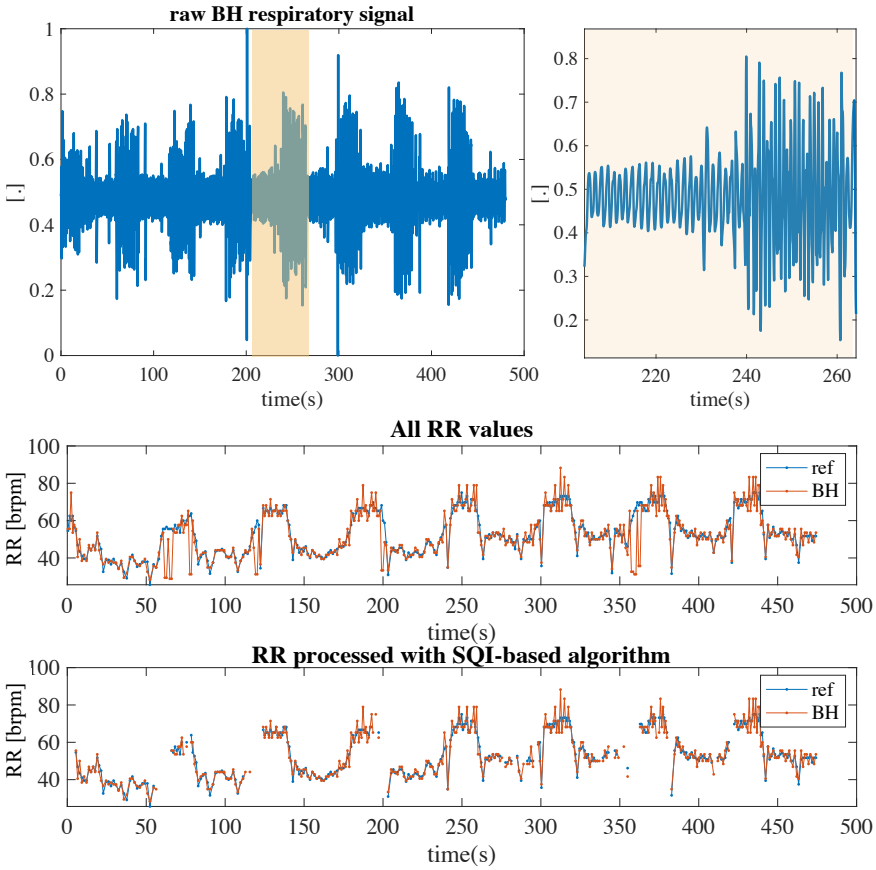

Figure 4.21: Raw normalized respiratory signal collected during HIIT (A) and respective breath-by-breath RR values (B). Also, the RR values with the exclusion of unreliable breaths are reported (C). Adapted from [312].

4.4. Conclusions

The studies presented in this chapter highlight important challenges in RR monitoring during dynamic sports activities. They show how device-specific characteristics influence measurement accuracy and reliability. WDs show considerable promise in this field, however, their effectiveness depends heavily on multiple factors, including sensor design, placement, and the algorithms used for parameter estimation. The specific movement patterns of different sports greatly affect monitoring performance. Activities with repetitive motions, such as cycling, typically yield better signal quality. In contrast, sports like soccer present greater challenges due to their unpredictable movements and sudden

directional changes. These irregular movements often lead to pronounced motion artifacts, making accurate respiratory monitoring more challenging.

The proposed smart facemask demonstrated good performance across all testing conditions. Its working principle and sensor's placement near the airways effectively minimized motion artifacts, enabling accurate breath-by-breath RR monitoring. The facemask achieved a MAE below 1 brpm and a MAPE up to 2% for breath-by-breath analysis, maintaining this accuracy even at RR values exceeding 60 brpm, and during high-intensity activities. Despite these advantages, prolonged use of the smart facemask in sports contexts may present some practical limitations. While its design minimizes airflow resistance compared to conventional respiratory masks, extended wear could still cause discomfort, particularly in endurance activities or training sessions requiring continuous use. Additionally, factors such as heat buildup and the feeling of restriction around the face may impact user compliance and long-term comfort in sustained physical activities.

In contrast, torso-worn devices prioritized comfort and ease of use but showed a greater influence on motion artefacts. Each device needed different parameters for optimal performance. For instance, while the CT vest maintained reliable measurements up to 75 brpm, the BH accuracy declined above 60 brpm. These variations in parameters to be set and performance across devices and sports contexts highlighted the importance of developing sport-specific and device-specific optimization approaches rather than pursuing universal solutions. To further address these challenges, an SQI-based algorithm was developed to identify and exclude unreliable breaths based on signal morphology. This approach reduced errors and enhanced the reliability of breath-by-breath RR estimation, even in high-intensity scenarios. For example, testing showed it reduced measurement errors by up to 30.7% during HIIT, while excluding only 4.4% of detected breaths. The algorithm's adaptability to different conditions and its effectiveness in mitigating motion artifacts demonstrate its potential to resolve one of the most persistent challenges in

wearable respiratory monitoring, particularly in sports characterized by complex movement patterns and varying intensities. Despite its potential, a limitation of the study is that, unlike the smart facemask, respiratory monitoring through chest-worn devices may be affected by physiological differences between male and female users, particularly in terms of chest wall compliance and sensor fit. Therefore, as the study was conducted exclusively on male participants, further investigation is needed to assess potential gender-related differences in sensor performance and optimization strategies for wider applicability.

These findings suggest that the development of monitoring solutions for respiratory monitoring in sports may require a tailored approach that considers not only the device characteristics but also the specific demands and constraints of different sporting activities.

5

Chapter 5: Conclusions

The digital transformation of healthcare has changed how physiological parameters are monitored and analyzed, shifting from periodic assessments in clinical settings to continuous monitoring across multiple environments. WDs have facilitated this transformation but face several challenges to ensure widespread adoption. These devices must ensure accurate measurements while maintaining user comfort and efficiently processing data to extract physiological information from noisy signals, especially for cardiac and respiratory parameters. This highlights the need for greater focus on hardware configuration and signal processing techniques.

This thesis has investigated these challenges through the development and validation of WDs solutions across three domains: daily life activities, clinical applications, and sports scenarios. Each domain presents specific requirements and challenges that influence both hardware design and signal processing approaches.

A notable finding from this research is that no single monitoring solution can effectively serve all applications. Instead, the choice of sensor technology, device configuration, and sensor's placement on the body must be adapted to the monitoring context. This was demonstrated in the analysis of IMU sensors for daily life monitoring, where among five locations on the chest wall and the three axes, the MV position and z-axis measurements proved best performance for simultaneous cardiac and respiratory assessment. However, this same configuration showed limitations during dynamic activities especially related to

respiratory monitoring, requiring alternative approaches such as the textile-based system with piezoresistive sensors, which improved the accuracy in this application.

The importance of context-specific optimization extended to the clinical domain, where the research demonstrated that both sensor positioning and algorithm selection impact diagnostic accuracy in AS classification. The identification of optimal positions at the PV and MV regions, combined with signal processing techniques, enabled high classification performance. The comparative analysis of different algorithms revealed that ML techniques, particularly SVM, achieved better performance than DL approaches. Signal window length also influenced classification accuracy, with 40 s windows reaching accuracies above 95% at the PV and MV positions, while shorter window lengths showed lower accuracy. Similarly, the HRV analysis demonstrated posture-dependent effects on measurement reliability. The supine posture yielded stronger correlations with ECG-derived reference values compared to seated measurements, for both linear and non-linear HRV indexes. This posture-dependent performance likely results from reduced motion artifacts and more stable sensor contact in the supine position, highlighting how body posture influences the quality of mechanical signal acquisition.

Research on sports science showed that unpredictable movement patterns affect monitoring performance. The smart facemask and chest-worn devices represented two distinct approaches to this challenge. The facemask's positioning near the airways minimized motion artifacts, enabling reliable breath-by-breath RR monitoring even during high-intensity activities. In contrast, chest-worn devices emphasized user comfort but required specific optimization strategies. In fact, different chest-worn devices have been analyzed and each device demonstrated different performance and requirements for signal processing parameters. For example, the CT vest showed measurement reliability at higher RR values than the BH, while each device required specific prominence thresholds for optimal performance. These variations in device

performance led to the development of the SQI-based algorithm, which addressed motion artifacts through signal morphology analysis. Using a correlation threshold of 0.8, the algorithm achieved improvements in measurement reliability: MAPE reduction of 30.7% during HIIT while excluding only 4.4% of breaths, and improvements in measurement accuracy across different activities (3.2% for resting, 13% for running).

Despite these considerations, the transition from research prototypes to widely adopted devices still faces challenges. IMU-based monitoring systems, while effective in static conditions, show a decrease in performance during movement. This limitation derives from the difficulty in separating motion-induced signals from physiological parameters, particularly affecting RR measurements during dynamic activities. Moreover, in sports applications, despite their widespread use, chest-worn devices struggle with motion artifacts. This is particularly evident in sports like soccer, where movements and rapid directional changes affect signal quality. These limitations continue to restrict the integration of wearable monitoring systems in daily healthcare and sports applications.

Looking forward, several research directions emerge. In the clinical domain, future research should focus on expanding the application of these technologies to other cardiovascular conditions while developing predictive models for early disease detection. Moreover, the daily life and sports science fields require additional efforts in developing algorithms that can account for movement patterns and physiological responses, potentially improving how physiological parameters are monitored.

In summary, this thesis contributes to the WDs field by demonstrating the importance of context-specific optimization in both sensor implementation and algorithm development. The methodologies and approaches developed provide a basis for future developments and aid in the transition to more targeted, data-driven healthcare.

Bibliography

[1] I. C. P. Marques and J. J. M. Ferreira, "Digital transformation in the area of health: systematic review of 45 years of evolution," *Health Technol. (Berl).*, vol. 10, no. 3, pp. 575–586, 2020.

[2] R. Agarwal, G. Gao, C. DesRoches, and A. K. Jha, "Research commentary—The digital transformation of healthcare: Current status and the road ahead," *Inf. Syst. Res.*, vol. 21, no. 4, pp. 796–809, 2010.

[3] A. Mohammad Mosadeghrad, "Healthcare service quality: towards a broad definition," *Int. J. Health Care Qual. Assur.*, vol. 26, no. 3, pp. 203–219, 2013.

[4] A. Shiwlani, M. Khan, A. M. K. Sherani, M. U. Qayyum, and H. K. Hussain, "REVOLUTIONIZING HEALTHCARE: THE IMPACT OF ARTIFICIAL INTELLIGENCE ON PATIENT CARE, DIAGNOSIS, AND TREATMENT," *JURIHUM J. Inov. dan Hum.*, vol. 1, no. 5, pp. 779–790, 2024.

[5] M. S. PEIRIS, "Transformative integration of artificial intelligence in telemedicine, remote healthcare, and virtual patient monitoring: Enhancing diagnostic accuracy, personalizing care," *Int. J. Intell. Healthc. Anal.*, vol. 104, no. 7, pp. 1019–1030, 2024.

[6] M. Alshamrani, "IoT and artificial intelligence implementations for remote healthcare monitoring systems: A survey," *J. King Saud Univ. Inf. Sci.*, vol. 34, no. 8, pp. 4687–4701, 2022.

[7] S. Tian, W. Yang, J. M. Le Grange, P. Wang, W. Huang, and Z. Ye, "Smart healthcare: making medical care more intelligent," *Glob. Heal. J.*, vol. 3, no. 3, pp. 62–65, 2019.

[8] S. Sikdar and S. Guha, "Advancements of healthcare technologies: Paradigm towards smart healthcare systems," *Recent trends image signal Process. Comput. Vis.*, pp. 113–132, 2020.

[9] B. Meskó, Z. Drobni, É. Bényei, B. Gergely, and Z. Győrffy, "Digital health is a cultural transformation of traditional healthcare," *Mhealth*, vol. 3, 2017.

[10] N. Chawla, "AI, IOT and Wearable Technology for Smart Healthcare-A Review.," *Int. J. Recent Res. Asp.*, vol. 7, no. 1, 2020.

[11] S. Iqbal, I. Mahgoub, E. Du, M. A. Leavitt, and W. Asghar, "Advances in healthcare wearable devices," *npj Flex. Electron.*, vol. 5, no. 1, pp. 1–14, 2021.

[12] M. S. Patel, D. A. Asch, and K. G. Volpp, "Wearable devices as facilitators, not drivers, of health behavior change," *Jama*, vol. 313, no. 5, pp. 459–460, 2015.

[13] D. Prabhakaran *et al.*, "Cardiovascular, respiratory, and related disorders: key messages from Disease Control Priorities," *Lancet*, vol. 391, no. 10126, pp. 1224–1236, 2018.

[14] who, "Global health estimates 2015: deaths by cause, age, sex, by country and by region, 2000–2015," *Geneva World Heal. Organ.*, 2016.

[15] A. H. Krist, S. T. Tong, R. A. Aycock, and D. R. Longo, "Engaging patients in decision-making and behavior change to promote prevention," *Inf. Serv. Use*, vol. 37, no. 2, pp.

105–122, 2017.

[16] S. T. Cheung and J. Wu, “The development of wearable mobile health devices in promoting healthy lifestyles,” in *SDG3–Good Health and Wellbeing: Re-Calibrating the SDG Agenda: Concise Guides to the United Nations Sustainable Development Goals*, Emerald Publishing Limited, 2019, pp. 107–124.

[17] A. Ç. Seçkin, B. Ateş, and M. Seçkin, “Review on Wearable Technology in sports: Concepts, Challenges and opportunities,” *Appl. Sci.*, vol. 13, no. 18, p. 10399, 2023.

[18] E. Svertoka *et al.*, “Wearables for industrial work safety: A survey,” *Sensors*, vol. 21, no. 11, p. 3844, 2021.

[19] S. Kraus, P. Jones, N. Kailer, A. Weinmann, N. Chaparro-Banegas, and N. Roig-Tierno, “Digital transformation: An overview of the current state of the art of research,” *Sage Open*, vol. 11, no. 3, p. 21582440211047576, 2021.

[20] Statista, “Digital transformation - statistics & facts, Petroc Taylor,.” https://www.statista.com/topics/6778/digital-transformation/#topicOverview (accessed Nov. 17, 2024).

[21] E. Rudnicka, P. Napierała, A. Podfigurna, B. Męczekalski, R. Smolarczyk, and M. Grymowicz, “The World Health Organization (WHO) approach to healthy ageing,” *Maturitas*, vol. 139, pp. 6–11, 2020.

[22] R. El-Kareh and D. F. Sittig, “Enhancing diagnosis through technology: Decision support, artificial intelligence, and beyond,” *Crit. Care Clin.*, vol. 38, no. 1, pp. 129–139, 2022.

[23] A. Holzinger, C. Röcker, and M. Ziefle, “From Smart Health to Smart Hospitals BT - Smart Health: Open Problems and Future Challenges,” A. Holzinger, C. Röcker, and M. Ziefle, Eds. Cham: Springer International Publishing, 2015, pp. 1–20. doi: 10.1007/978-3-319-16226-3_1.

[24] E. Mbunge, B. Muchemwa, and J. Batani, “Sensors and healthcare 5.0: transformative shift in virtual care through emerging digital health technologies,” *Glob. Heal. J.*, vol. 5, no. 4, pp. 169–177, 2021.

[25] V. Garg, “Digital Transformation in Healthcare,” *Navig. Digit. Landsc.*, p. 387.

[26] A. I. Stoumpos, F. Kitsios, and M. A. Talias, “Digital Transformation in Healthcare: Technology Acceptance and Its Applications,” *Int. J. Environ. Res. Public Health*, vol. 20, no. 4, 2023, doi: 10.3390/ijerph20043407.

[27] A. Rehman, S. Naz, and I. Razzak, “Leveraging big data analytics in healthcare enhancement: trends, challenges and opportunities,” *Multimed. Syst.*, vol. 28, no. 4, pp. 1339–1371, 2022.

[28] A. L. Beam and I. S. Kohane, “Big data and machine learning in health care,” *Jama*, vol. 319, no. 13, pp. 1317–1318, 2018.

[29] F. Jiang *et al.*, “Artificial intelligence in healthcare: past, present and future,” *Stroke Vasc. Neurol.*, vol. 2, no. 4, 2017.

[30] K.-H. Yu, A. L. Beam, and I. S. Kohane, “Artificial intelligence in healthcare,” *Nat.*

Biomed. Eng., vol. 2, no. 10, pp. 719–731, 2018.

[31] M. Senbekov *et al.*, "The recent progress and applications of digital technologies in healthcare: a review," *Int. J. Telemed. Appl.*, vol. 2020, no. 1, p. 8830200, 2020.

[32] S. Kraus, F. Schiavone, A. Pluzhnikova, and A. C. Invernizzi, "Digital transformation in healthcare: Analyzing the current state-of-research," *J. Bus. Res.*, vol. 123, pp. 557–567, 2021.

[33] L. Minh Dang, M. J. Piran, D. Han, K. Min, and H. Moon, "A survey on internet of things and cloud computing for healthcare," *Electron.*, vol. 8, no. 7, pp. 1–49, 2019, doi: 10.3390/electronics8070768.

[34] L. Griebel *et al.*, "A scoping review of cloud computing in healthcare," *BMC Med. Inform. Decis. Mak.*, vol. 15, pp. 1–16, 2015.

[35] L. M. Orlov, "The Future of Wearables," in *Closing the Care Gap with Wearable Devices*, Productivity Press, 2022, pp. 17–40.

[36] Global wearable device market, "Wearable Medical Device Market Trends and Forecast." https://www.lucintel.com/wearable-medical-device-market.aspx (accessed Nov. 20, 2024).

[37] R. Xiao, J. A. Miller, W. J. Zafirau, E. Z. Gorodeski, and J. B. Young, "Impact of Home Health Care on Health Care Resource Utilization Following Hospital Discharge: A Cohort Study," *Am. J. Med.*, vol. 131, no. 4, pp. 395-407.e35, 2018, doi: https://doi.org/10.1016/j.amjmed.2017.11.010.

[38] S. L. Hughes *et al.*, "Impact of home care on hospital days: a meta analysis.," *Health Serv. Res.*, vol. 32, no. 4, pp. 415–432, Oct. 1997.

[39] S. Chakrabarti, N. Biswas, L. D. Jones, S. Kesari, and S. Ashili, "Smart consumer wearables as digital diagnostic tools: a review," *Diagnostics*, vol. 12, no. 9, p. 2110, 2022.

[40] F. Landi *et al.*, "A new model of integrated home care for the elderly: impact on hospital use," *J. Clin. Epidemiol.*, vol. 54, no. 9, pp. 968–970, 2001, doi: https://doi.org/10.1016/S0895-4356(01)00366-3.

[41] R. De Fazio, V. M. Mastronardi, M. De Vittorio, and P. Visconti, "Wearable sensors and smart devices to monitor rehabilitation parameters and sports performance: an overview," *Sensors*, vol. 23, no. 4, p. 1856, 2023.

[42] E. M. Pucillo, M. B. Huish, Q. Tate, E. C. O'Bryan, and T. T. Dickerson, "Global health and disability: A review and call to action for all rehabilitation professions," 2018.

[43] W. H. Organization, *Rehabilitation 2030: meeting report, Geneva, Switzerland, 10-11 July 2023*. World Health Organization, 2024.

[44] G. B. Wilkerson, A. Gupta, J. R. Allen, C. M. Keith, and M. A. Colston, "Utilization of practice session average inertial load to quantify college football injury risk," *J. Strength Cond. Res.*, vol. 30, no. 9, pp. 2369–2374, 2016.

[45] E. U. Eurostat, "Sport participation - practicing sport and physical activity," 2022. https://ec.europa.eu/eurostat/statistics-explained/index.php?title=Sport_participation_-

_practicing_sport_and_physical_activity#Context

[46] A. Nicolò, C. Massaroni, E. Schena, and M. Sacchetti, "The importance of respiratory rate monitoring: From healthcare to sport and exercise," *Sensors (Switzerland)*, vol. 20, no. 21. Multidisciplinary Digital Publishing Institute, pp. 1–45, Nov. 09, 2020. doi: 10.3390/s20216396.

[47] A. Ahmed *et al.*, "Wearable devices for anxiety & depression: a scoping review," *Comput. Methods Programs Biomed. Updat.*, vol. 3, p. 100095, 2023.

[48] J. Dunn, R. Runge, and M. Snyder, "Wearables and the medical revolution," *Per. Med.*, vol. 15, no. 5, pp. 429–448, 2018, doi: 10.2217/pme-2018-0044.

[49] A. M. Katz, *Physiology of the Heart*. Lippincott Williams & Wilkins, 2010.

[50] G. K. Prasad and J. S. Sahambi, "Classification of ECG arrhythmias using multi-resolution analysis and neural networks," in *TENCON 2003. Conference on convergent technologies for Asia-Pacific region*, 2003, vol. 1, pp. 227–231.

[51] J. P. Sahoo, "Analysis of ECG signal for Detection of Cardiac Arrhythmias." 2011.

[52] R. M. F. L. da Silva and A. de Souza Maciel, "Conduction disorders: the value of surface ECG," *Curr. Cardiol. Rev.*, vol. 17, no. 2, pp. 173–181, 2021.

[53] S. F. Nagueh *et al.*, "Recommendations for the evaluation of left ventricular diastolic function by echocardiography," *Eur. J. Echocardiogr.*, vol. 10, no. 2, pp. 165–193, 2009.

[54] G. Pestelli *et al.*, "Value of Left Ventricular Indexed Ejection Time to Characterize the Severity of Aortic Stenosis," *J. Clin. Med.*, vol. 11, no. 7, p. 1877, 2022.

[55] S. Hirschfeld, R. Meyer, J. Korfhagen, S. Kaplan, and J. Liebman, "The isovolumic contraction time of the left ventricle. An echographic study.," *Circulation*, vol. 54, no. 5, pp. 751–756, 1976.

[56] J. Karvonen and T. Vuorimaa, "Heart rate and exercise intensity during sports activities: practical application," *Sport. Med.*, vol. 5, pp. 303–311, 1988.

[57] B. Makivić, M. Nikić Djordjević, and M. S. Willis, "Heart Rate Variability (HRV) as a tool for diagnostic and monitoring performance in sport and physical activities.," *J. Exerc. Physiol. Online*, vol. 16, no. 3, 2013.

[58] S. Järvelin-Pasanen, S. Sinikallio, and M. P. Tarvainen, "Heart rate variability and occupational stress—systematic review," *Ind. Health*, vol. 56, no. 6, pp. 500–511, 2018.

[59] D. B. Geselowitz, "On the theory of the electrocardiogram," *Proc. IEEE*, vol. 77, no. 6, pp. 857–876, 1989.

[60] F. P. Branca, *Fondamenti di Ingegneria Clinica-Volume 2: Volume 2: Ecotomografia*, vol. 2. Springer Science & Business Media, 2008.

[61] A. Leatham, "Phonocardiography," *Br. Med. Bull.*, vol. 8, no. 4, pp. 333–342, 1952.

[62] A. K. Abbas and R. Bassam, *Phonocardiography signal processing*, vol. 31. Morgan & Claypool Publishers, 2009.

[63] M. J. Vieira, R. Teixeira, L. Gonçalves, and B. J. Gersh, "Left atrial mechanics: echocardiographic assessment and clinical implications," *J. Am. Soc. Echocardiogr.*, vol. 27, no. 5, pp. 463–478, 2014.

[64] R. M. Lang, V. Mor-Avi, L. Sugeng, P. S. Nieman, and D. J. Sahn, "Three-dimensional echocardiography: the benefits of the additional dimension," *J. Am. Coll. Cardiol.*, vol. 48, no. 10, pp. 2053–2069, 2006.

[65] J. E. Hall and M. E. Hall, *Guyton and Hall Textbook of Medical Physiology E-Book: Guyton and Hall Textbook of Medical Physiology E-Book*. Elsevier Health Sciences, 2020.

[66] S. Rolfe, "The importance of respiratory rate monitoring," *Br. J. Nurs.*, vol. 28, no. 8, pp. 504–508, 2019.

[67] A. Nicolò, C. Massaroni, E. Schena, and M. Sacchetti, "The importance of respiratory rate monitoring: From healthcare to sport and exercise," *Sensors*, vol. 20, no. 21, p. 6396, 2020.

[68] J. F. Fieselmann, M. S. Hendryx, C. M. Helms, and D. S. Wakefield, "Respiratory rate predicts cardiopulmonary arrest for internal medicine inpatients," *J. Gen. Intern. Med.*, vol. 8, pp. 354–360, 1993.

[69] C. Subbe, R. G. Davies, E. Williams, P. Rutherford, and L. Gemmell, "Effect of introducing the Modified Early Warning score on clinical outcomes, cardio-pulmonary arrests and intensive care utilisation in acute medical admissions," *Anaesthesia*, vol. 58, no. 8, pp. 797–802, 2003.

[70] R. Parkes, "Rate of respiration: the forgotten vital sign," *Emerg. Nurse*, vol. 19, no. 2, 2011.

[71] A. Nicolò, S. M. Marcora, and M. Sacchetti, "Respiratory frequency is strongly associated with perceived exertion during time trials of different duration," *J. Sports Sci.*, vol. 34, no. 13, pp. 1199–1206, 2016.

[72] M. Nakagawa *et al.*, "Effect of increasing respiratory rate on airway resistance and reactance in COPD patients," *Respirology*, vol. 20, no. 1, pp. 87–94, 2015.

[73] A. M. Yañez *et al.*, "Monitoring breathing rate at home allows early identification of COPD exacerbations," *Chest*, vol. 142, no. 6, pp. 1524–1529, 2012.

[74] J. F. Morris, "Spirometry in the evaluation of pulmonary function," *West. J. Med.*, vol. 125, no. 2, p. 110, 1976.

[75] S. Ramasamy and A. Balan, "Wearable sensors for ECG measurement: a review," *Sens. Rev.*, vol. 38, no. 4, pp. 412–419, 2018.

[76] N. Meziane, J. G. Webster, M. Attari, and A. J. Nimunkar, "Dry electrodes for electrocardiography," *Physiol. Meas.*, vol. 34, no. 9, p. R47, 2013.

[77] A. Alsharif, N. Cucuri, L. Dakhaikh, F. Al-Modaf, and N. El-Atab, "Structured 3D Printed Dry ECG Electrodes Using Copper Based Filament," *ECS Trans.*, vol. 109, no. 16, p. 3, 2022.

[78] A. A. Alsharif, N. S. Milan Cucuri, R. B. Mishra, and N. El-Atab, "3D printed dry

electrodes for electrophysiological signal monitoring: A review," *Adv. Mater. Technol.*, vol. 8, no. 7, p. 2201677, 2023.

[79] P. Salvo, R. Raedt, E. Carrette, D. Schaubroeck, J. Vanfleteren, and L. Cardon, "A 3D printed dry electrode for ECG/EEG recording," *Sensors Actuators A Phys.*, vol. 174, pp. 96–102, 2012.

[80] J. Liu *et al.*, "A flexible semidry electrode for long-term, high-quality electrocardiogram monitoring," *Adv. Compos. Hybrid Mater.*, vol. 6, no. 1, p. 13, 2023.

[81] G.-L. Li, J.-T. Wu, Y.-H. Xia, Q.-G. He, and H.-G. Jin, "Review of semi-dry electrodes for EEG recording," *J. Neural Eng.*, vol. 17, no. 5, p. 51004, 2020.

[82] P. J. Xu, H. Zhang, and X. M. Tao, "Textile-structured electrodes for electrocardiogram," *Text. Prog.*, vol. 40, no. 4, pp. 183–213, 2008.

[83] T. Pola and J. Vanhala, "Textile electrodes in ECG measurement," in *2007 3rd International Conference on Intelligent Sensors, Sensor Networks and Information*, 2007, pp. 635–639.

[84] H. Carvalho, A. P. Catarino, A. Rocha, and O. Postolache, "Health monitoring using textile sensors and electrodes: An overview and integration of technologies," *IEEE MeMeA 2014 - IEEE Int. Symp. Med. Meas. Appl. Proc.*, 2014, doi: 10.1109/MEMEA.2014.6860033.

[85] C. O'Mahony, K. Grygoryev, A. Ciarlone, G. Giannoni, A. Kenthao, and P. Galvin, "Design, fabrication and skin-electrode contact analysis of polymer microneedle-based ECG electrodes," *J. Micromechanics Microengineering*, vol. 26, no. 8, p. 84005, 2016.

[86] L. Ren, B. Liu, W. Zhou, and L. Jiang, "A mini review of microneedle array electrode for bio-signal recording: a review," *IEEE Sens. J.*, vol. 20, no. 2, pp. 577–590, 2019.

[87] Z. Liu *et al.*, "Multichannel microneedle dry electrode patches for minimally invasive transdermal recording of electrophysiological signals," *Microsystems Nanoeng.*, vol. 10, no. 1, p. 72, 2024.

[88] M. S. Reza, L. Jin, Y. J. Jeong, T. I. Oh, H. Kim, and K. J. Kim, "Electrospun rubber nanofiber web-based dry electrodes for biopotential monitoring," *Sensors*, vol. 23, no. 17, p. 7377, 2023.

[89] D. Doci *et al.*, "Washing and abrasion resistance of textile electrodes for ECG measurements," *Coatings*, vol. 13, no. 9, p. 1624, 2023.

[90] R. Helgason, A. Banavali, and Y. Lai, "Cohesive dry ECG sensor using silver nanowires and PDMS tuned for adhesion," *Med. Devices Sensors*, vol. 2, no. 1, p. e10025, 2019.

[91] B. Liu, H. Tang, Z. Luo, W. Zhang, Q. Tu, and X. Jin, "Wearable carbon nanotubes-based polymer electrodes for ambulatory electrocardiographic measurements," *Sensors Actuators A Phys.*, vol. 265, pp. 79–85, 2017.

[92] W.-T. Chang *et al.*, "Design of smart clothing with automatic cardiovascular diseases detection," *IEEE Trans. Human-Machine Syst.*, vol. 53, no. 5, pp. 905–914, 2023.

[93] M. A. Yokus and J. S. Jur, "Fabric-based wearable dry electrodes for body surface biopotential recording," *IEEE Trans. Biomed. Eng.*, vol. 63, no. 2, pp. 423–430, 2015.

[94] A. Pourahmad and A. Mahnam, “Evaluation of a low-cost and low-noise active dry electrode for long-term biopotential recording,” *J. Med. Signals Sensors*, vol. 6, no. 4, pp. 197–202, 2016.

[95] J. Lozano and B. Stoeber, “Fabrication and characterization of a microneedle array electrode with flexible backing for biosignal monitoring,” *Biomed. Microdevices*, vol. 23, pp. 1–19, 2021.

[96] Y. Huang, Y. Song, L. Gou, and Y. Zou, “A novel wearable flexible dry electrode based on cowhide for ECG measurement,” *Biosensors*, vol. 11, no. 4, p. 101, 2021.

[97] O. T. Inan *et al.*, “Ballistocardiography and Seismocardiography: A Review of Recent Advances,” *IEEE J. Biomed. Heal. Informatics*, vol. 19, no. 4, pp. 1414–1427, Jul. 2015, doi: 10.1109/JBHI.2014.2361732.

[98] F. Santucci, D. Lo Presti, C. Massaroni, E. Schena, and R. Setola, “Precordial vibrations: A review of wearable systems, signal processing techniques, and main applications,” *Sensors*, vol. 22, no. 15, p. 5805, 2022.

[99] J. M. Zanetti and D. M. Salerno, “Seismocardiography: a technique for recording precordial acceleration,” in *Computer-Based Medical Systems-Proceedings of the Fourth Annual IEEE Symposium*, 1991, pp. 4–5.

[100] K. Sørensen, S. E. Schmidt, A. S. Jensen, P. Søgaard, and J. J. Struijk, “Definition of fiducial points in the normal seismocardiogram,” *Sci. Rep.*, vol. 8, no. 1, p. 15455, 2018.

[101] A. Taebi, B. E. Solar, A. J. Bomar, R. H. Sandler, and H. A. Mansy, “Recent advances in seismocardiography,” *Vibration*, vol. 2, no. 1, pp. 64–86, 2019.

[102] G. Shafiq, S. Tatinati, W. T. Ang, and K. C. Veluvolu, “Automatic identification of systolic time intervals in seismocardiogram,” *Sci. Rep.*, vol. 6, no. 1, p. 37524, 2016.

[103] M. J. Tadi *et al.*, “A new algorithm for segmentation of cardiac quiescent phases and cardiac time intervals using seismocardiography,” in *Sixth International Conference on Graphic and Image Processing (ICGIP 2014)*, 2015, vol. 9443, pp. 571–577.

[104] R. P. Lewis, S. E. Rittogers, W. F. Froester, and Hari. Boudoulas, “A critical review of the systolic time intervals.,” *Circulation*, vol. 56, no. 2, pp. 146–158, 1977.

[105] O. Lahdenoja *et al.*, “Atrial Fibrillation Detection via Accelerometer and Gyroscope of a Smartphone,” *IEEE J. Biomed. Heal. Informatics*, vol. 22, no. 1, pp. 108–118, Jan. 2018, doi: 10.1109/JBHI.2017.2688473.

[106] G. Johnson, P. Pianosi, and R. Rajamani, “Estimation of Three-Dimensional Thoracoabdominal Displacements During Respiration Using Inertial Measurement Units,” *IEEE/ASME Trans. Mechatronics*, pp. 1–11, 2022, doi: 10.1109/TMECH.2022.3151837.

[107] A. Angelucci and A. Aliverti, “An IMU-based wearable system for respiratory rate estimation in static and dynamic conditions,” *Cardiovasc. Eng. Technol.*, vol. 14, no. 3, pp. 351–363, 2023.

[108] P. K. Sahoo, H. K. Thakkar, W.-Y. Lin, P.-C. Chang, and M.-Y. Lee, “On the Design of an Efficient Cardiac Health Monitoring System Through Combined Analysis of ECG and SCG Signals,” *Sensors (Basel).*, vol. 18, no. 2, p. 379, Jan. 2018, doi:

10.3390/s18020379.

[109] M. H. Rahmani, R. Berkvens, and M. Weyn, “Chest-worn inertial sensors: A survey of applications and methods,” *Sensors*, vol. 21, no. 8. MDPI AG, Apr. 02, 2021. doi: 10.3390/s21082875.

[110] M. Jafari Tadi *et al.*, “Gyrocardiography: A new non-invasive monitoring method for the assessment of cardiac mechanics and the estimation of hemodynamic variables,” *Sci. Rep.*, vol. 7, no. 1, p. 6823, 2017.

[111] Y. D’Mello *et al.*, “Real-time cardiac beat detection and heart rate monitoring from combined seismocardiography and gyrocardiography,” *Sensors*, vol. 19, no. 16, p. 3472, 2019.

[112] M. Jafari Tadi *et al.*, “Gyrocardiography: A new non-invasive monitoring method for the assessment of cardiac mechanics and the estimation of hemodynamic variables,” *Sci. Rep.*, vol. 7, no. 1, Dec. 2017, doi: 10.1038/s41598-017-07248-y.

[113] P. Dehkordi, K. Tavakolian, M. J. Tadi, V. Zakeri, and F. Khosrow-Khavar, “Investigating the estimation of cardiac time intervals using gyrocardiography,” *Physiol. Meas.*, vol. 41, no. 5, p. 55004, 2020.

[114] H. Ashouri, S. Hersek, and O. T. Inan, “Universal pre-ejection period estimation using seismocardiography: quantifying the effects of sensor placement and regression algorithms,” *IEEE Sens. J.*, vol. 18, no. 4, pp. 1665–1674, 2017.

[115] R. Fadil *et al.*, “Temporal changes of fiducial seismocardiogram points due to different sensor placements on the chest,” in *2020 Computing in Cardiology*, 2020, pp. 1–4.

[116] S. Sieciński, P. S. Kostka, and E. J. Tkacz, “Gyrocardiography: a review of the definition, history, waveform description, and applications,” *Sensors*, vol. 20, no. 22, p. 6675, 2020.

[117] D. Lo Presti *et al.*, “Fiber bragg gratings for medical applications and future challenges: A review,” *IEEE Access*, vol. 8, pp. 156863–156888, 2020, doi: 10.1109/ACCESS.2020.3019138.

[118] J. Nedoma, M. Fajkus, P. Siska, R. Martinek, and V. Vasinek, “Non-invasive fiber optic probe encapsulated into PolyDiMethylSiloxane for measuring respiratory and heart rate of the human body,” *Adv. Electr. Electron. Eng.*, vol. 15, no. 1, pp. 93–100, 2017.

[119] J. Nedoma, M. Fajkus, R. Martinek, and H. Nazeran, “Vital sign monitoring and cardiac triggering at 1.5 tesla: A practical solution by an mr-ballistocardiography fiber-optic sensor,” *Sensors*, vol. 19, no. 3, p. 470, 2019.

[120] D. Lo Presti *et al.*, “Wearable system based on flexible fbg for respiratory and cardiac monitoring,” *IEEE Sens. J.*, vol. 19, no. 17, pp. 7391–7398, 2019, doi: 10.1109/JSEN.2019.2916320.

[121] D. Lo Presti, F. Santucci, C. Massaroni, D. Formica, R. Setola, and E. Schena, “A multi-point heart rate monitoring using a soft wearable system based on fiber optic technology,” *Sci. Rep.*, vol. 11, no. 1, pp. 1–10, Oct. 2021, doi: 10.1038/s41598-021-00574-2.

[122] A. A. Alian and K. H. Shelley, “Photoplethysmography,” *Best Pract. Res. Clin.*

Anaesthesiol., vol. 28, no. 4, pp. 395–406, 2014.

[123] G. Fortino and V. Giampà, "PPG-based methods for non invasive and continuous blood pressure measurement: An overview and development issues in body sensor networks," in *2010 IEEE International Workshop on Medical Measurements and Applications*, 2010, pp. 10–13.

[124] D. Pollreisz and N. TaheriNejad, "Detection and removal of motion artifacts in PPG signals," *Mob. Networks Appl.*, vol. 27, no. 2, pp. 728–738, 2022.

[125] M. J. Butler, J. A. Crowe, B. R. Hayes-Gill, and P. I. Rodmell, "Motion limitations of non-contact photoplethysmography due to the optical and topological properties of skin," *Physiol. Meas.*, vol. 37, no. 5, p. N27, 2016.

[126] C. Yang and N. Tavassolian, "Combined seismo-and gyro-cardiography: A more comprehensive evaluation of heart-induced chest vibrations," *IEEE J. Biomed. Heal. informatics*, vol. 22, no. 5, pp. 1466–1475, 2017.

[127] C. Massaroni, A. Nicolò, D. Lo Presti, M. Sacchetti, S. Silvestri, and E. Schena, *Contact-based methods for measuring respiratory rate*, vol. 19, no. 4. Multidisciplinary Digital Publishing Institute, 2019, pp. 1–49. doi: 10.3390/s19040908.

[128] C. Massaroni, A. Nicolò, D. Lo Presti, M. Sacchetti, S. Silvestri, and E. Schena, "Contact-based methods for measuring respiratory rate," *Sensors*, vol. 19, no. 4, p. 908, 2019.

[129] M. Folke, L. Cernerud, M. Ekström, and B. Hök, "Critical review of non-invasive respiratory monitoring in medical care," *Med. Biol. Eng. Comput.*, vol. 41, pp. 377–383, 2003.

[130] T. G. Beckwith, *Mechanical measurements*. Pearson Education India, 2007.

[131] A. Nicolò, C. Massaroni, and L. Passfield, "Respiratory frequency during exercise: The neglected physiological measure," *Front. Physiol.*, vol. 8, no. DEC, 2017, doi: 10.3389/fphys.2017.00922.

[132] L. Guidetti, M. Meucci, F. Bolletta, G. Pietro Emerenziani, M. C. Gallotta, and C. Baldari, "Validity, reliability and minimum detectable change of COSMED K5 portable gas exchange system in breath-by-breath mode," *PLoS One*, vol. 13, no. 12, p. e0209925, 2018.

[133] H. H. Bruun, "Hot-wire anemometry: principles and signal analysis," *Meas. Sci. Technol.*, vol. 7, no. 10, p. 24, 1996.

[134] I. Yoshiya, T. Nakajima, I. Nagai, and S. Jitsukawa, "A bidirectional respiratory flowmeter using the hot-wire principle," *J. Appl. Physiol.*, vol. 38, no. 2, pp. 360–365, 1975.

[135] E. Schena, P. Saccomandi, and S. Silvestri, "A high sensitivity fiber optic macro-bend based gas flow rate transducer for low flow rates: Theory, working principle, and static calibration," *Rev. Sci. Instrum.*, vol. 84, no. 2, 2013.

[136] L. Mohanty and K. S. C. Kuang, "A breathing rate sensor with plastic optical fiber," *Appl. Phys. Lett.*, vol. 97, no. 7, 2010.

[137] A. R. A. Sovijarvi, F. Dalmasso, J. Vanderschoot, L. P. Malmberg, G. Righini, and S. A. T. Stoneman, "Definition of terms for applications of respiratory sounds," *Eur. Respir. Rev.*, vol. 10, no. 77, pp. 597–610, 2000.

[138] C. Romano *et al.*, "Respiratory Rate Estimation during Walking and Running Using Breathing Sounds Recorded with a Microphone," *Biosensors*, vol. 13, no. 6, p. 637, 2023.

[139] P. Höppe, "Temperatures of expired air under varying climatic conditions," *Int. J. Biometeorol.*, vol. 25, pp. 127–132, 1981.

[140] Y. P. Huang, M.-S. Young, and C. C. Tai, "Noninvasive respiratory monitoring system based on the piezoceramic transducer's pyroelectric effect," *Rev. Sci. Instrum.*, vol. 79, no. 3, 2008.

[141] Y.-P. Huang and K.-N. Huang, "Monitoring of breathing rate by a piezofilm sensor using pyroelectric effect," in *2013 1st International Conference on Orange Technologies (ICOT)*, 2013, pp. 99–102.

[142] D. A. Krohn, T. MacDougall, and A. Mendez, *Fiber optic sensors: fundamentals and applications*, vol. 4. Spie Press Bellingham, Washington, 2014.

[143] Ł. Dziuda, F. W. Skibniewski, M. Krej, and P. M. Baran, "Fiber Bragg grating-based sensor for monitoring respiration and heart activity during magnetic resonance imaging examinations," *J. Biomed. Opt.*, vol. 18, no. 5, p. 57006, 2013.

[144] R. D. Branson and M. A. Gentile, "Is humidification always necessary during noninvasive ventilation in the hospital?," *Respir. Care*, vol. 55, no. 2, pp. 209–216, 2010.

[145] H. Farahani, R. Wagiran, and M. N. Hamidon, "Humidity sensors principle, mechanism, and fabrication technologies: a comprehensive review," *Sensors*, vol. 14, no. 5, pp. 7881–7939, 2014.

[146] I. Smith, J. Mackay, N. Fahrid, and D. Krucheck, "Respiratory rate measurement: a comparison of methods," *Br. J. Healthc. Assist.*, vol. 5, no. 1, pp. 18–23, 2011.

[147] J. M. Corres, I. R. Matias, M. Hernaez, J. Bravo, and F. J. Arregui, "Optical fiber humidity sensors using nanostructured coatings of SiO $ _ {2} $ nanoparticles," *IEEE Sens. J.*, vol. 8, no. 3, pp. 281–285, 2008.

[148] S. Iacoponi *et al.*, "Polymer-coated fiber optic probe for the monitoring of breathing pattern and respiratory rate," in *2018 40th Annual International Conference of the IEEE Engineering in Medicine and Biology Society (EMBC)*, 2018, pp. 1616–1619.

[149] R. S. Figliola and D. E. Beasley, *Theory and design for mechanical measurements*. John Wiley & Sons, 2014.

[150] T.-V. Dinh, I.-Y. Choi, Y.-S. Son, and J.-C. Kim, "A review on non-dispersive infrared gas sensors: Improvement of sensor detection limit and interference correction," *Sensors Actuators B Chem.*, vol. 231, pp. 529–538, 2016.

[151] T. Katagiri, K. Shibayama, T. Iida, and Y. Matsuura, "Infrared hollow optical fiber probe for localized carbon dioxide measurement in respiratory tracts," *Sensors*, vol. 18, no. 4, p. 995, 2018.

[152] R. De Fazio, M. Stabile, M. De Vittorio, R. Velázquez, and P. Visconti, "An overview of wearable piezoresistive and inertial sensors for respiration rate monitoring," *Electronics (Switzerland)*, vol. 10, no. 17. Multidisciplinary Digital Publishing Institute, p. 2178, Sep. 06, 2021. doi: 10.3390/electronics10172178.

[153] D. Naranjo-Hernández *et al.*, "Smart vest for respiratory rate monitoring of COPD patients based on non-contact capacitive sensing," *Sensors*, vol. 18, no. 7, p. 2144, 2018.

[154] S. K. Kundu, S. Kumagai, and M. Sasaki, "A wearable capacitive sensor for monitoring human respiratory rate," *Jpn. J. Appl. Phys.*, vol. 52, no. 4S, p. 04CL05, 2013.

[155] T. S. Chadha *et al.*, "Validation of respiratory inductive plethysmography using different calibration procedures," *Am. Rev. Respir. Dis.*, vol. 125, no. 6, pp. 644–649, 1982.

[156] D. Lo Presti *et al.*, "Cardio-respiratory monitoring in archery using a smart textile based on flexible fiber bragg grating sensors," *Sensors (Switzerland)*, vol. 19, no. 16, 2019, doi: 10.3390/s19163581.

[157] F. De Tommasi, D. Lo Presti, M. Carassiti, E. Schena, and C. Massaroni, "Smart mattress based on fiber bragg grating sensors for respiratory monitoring: A feasibility test," in *2021 IEEE International Workshop on Metrology for Industry 4.0 and IoT, MetroInd 4.0 and IoT 2021 - Proceedings*, 2021, pp. 532–537. doi: 10.1109/MetroInd4.0IoT51437.2021.9488539.

[158] F.-T. Wang, H.-L. Chan, C.-L. Wang, H.-M. Jian, and S.-H. Lin, "Instantaneous respiratory estimation from thoracic impedance by empirical mode decomposition," *Sensors*, vol. 15, no. 7, pp. 16372–16387, 2015.

[159] G. Karacocuk *et al.*, "Inertial Sensor-Based Respiration Analysis," *IEEE Trans. Instrum. Meas.*, vol. 68, no. 11, pp. 4268–4275, 2019, doi: 10.1109/TIM.2018.2889363.

[160] K. Pandia, O. T. Inan, G. T. A. Kovacs, and L. Giovangrandi, "Extracting respiratory information from seismocardiogram signals acquired on the chest using a miniature accelerometer," *Physiol. Meas.*, vol. 33, no. 10, pp. 1643–1660, 2012, doi: 10.1088/0967-3334/33/10/1643.

[161] M. Jafari Tadi *et al.*, "A novel dual gating approach using joint inertial sensors: Implications for cardiac PET imaging," *Phys. Med. Biol.*, vol. 62, no. 20, pp. 8080–8101, Oct. 2017, doi: 10.1088/1361-6560/aa8b09.

[162] J. Di Tocco, L. Raiano, R. Sabbadini, C. Massaroni, D. Formica, and E. Schena, "A Wearable System with Embedded Conductive Textiles and an IMU for Unobtrusive Cardio-Respiratory Monitoring," *Sensors 2021, Vol. 21, Page 3018*, vol. 21, no. 9, p. 3018, Apr. 2021, doi: 10.3390/S21093018.

[163] G. G. Berntson, J. T. Cacioppo, and K. S. Quigley, "Respiratory sinus arrhythmia: Autonomic origins, physiological mechanisms, and psychophysiological implications," *Psychophysiology*, vol. 30, no. 2, pp. 183–196, 1993.

[164] J. Skoric *et al.*, "Respiratory Modulation of Sternal Motion in the Context of Seismocardiography," *IEEE Sens. J.*, vol. 22, no. 13, pp. 13055–13066, 2022, doi: 10.1109/JSEN.2022.3173205.

[165] P. H. Charlton *et al.*, "Breathing rate estimation from the electrocardiogram and photoplethysmogram: A review," *IEEE Rev. Biomed. Eng.*, vol. 11, pp. 2–20, 2017.

[166] E. Helfenbein, R. Firoozabadi, S. Chien, E. Carlson, and S. Babaeizadeh, "Development of three methods for extracting respiration from the surface ECG: A review," *J. Electrocardiol.*, vol. 47, no. 6, pp. 819–825, 2014.

[167] I. Alikhani, K. Noponen, A. Hautala, R. Ammann, and T. Seppänen, "Spectral fusion-based breathing frequency estimation; experiment on activities of daily living," *Biomed. Eng. Online*, vol. 17, pp. 1–12, 2018.

[168] T. Tamura, Y. Maeda, M. Sekine, and M. Yoshida, "Wearable photoplethysmographic sensors—past and present," *Electronics*, vol. 3, no. 2, pp. 282–302, 2014.

[169] S. D. Bergese *et al.*, "Multicenter study validating accuracy of a continuous respiratory rate measurement derived from pulse oximetry: a comparison with capnography," *Anesth. Analg.*, vol. 124, no. 4, pp. 1153–1159, 2017.

[170] J. L. Moraes, M. X. Rocha, G. G. Vasconcelos, J. E. Vasconcelos Filho, V. H. C. De Albuquerque, and A. R. Alexandria, "Advances in photopletysmography signal analysis for biomedical applications," *Sensors*, vol. 18, no. 6, p. 1894, 2018.

[171] L. Francés-Morcillo, P. Morer-Camo, M. I. Rodríguez-Ferradas, and A. Cazón-Martín, "Wearable Design Requirements Identification and Evaluation," *Sensors*, vol. 20, no. 9. 2020. doi: 10.3390/s20092599.

[172] U. Anliker, H. Junker, P. Lukowicz, and G. Tröster, "Design Methodology for Context-Aware Wearable Sensor Systems BT - Pervasive Computing," 2005, pp. 220–236.

[173] E. Vanegas, R. Igual, and I. Plaza, "Sensing systems for respiration monitoring: A technical systematic review," *Sensors*, vol. 20, no. 18, p. 5446, 2020.

[174] A. Aliverti, "Wearable technology: role in respiratory health and disease," *Breathe*, vol. 13, no. 2, pp. e27–e36, 2017.

[175] S. Sieciński, P. S. Kostka, and E. J. Tkacz, "Gyrocardiography: A review of the definition, history, waveform description, and applications," *Sensors (Switzerland)*, vol. 20, no. 22, pp. 1–30, 2020, doi: 10.3390/s20226675.

[176] O. T. Inan *et al.*, "Ballistocardiography and seismocardiography: A review of recent advances," *IEEE J. Biomed. Heal. informatics*, vol. 19, no. 4, pp. 1414–1427, 2014.

[177] C. Zeagler, "Where to wear it: functional, technical, and social considerations in on-body location for wearable technology 20 years of designing for wearability," in *Proceedings of the 2017 ACM International Symposium on Wearable Computers*, 2017, pp. 150–157.

[178] K. T. Sweeney, T. E. Ward, and S. F. McLoone, "Artifact removal in physiological signals—Practices and possibilities," *IEEE Trans. Inf. Technol. Biomed.*, vol. 16, no. 3, pp. 488–500, 2012.

[179] N. Gautam *et al.*, "Artificial Intelligence, Wearables and Remote Monitoring for Heart failure: current and future applications," *Diagnostics*, vol. 12, no. 12, p. 2964, 2022.

[180] J. Dunn, R. Runge, and M. Snyder, "Wearables and the medical revolution," *Per. Med.*, vol. 15, no. 5, pp. 429–448, 2018.

[181] S. Beniczky, P. Karoly, E. Nurse, P. Ryvlin, and M. Cook, "Machine learning and

wearable devices of the future," *Epilepsia*, vol. 62, pp. S116–S124, 2021.

[182] D. R. Witt, R. A. Kellogg, M. P. Snyder, and J. Dunn, "Windows into human health through wearables data analytics," *Curr. Opin. Biomed. Eng.*, vol. 9, pp. 28–46, 2019.

[183] D. H. Phan, S. Bonnet, R. Guillemaud, E. Castelli, and N. Y. P. Thi, "Estimation of respiratory waveform and heart rate using an accelerometer," in *2008 30th Annual International Conference of the IEEE Engineering in Medicine and Biology Society*, 2008, pp. 4916–4919.

[184] M. H. Rahmani, R. Berkvens, and M. Weyn, "Chest-worn inertial sensors: A survey of applications and methods," *Sensors*, vol. 21, no. 8, p. 2875, 2021.

[185] A. Angelucci *et al.*, "Smart textiles and sensorized garments for physiological monitoring: A review of available solutions and techniques," *Sensors*, vol. 21, no. 3, p. 814, 2021.

[186] R. De Fazio, M. Stabile, M. De Vittorio, R. Velázquez, and P. Visconti, "An overview of wearable piezoresistive and inertial sensors for respiration rate monitoring," *Electronics*, vol. 10, no. 17, p. 2178, 2021.

[187] R. S. Crow, P. Hannan, D. Jacobs, L. Hedquist, and D. M. Salerno, "Relationship between seismocardiogram and echocardiogram for events in the cardiac cycle," *Am. J. noninvasive Cardiol.*, vol. 8, no. 1, pp. 39–46, 1994.

[188] S. Sieciński, P. S. Kostka, and E. J. Tkacz, "Heart rate variability analysis on electrocardiograms, seismocardiograms and gyrocardiograms on healthy volunteers," *Sensors (Switzerland)*, vol. 20, no. 16, pp. 1–16, 2020, doi: 10.3390/s20164522.

[189] C. Yang and N. Tavassolian, "Combined Seismo-and Gyro-Cardiography: A More Comprehensive Evaluation of Heart-Induced Chest Vibrations," *IEEE J. Biomed. Heal. Informatics*, vol. 22, no. 5, pp. 1466–1475, Sep. 2018, doi: 10.1109/JBHI.2017.2764798.

[190] A. Buke, F. Gaoli, W. Yongcai, S. Lei, and Y. Zhiqi, "Healthcare algorithms by wearable inertial sensors: a survey," *China Commun.*, vol. 12, no. 4, pp. 1–12, 2015.

[191] M. Jafari Tadi *et al.*, "Gyrocardiography: A new non-invasive monitoring method for the assessment of cardiac mechanics and the estimation of hemodynamic variables," *Sci. Rep.*, vol. 7, no. 1, pp. 1–11, 2017.

[192] T. Choudhary, M. K. Bhuyan, and L. N. Sharma, "Delineation and analysis of seismocardiographic systole and diastole profiles," *IEEE Trans. Instrum. Meas.*, vol. 70, pp. 1–8, 2020.

[193] F. Khosrow-Khavar, K. Tavakolian, A. Blaber, and C. Menon, "Automatic and robust delineation of the fiducial points of the seismocardiogram signal for noninvasive estimation of cardiac time intervals," *IEEE Trans. Biomed. Eng.*, vol. 64, no. 8, pp. 1701–1710, 2016.

[194] J. Zia, J. Kimball, M. H. Shandhi, and O. T. Inan, "Automated identification of persistent time-domain features in seismocardiogram signals," in *2019 IEEE EMBS International Conference on Biomedical & Health Informatics (BHI)*, 2019, pp. 1–4.

[195] G. Shafiq, S. Tatinati, and K. C. Veluvolu, "Automatic annotation of peaks in seismocardiogram for systolic time intervals," in *2016 38th Annual International*

Conference of the IEEE Engineering in Medicine and Biology Society (EMBC), 2016, pp. 2672–2675.

[196] T. Choudhary, M. K. Bhuyan, and L. N. Sharma, "A novel method for aortic valve opening phase detection using SCG signal," *IEEE Sens. J.*, vol. 20, no. 2, pp. 899–908, 2019.

[197] N. Mora, F. Cocconcelli, G. Matrella, and P. Ciampolini, "A unified methodology for heartbeats detection in seismocardiogram and ballistocardiogram signals," *Computers*, vol. 9, no. 2, p. 41, 2020.

[198] P. T. Gamage, M. K. Azad, A. Taebi, R. H. Sandler, and H. A. Mansy, "Clustering seismocardiographic events using unsupervised machine learning," in *2018 IEEE Signal Processing in Medicine and Biology Symposium (SPMB)*, 2018, pp. 1–5.

[199] A. Taebi, B. E. Solar, and H. A. Mansy, "An adaptive feature extraction algorithm for classification of seismocardiographic signals," in *SoutheastCon 2018*, 2018, pp. 1–5.

[200] H. Ashouri and O. T. Inan, "Automatic detection of seismocardiogram sensor misplacement for robust pre-ejection period estimation in unsupervised settings," *IEEE Sens. J.*, vol. 17, no. 12, pp. 3805–3813, 2017.

[201] X. Cao, J. Wang, X. Zhang, and J. Tang, "A ballistocardiogram measurement system for home monitoring: design, performance, and evaluation," *Chinese Sci. Bull.*, vol. 59, pp. 2909–2917, 2014.

[202] O. T. Inan *et al.*, "Novel wearable seismocardiography and machine learning algorithms can assess clinical status of heart failure patients," *Circ. Hear. Fail.*, vol. 11, no. 1, p. e004313, 2018.

[203] S. Hughes, H. Liu, and D. Zheng, "Influences of Sensor Placement Site and Subject Posture on Measurement of Respiratory Frequency Using Triaxial Accelerometers," *Front. Physiol.*, vol. 11, p. 539417, Jul. 2020, doi: 10.3389/fphys.2020.00823.

[204] S. Hughes, H. Liu, and D. Zheng, "Influences of sensor placement site and subject posture on measurement of respiratory frequency using triaxial accelerometers," *Front. Physiol.*, vol. 11, p. 823, 2020.

[205] L. Raiano, J. Di Tocco, C. Massaroni, G. Di Pino, E. Schena, and D. Formica, "A PCA-Based Method to Select the Number and the Body Location of Piezoresistive Sensors in a Wearable System for Respiratory Monitoring," *IEEE Sens. J.*, vol. 21, no. 5, pp. 6847–6855, Mar. 2021, doi: 10.1109/JSEN.2020.3043140.

[206] H. R. Koo *et al.*, "The effect of textile-based inductive coil sensor positions for heart rate monitoring," *J. Med. Syst.*, vol. 38, pp. 1–12, 2014.

[207] C. Romano, D. Formica, E. Schena, and C. Massaroni, "Investigation Of Body Locations For Cardiac And Respiratory Monitoring with Skin-Interfaced Inertial Measurement Unit Sensors," *IEEE Sens. J.*, 2023.

[208] D. Jarchi, S. J. Rodgers, L. Tarassenko, and D. A. Clifton, "Accelerometry-based estimation of respiratory rate for post-intensive care patient monitoring," *IEEE Sens. J.*, vol. 18, no. 12, pp. 4981–4989, 2018.

[209] J. Pan and W. J. Tompkins, "A real-time QRS detection algorithm," *IEEE Trans.*

Biomed. Eng., no. 3, pp. 230–236, 1985.

[210] M. Di Rienzo *et al.*, "Wearable seismocardiography: Towards a beat-by-beat assessment of cardiac mechanics in ambulant subjects," *Auton. Neurosci.*, vol. 178, no. 1–2, pp. 50–59, 2013.

[211] A. Cesareo, Y. Previtali, E. Biffi, and A. Aliverti, "Assessment of breathing parameters using an inertial measurement unit (IMU)-based system," *Sensors (Switzerland)*, vol. 19, no. 1, Jan. 2019, doi: 10.3390/s19010088.

[212] G. Karacocuk *et al.*, "Inertial sensor-based respiration analysis," *IEEE Trans. Instrum. Meas.*, vol. 68, no. 11, pp. 4268–4275, 2019.

[213] Y. D'Mello *et al.*, "Autocorrelated Differential Algorithm for Real-Time Seismocardiography Analysis," *IEEE Sens. J.*, vol. 19, no. 13, pp. 5127–5140, 2019, doi: 10.1109/JSEN.2019.2903449.

[214] S. Yu and S. Liu, "A novel adaptive recursive least squares filter to remove the motion artifact in seismocardiography," *Sensors (Switzerland)*, vol. 20, no. 6, 2020, doi: 10.3390/s20061596.

[215] A. for the A. of M. Instrumentation, "ANSI/AAMI EC13: 2002 Cardiac monitors, heart rate meters, and alarms," *Arlington, Virginia, Assoc. Adv. Med. Instrum.*, p. 21, 2002.

[216] C. Romano, E. Schena, D. Formica, and C. Massaroni, "Comparison between Chest-Worn Accelerometer and Gyroscope Performance for Heart Rate and Respiratory Rate Monitoring," *Biosensors*, vol. 12, no. 10, 2022, doi: 10.3390/bios12100834.

[217] M. Kaisti *et al.*, "Stand-Alone Heartbeat Detection in Multidimensional Mechanocardiograms," *IEEE Sens. J.*, vol. 19, no. 1, pp. 234–242, Jan. 2019, doi: 10.1109/JSEN.2018.2874706.

[218] M. J. Tadi, O. Lahdenoja, T. Humanen, J. Koskinen, M. Pankaala, and T. Koivisto, "Automatic identification of signal quality for heart beat detection in cardiac MEMS signals," *2017 IEEE EMBS Int. Conf. Biomed. Heal. Informatics, BHI 2017*, pp. 137–140, 2017, doi: 10.1109/BHI.2017.7897224.

[219] Y. D'Mello *et al.*, "Real-time cardiac beat detection and heart rate monitoring from combined seismocardiography and gyrocardiography," *Sensors (Switzerland)*, vol. 19, no. 16, Aug. 2019, doi: 10.3390/s19163472.

[220] H. Lee, H. Lee, and M. Whang, "An enhanced method to estimate heart rate from seismocardiography via ensemble averaging of body movements at six degrees of freedom," *Sensors*, vol. 18, no. 1, p. 238, 2018.

[221] N. Molinaro, E. Schena, S. Silvestri, and C. Massaroni, "Multi-ROI Spectral Approach for the Continuous Remote Cardio-Respiratory Monitoring from Mobile Device Built-In Cameras," *Sensors*, vol. 22, no. 7, 2022, doi: 10.3390/s22072539.

[222] I. S. O. Vim, "International vocabulary of basic and general terms in metrology (VIM)," *Int. Organ.*, vol. 2004, pp. 9–14, 2004.

[223] G. Ferrigno, P. Carnevali, A. Aliverti, F. Molteni, G. Beulcke, and A. Pedotti, "Three-dimensional optical analysis of chest wall motion," *J. Appl. Physiol.*, vol. 77, no. 3, pp. 1224–1231, 1994.

[224] C. Romano, D. Lo Presti, J. Dickinson, E. Schena, S. Silvestri, and C. Massaroni, "Design And Development Of A Flexible Wearable Sensor Based On A Conductive Textile For Breathing Monitoring," in *2023 International Workshop on Biomedical Applications, Technologies and Sensors (BATS)*, 2023, pp. 51–56.

[225] A. Atalay *et al.*, "Batch fabrication of customizable silicone-textile composite capacitive strain sensors for human motion tracking," *Adv. Mater. Technol.*, vol. 2, no. 9, p. 1700136, 2017.

[226] O. Atalay, A. Tuncay, M. D. Husain, and W. R. Kennon, "Comparative study of the weft-knitted strain sensors," *J. Ind. Text.*, vol. 46, no. 5, pp. 1212–1240, 2017.

[227] M. Liu, R. Del-Rio-Ruiz, A. Sharma, C. Asci, R. Owyeung, and S. Sonkusale, "Preliminary Results on Sensing Pillow to Monitor Head Movement using strain sensing threads," in *2022 IEEE Sensors*, 2022, pp. 1–4.

[228] C. M. Otto, "Timing of aortic valve surgery," *Heart*, vol. 84, no. 2, pp. 211–218, 2000.

[229] A. S. Update, "Heart disease and stroke statistics–2017 update," *Circulation*, vol. 135, pp. e146–e603, 2017.

[230] F. A. Elhaj, N. Salim, A. R. Harris, T. T. Swee, and T. Ahmed, "Arrhythmia recognition and classification using combined linear and nonlinear features of ECG signals," *Comput. Methods Programs Biomed.*, vol. 127, pp. 52–63, 2016.

[231] B. H. Freed *et al.*, "Prognostic utility and clinical significance of cardiac mechanics in heart failure with preserved ejection fraction: importance of left atrial strain," *Circ. Cardiovasc. Imaging*, vol. 9, no. 3, p. e003754, 2016.

[232] A. Pasipoularides, "Cardiac mechanics: basic and clinical contemporary research," *Ann. Biomed. Eng.*, vol. 20, pp. 3–17, 1992.

[233] M. P. Nash and P. J. Hunter, "Computational mechanics of the heart," *J. Elast. Phys. Sci. solids*, vol. 61, pp. 113–141, 2000.

[234] M. F. Jan and A. J. Tajik, "Modern imaging techniques in cardiomyopathies," *Circ. Res.*, vol. 121, no. 7, pp. 874–891, 2017.

[235] P. M. T. Pattynama, A. De Roos, E. E. Van der Wall, and A. E. Van Voorthuisen, "Evaluation of cardiac function with magnetic resonance imaging," *Am. Heart J.*, vol. 128, no. 3, pp. 595–607, 1994.

[236] C. M. Kolind *et al.*, "Seismocardiography and echocardiography: the correlation in the systolic complex," *Biomed. Phys. Eng. Express*, vol. 10, no. 5, p. 55025, 2024.

[237] I. Korzeniowska-Kubacka, B. Kuśmierczyk-Droszcz, M. Bilińska, B. Dobraszkiewicz-Wasilewska, K. Mazurek, and R. Piotrowicz, "Seismocardiography-a non-invasive method of assessing systolic and diastolic left ventricular function in ischaemic heart disease," *Cardiol. J.*, vol. 13, no. 4, pp. 319–325, 2006.

[238] K. Tavakolian *et al.*, "Myocardial contractility: A seismocardiography approach," in *2012 Annual International Conference of the IEEE Engineering in Medicine and Biology Society*, 2012, pp. 3801–3804.

[239] P. Dehkordi, E. P. Bauer, K. Tavakolian, Z. G. Xiao, A. P. Blaber, and F. Khosrow-

Khavar, “Detecting coronary artery disease using rest seismocardiography and gyrocardiography,” *Front. Physiol.*, vol. 12, p. 758727, 2021.

[240] S. Mehrang *et al.*, “Machine learning based classification of myocardial infarction conditions using smartphone-derived seismo-and gyrocardiography,” in *2018 Computing in Cardiology Conference (CinC)*, 2018, vol. 45, pp. 1–4.

[241] M. J. Tadi, E. Lehtonen, T. Koivisto, M. Pänkäälä, A. Paasio, and M. Teräs, “Seismocardiography: Toward heart rate variability (HRV) estimation,” in *2015 IEEE International Symposium on Medical Measurements and Applications (MeMeA) Proceedings*, 2015, pp. 261–266.

[242] S. Sieciński, P. S. Kostka, and E. J. Tkacz, “Heart rate variability analysis on electrocardiograms, seismocardiograms and gyrocardiograms on healthy volunteers,” *Sensors (Switzerland)*, vol. 20, no. 16, pp. 1–16, Aug. 2020, doi: 10.3390/s20164522.

[243] S. Parlato, J. Centracchio, D. Esposito, P. Bifulco, and E. Andreozzi, “ECG-Free Heartbeat Detection in Seismocardiography and Gyrocardiography Signals Provides Acceptable Heart Rate Variability Indices in Healthy and Pathological Subjects,” *Sensors*, vol. 23, no. 19, p. 8114, 2023.

[244] T. Choudhary, M. Das, L. N. Sharma, and M. K. Bhuyan, “Analyzing seismocardiographic approach for heart rate variability measurement,” *Biomed. Signal Process. Control*, vol. 68, p. 102793, 2021.

[245] C. Yang, B. D. Ojha, N. D. Aranoff, P. Green, and N. Tavassolian, “Classification of aortic stenosis using conventional machine learning and deep learning methods based on multi-dimensional cardio-mechanical signals,” *Sci. Rep.*, vol. 10, no. 1, p. 17521, 2020.

[246] A. Shokouhmand, N. D. Aranoff, E. Driggin, P. Green, and N. Tavassolian, “Efficient detection of aortic stenosis using morphological characteristics of cardiomechanical signals and heart rate variability parameters,” *Sci. Rep.*, vol. 11, no. 1, pp. 1–14, 2021.

[247] B. L. Thomas, N. Claassen, P. Becker, and M. Viljoen, “Validity of commonly used heart rate variability markers of autonomic nervous system function,” *Neuropsychobiology*, vol. 78, no. 1, pp. 14–26, 2019.

[248] J. Sztajzel, “Heart rate variability: a noninvasive electrocardiographic method to measure the autonomic nervous system,” *Swiss Med. Wkly.*, vol. 134, no. 3536, pp. 514–522, 2004.

[249] M. J. Reed, C. E. Robertson, and P. S. Addison, “Heart rate variability measurements and the prediction of ventricular arrhythmias,” *Qjm*, vol. 98, no. 2, pp. 87–95, 2005.

[250] S. Guzzetti, R. Magatelli, E. Borroni, and S. Mezzetti, “Heart rate variability in chronic heart failure,” *Auton. Neurosci.*, vol. 90, no. 1–2, pp. 102–105, 2001.

[251] F. Lombardi, T. H. Mäkikallio, R. J. Myerburg, and H. V Huikuri, “Sudden cardiac death: role of heart rate variability to identify patients at risk,” *Cardiovasc. Res.*, vol. 50, no. 2, pp. 210–217, 2001.

[252] F. Lombardi and P. K. Stein, “Origin of heart rate variability and turbulence: an appraisal of autonomic modulation of cardiovascular function,” *Front. Physiol.*, vol. 2, p. 95, 2011.

[253] H. V Huikuri and P. K. Stein, “Clinical application of heart rate variability after acute myocardial infarction,” *Front. Physiol.*, vol. 3, p. 41, 2012.

[254] C. S. Zuern, P. Barthel, and A. Bauer, “Heart rate turbulence as risk-predictor after myocardial infarction,” *Front. Physiol.*, vol. 2, p. 15620, 2011.

[255] H. F. Jelinek, Z. Q. Huang, A. H. Khandoker, D. Chang, and H. Kiat, “Cardiac rehabilitation outcomes following a 6-week program of PCI and CABG Patients,” *Front. Physiol.*, vol. 4, p. 302, 2013.

[256] R. Hartmann, F. M. Schmidt, C. Sander, and U. Hegerl, “Heart rate variability as indicator of clinical state in depression,” *Front. psychiatry*, vol. 9, p. 735, 2019.

[257] J. Ramos-Castro *et al.*, “Heart rate variability analysis using a seismocardiogram signal,” in *Proceedings of the Annual International Conference of the IEEE Engineering in Medicine and Biology Society, EMBS*, 2012, pp. 5642–5645. doi: 10.1109/EMBC.2012.6347274.

[258] Č. Milena *et al.*, “Linear and Non-Linear Heart Rate Variability Indexes from Heart-Induced Mechanical Signals Recorded with a Skin-Interfaced IMU,” *Sensors*, vol. 23, no. 3, p. 1615, 2023.

[259] T. Higuchi, “Approach to an irregular time series on the basis of the fractal theory,” *Phys. D Nonlinear Phenom.*, vol. 31, no. 2, pp. 277–283, 1988.

[260] C.-K. Peng, J. M. Hausdorff, and A. L. Goldberger, “Fractal mechanisms in neuronal control: human heartbeat and gait dynamics in health and disease,” *Self-organized Biol. Dyn. nonlinear Control Towar. Underst. complexity, chaos emergent Funct. living Syst.*, pp. 66–96, 2000.

[261] J. S. Richman and J. R. Moorman, “Physiological time-series analysis using approximate entropy and sample entropy,” *Am. J. Physiol. Circ. Physiol.*, vol. 278, no. 6, pp. H2039–H2049, 2000.

[262] C. M. Otto and B. Prendergast, “Aortic-valve stenosis—from patients at risk to severe valve obstruction,” *N. Engl. J. Med.*, vol. 371, no. 8, pp. 744–756, 2014.

[263] B. A. Carabello and W. J. Paulus, “Aortic stenosis,” *Lancet*, vol. 373, no. 9667, pp. 956–966, 2009.

[264] J. Joseph, S. Y. Naqvi, J. Giri, and S. Goldberg, “Aortic stenosis: pathophysiology, diagnosis, and therapy,” *Am. J. Med.*, vol. 130, no. 3, pp. 253–263, 2017.

[265] N. M. Rajamannan, R. O. Bonow, and S. H. Rahimtoola, “Calcific aortic stenosis: an update,” *Nat. Clin. Pract. Cardiovasc. Med.*, vol. 4, no. 5, pp. 254–262, 2007.

[266] P. Carità *et al.*, “Aortic stenosis: insights on pathogenesis and clinical implications,” *J. Geriatr. Cardiol. JGC*, vol. 13, no. 6, p. 489, 2016.

[267] N. Saikrishnan, G. Kumar, F. J. Sawaya, S. Lerakis, and A. P. Yoganathan, “Accurate assessment of aortic stenosis: a review of diagnostic modalities and hemodynamics,” *Circulation*, vol. 129, no. 2, pp. 244–253, 2014.

[268] V. Rizzello, “Moderate gradient severe aortic stenosis: diagnosis, prognosis and therapy,” *Eur. Hear. J. Suppl.*, vol. 23, no. Supplement_E, pp. E133–E137, 2021.

[269] R. A. Nishimura *et al.*, "2017 AHA/ACC focused update of the 2014 AHA/ACC guideline for the management of patients with valvular heart disease: a report of the American College of Cardiology/American Heart Association Task Force on Clinical Practice Guidelines," *Circulation*, vol. 135, no. 25, pp. e1159–e1195, 2017.

[270] R. A. Nishimura *et al.*, "2014 AHA/ACC guideline for the management of patients with valvular heart disease: a report of the American College of Cardiology/American Heart Association Task Force on Practice Guidelines," *Circulation*, vol. 129, no. 23, pp. e521–e643, 2014.

[271] J. Minners, M. Allgeier, C. Gohlke-Baerwolf, R.-P. Kienzle, F.-J. Neumann, and N. Jander, "Inconsistencies of echocardiographic criteria for the grading of aortic valve stenosis," *Eur. Heart J.*, vol. 29, no. 8, pp. 1043–1048, 2008.

[272] P. Gjertsson, K. Caidahl, A. Odén, and O. Bech-Hanssen, "Diagnostic and referral delay in patients with aortic stenosis is common and negatively affects outcome," *Scand. Cardiovasc. J.*, vol. 41, no. 1, pp. 12–18, 2007.

[273] T. Hurnanen *et al.*, "Automated detection of atrial fibrillation based on time–frequency analysis of seismocardiograms," *IEEE J. Biomed. Heal. informatics*, vol. 21, no. 5, pp. 1233–1241, 2016.

[274] E. M. I. Johnson *et al.*, "Detecting aortic valve-induced abnormal flow with seismocardiography and cardiac MRI," *Ann. Biomed. Eng.*, vol. 48, pp. 1779–1792, 2020.

[275] C. Yang, B. Ojha, N. D. Aranoff, P. Green, and N. Tavassolian, "Classification of aortic stenosis before and after transcatheter aortic valve replacement using cardio-mechanical modalities," in *2020 42nd Annual International Conference of the IEEE Engineering in Medicine & Biology Society (EMBC)*, 2020, pp. 2820–2823.

[276] C. Yang, N. D. Aranoff, P. Green, and N. Tavassolian, "Classification of aortic stenosis using time–frequency features from chest cardio-mechanical signals," *IEEE Trans. Biomed. Eng.*, vol. 67, no. 6, pp. 1672–1683, 2019.

[277] M. J. Singh, S. Das, L. N. Sharma, and S. Dandapat, "Stationary Wavelet Transform Based Detection of Aortic Stenosis Using Seismocardiogram Signal," in *2023 National Conference on Communications (NCC)*, 2023, pp. 1–6.

[278] C. Romano *et al.*, "Classification of aortic stenosis patients via ECG-independent multi-site measurements of cardiac-induced accelerations and angular velocities at the skin level," *IEEE Open J. Eng. Med. Biol.*, 2024.

[279] M. Kellmann, "Preventing overtraining in athletes in high-intensity sports and stress/recovery monitoring," *Scand. J. Med. Sci. Sports*, vol. 20, pp. 95–102, 2010.

[280] D. Carey, J. Hughes, R. Raymond, and G. Pliego, "The respiratory rate as a marker for the ventilatory threshold: comparison to other ventilatory parameters," *J. Exerc. Physiol.*, vol. 8, no. 2, pp. 30–38, 2005.

[281] D. G. Carey, L. A. Schwarz, G. J. Pliego, and R. L. Raymond, "Respiratory rate is a valid and reliable marker for the anaerobic threshold: implications for measuring change in fitness," *J. Sports Sci. Med.*, vol. 4, no. 4, p. 482, 2005.

[282] B. J. Nobel, "Perceptual responses to exercise: a multiple regression study," *Med Sci*

Sport., vol. 5, pp. 104–109, 1973.

[283] A. Nicolò, S. M. Marcora, I. Bazzucchi, and M. Sacchetti, "Differential control of respiratory frequency and tidal volume during high-intensity interval training.," *Exp. Physiol.*, vol. 102, no. 8, pp. 934–949, Aug. 2017, doi: 10.1113/EP086352.

[284] W. Sun *et al.*, "A review of recent advances in vital signals monitoring of sports and health via flexible wearable sensors," *Sensors*, vol. 22, no. 20, p. 7784, 2022.

[285] A. H. Gouw, G. P. Van Guilder, G. G. Cullen, and L. C. Dalleck, "Is the Tyme Wear Smart Shirt Reliable and Valid at Detecting Personalized Ventilatory Thresholds in Recreationally Active Individuals?," *Int. J. Environ. Res. Public Health*, vol. 19, no. 3, p. 1147, 2022.

[286] G. Nazari and J. C. MacDermid, "Reliability of zephyr bioHarness respiratory rate at rest, during the modified Canadian aerobic fitness test and recovery," *J. Strength Cond. Res.*, vol. 34, no. 1, pp. 264–269, 2020.

[287] E. Mencarini, A. Rapp, L. Tirabeni, and M. Zancanaro, "Designing Wearable Systems for Sports: A Review of Trends and Opportunities in Human-Computer Interaction," *IEEE Trans. Human-Machine Syst.*, vol. 49, no. 4, pp. 314–325, Aug. 2019, doi: 10.1109/THMS.2019.2919702.

[288] C. R. Merritt, H. T. Nagle, and E. Grant, "Textile-based capacitive sensors for respiration monitoring," *IEEE Sens. J.*, vol. 9, no. 1, pp. 71–78, 2008.

[289] J. D. Witt, J. R. K. O. Fisher, J. A. Guenette, K. A. Cheong, B. J. Wilson, and A. W. Sheel, "Measurement of exercise ventilation by a portable respiratory inductive plethysmograph," *Respir. Physiol. Neurobiol.*, vol. 154, no. 3, pp. 389–395, 2006.

[290] E. Harbour, T. Stöggl, H. Schwameder, and T. Finkenzeller, "Breath tools: a synthesis of evidence-based breathing strategies to enhance human running," *Front. Physiol.*, vol. 13, p. 233, 2022.

[291] A. Nicolò and M. Sacchetti, "Differential control of respiratory frequency and tidal volume during exercise," *Eur. J. Appl. Physiol.*, pp. 1–28, 2022.

[292] Q. Lu *et al.*, "Intelligent facemask based on triboelectric nanogenerator for respiratory monitoring," *Nano Energy*, vol. 91, p. 106612, 2022.

[293] J. Zhong *et al.*, "Smart face mask based on an ultrathin pressure sensor for wireless monitoring of breath conditions," *Adv. Mater.*, vol. 34, no. 6, p. 2107758, 2022.

[294] C. Romano, A. Nicolò, L. Innocenti, M. Sacchetti, E. Schena, and C. Massaroni, "Design and Testing of a Smart Facemask for Respiratory Monitoring during Cycling Exercise," *Biosensors*, vol. 13, no. 3, p. 369, 2023.

[295] J. Jcgm, "Evaluation of measurement data—Guide to the expression of uncertainty in measurement," *Int. Organ. Stand. Geneva ISBN*, vol. 50, p. 134, 2008.

[296] G. Borg, *Borg's perceived exertion and pain scales.* Human kinetics, 1998.

[297] A. Nicolò, M. Montini, M. Girardi, F. Felici, I. Bazzucchi, and M. Sacchetti, "Respiratory frequency as a marker of physical effort during high-intensity interval training in soccer players," *Int. J. Sports Physiol. Perform.*, 2020, doi:

10.1123/ijspp.2019-0028.

[298] R. Villar, T. Beltrame, and R. L. Hughson, "Validation of the Hexoskin wearable vest during lying, sitting, standing, and walking activities," *Appl. Physiol. Nutr. Metab.*, vol. 40, no. 10, pp. 1019–1024, 2015.

[299] J. H. Kim, R. Roberge, J. B. Powell, A. B. Shafer, and W. Jon Williams, "Measurement accuracy of heart rate and respiratory rate during graded exercise and sustained exercise in the heat using the zephyr BioHarness TM," *Int. J. Sports Med.*, vol. 34, no. 6, pp. 497–501, 2013, doi: 10.1055/s-0032-1327661.

[300] J. Hailstone and A. E. Kilding, "Reliability and Validity of the Zephyr™ BioHarness™ to Measure Respiratory Responses to Exercise," *http://dx.doi.org/10.1080/1091367X.2011.615671*, vol. 15, no. 4, pp. 293–300, Oct. 2011, doi: 10.1080/1091367X.2011.615671.

[301] N. Hayward *et al.*, "A capaciflector provides continuous and accurate respiratory rate monitoring for patients at rest and during exercise," *J. Clin. Monit. Comput.*, pp. 1–12, 2022.

[302] C. Massaroni *et al.*, "Validation of a Wearable Device and an Algorithm for Respiratory Monitoring during Exercise," *IEEE Sens. J.*, vol. 19, no. 12, 2019, doi: 10.1109/JSEN.2019.2899658.

[303] P. Cardoso *et al.*, "In-situ acceleration-speed profile of an elite soccer academy: A cross-sectional study," *J. Sports Sci.*, vol. 41, no. 20, pp. 1868–1874, 2023.

[304] P. Clavel, C. Leduc, J.-B. Morin, M. Buchheit, and M. Lacome, "Reliability of individual acceleration-speed profile in-situ in elite youth soccer players," *J. Biomech.*, vol. 153, p. 111602, 2023.

[305] M. Beato, G. Devereux, and A. Stiff, "Validity and reliability of global positioning system units (STATSports Viper) for measuring distance and peak speed in sports," *J. Strength Cond. Res.*, vol. 32, no. 10, pp. 2831–2837, 2018.

[306] G. Ravé, U. Granacher, D. Boullosa, A. C. Hackney, and H. Zouhal, "How to use global positioning systems (gps) data to monitor training load in the 'real world' of elite soccer," *Front. Physiol.*, vol. 11, p. 944, 2020.

[307] J.-H. Kim, R. Roberge, J. B. Powell, A. B. Shafer, and W. J. Williams, "Measurement accuracy of heart rate and respiratory rate during graded exercise and sustained exercise in the heat using the Zephyr BioHarnessTM," *Int. J. Sports Med.*, pp. 497–501, 2012.

[308] C. A. Elliot, M. J. Hamlin, and C. A. Lizamore, "Validity and Reliability of the Hexoskin Wearable Biometric Vest during Maximal Aerobic Power Testing in Elite Cyclists," *J. Strength Cond. Res.*, vol. 33, no. 5, pp. 1437–1444, 2019, doi: 10.1519/JSC.0000000000002005.

[309] E. Harbour, M. Lasshofer, M. Genitrini, and H. Schwameder, "Enhanced Breathing Pattern Detection during Running Using Wearable Sensors," *Sensors 2021, Vol. 21, Page 5606*, vol. 21, no. 16, p. 5606, Aug. 2021, doi: 10.3390/S21165606.

[310] L. Innocenti *et al.*, "Breathing Monitoring in Soccer: Part I—Validity of Commercial Wearable Sensors," *Sensors*, vol. 24, no. 14, p. 4571, 2024.

[311] M. Zaltieri *et al.*, “Preliminary assessment of a flexible multi-sensor wearable system based on fiber bragg gratings for respiratory monitoring of hemiplegic patients,” *Int. J. Environ. Res. Public Health*, vol. 19, no. 20, p. 13525, 2022.

[312] C. Romano, L. Innocenti, E. Schena, M. Sacchetti, A. Nicolò, and C. Massaroni, “A signal quality index for improving the estimation of breath-by-breath respiratory rate during sport and exercise,” *IEEE Sens. J.*, 2023.

List of Publications

Peer Reviewed Journals (J)

	-2024-
J1	Innocenti L, Romano C, Greco G, Nuccio S, Bellini A, Mari F, Silvestri S, Schena E, Sacchetti M, Massaroni C, et al. Breathing Monitoring in Soccer: Part I—Validity of Commercial Wearable Sensors. Sensors. 2024.
J2	Romano C, Lo Presti D, Silvestri S, Schena E, Massaroni C. Flexible Textile Sensors-Based Smart T-Shirt for Respiratory Monitoring: Design, Development, and Preliminary Validation. Sensors. 2024.
J3	C. Romano, E. Maiorana, A. Nusca, S. Circhetta, S. Silvestri, G.P. Ussia and C. Massaroni "Classification of aortic stenosis patients via ECG-independent multi-site measurements of cardiac-induced accelerations and angular velocities at the skin level", IEEE Open Journal of Engineering in Medicine and Biology 2024.
	-2023-
J4	C. Romano, L. Innocenti, E. Schena, M. Sacchetti, A. Nicolò and C. Massaroni, "A Signal Quality Index for Improving the Estimation of Breath-by-Breath Respiratory Rate During Sport and Exercise," in IEEE Sensors Journal, 2023.
J5	Romano, C.; Nicolò, A.; Innocenti, L.; Bravi, M.; Miccinilli, S.; Sterzi, S.; Sacchetti, M.; Schena, E.; Massaroni, C. Respiratory Rate Estimation during Walking and Running Using Breathing Sounds Recorded with a Microphone. Biosensors 2023.
J6	E. Maiorana, C. Romano, E. Schena and C. Massaroni, "BIOWISH: Biometric Recognition using Wearable Inertial Sensors detecting Heart Activity," in IEEE Transactions on Dependable and Secure Computing, 2023.
J7	Romano, C.; Nicolò, A.; Innocenti, L.; Sacchetti, M.; Schena, E.; Massaroni, C. Design and Testing of a Smart Facemask for Respiratory Monitoring during Cycling Exercise. Biosensors 2023.
J8	C. Romano, D. Formica, E. Schena and C. Massaroni, "Investigation of Body Locations for Cardiac and Respiratory Monitoring With Skin-Interfaced Inertial Measurement Unit Sensors," in IEEE Sensors Journal, 2023.
J9	Milena, Č.; Romano, C.; De Tommasi, F.; Carassiti, M.; Formica, D.; Schena, E.; Massaroni, C. Linear and Non-Linear Heart Rate Variability Indexes from Heart-Induced Mechanical Signals Recorded with a Skin-Interfaced IMU. Sensors 2023.
	-2022-
J10	Romano, C.; Schena, E.; Formica, D.; Massaroni, C. Comparison between Chest-Worn Accelerometer and Gyroscope Performance for Heart Rate and Respiratory Rate Monitoring. Biosensors 2022.
J11	De Tommasi, F.; Romano, C.; Lo Presti, D.; Massaroni, C.; Carassiti, M.; Schena, E. FBG-Based Soft System for Assisted Epidural Anesthesia: Design Optimization and Clinical Assessment. Biosensors 2022.
	-2021-

J12	Romano, Chiara, Emiliano Schena, Sergio Silvestri, and Carlo Massaroni. 2021. "Non-Contact Respiratory Monitoring Using an RGB Camera for Real-World Applications" Sensors 2021.

Conference Proceedings (C)

	-2024-
C1	C. Romano, S. Silvestri, D. L. Presti, E. Schena, and C. Massaroni "Soft Force Sensor for Breathing Monitoring: Design, Development and Feasibility Assessment" 2024 IEEE International Workshop on Metrology for Industry 4.0 & IoT (MetroInd4.0&IoT), Firenze, Italy, 2024.
C2	L. Giorgi et al., "Assessment of an innovative smart face mask for the estimation of respiratory rate in static and dynamic conditions," 2024 IEEE International Workshop on Metrology for Industry 4.0 & IoT (MetroInd4.0 & IoT), Firenze, Italy, 2024.
C3	M. Pinnelli et al., "A Wearable Platform as a First Step towards Enabling Collective Intelligence in Alzheimer's Disease Management: Feasibility Assessment on Healthy Volunteers," 2024 IEEE International Workshop on Metrology for Industry 4.0 & IoT (MetroInd4.0 & IoT), Firenze, Italy, 2024.
C4	M. Pinnelli et al., "A Technological Platform for Quantifying Alzheimer's Patient-Caregiver Interactions in the Walk and Talk Program," 2024 IEEE International Workshop on Metrology for Industry 4.0 & IoT (MetroInd4.0 & IoT), Firenze, Italy, 2024.
	-2023-
C5	C. Romano, D. L. Presti, J. Dickinson, E. Schena, S. Silvestri and C. Massaroni, "Design And Development Of A Flexible Wearable Sensor Based On A Conductive Textile For Breathing Monitoring," 2023 International Workshop on Biomedical Applications, Technologies and Sensors (BATS), Catanzaro, Italy, 2023.
C6	D. L. Presti, C. Romano, C. Massaroni, N. Di Stefano, D. Formica and E. Schena, "Wearable Sensors to Monitor Psychophysiological Response Induced by Musical Consonance and Dissonance," 2023 International Workshop on Biomedical Applications, Technologies and Sensors (BATS), Catanzaro, Italy, 2023.
C7	C. Romano et al., "Smart Vest And Adaptive Algorithm For Vital Signs And Physical Activity Monitoring: A Feasibility Study," 2023 IEEE International Symposium on Medical Measurements and Applications (MeMeA), Jeju, Korea, Republic of, 2023.
C8	C. Massaroni, M. Sacchetti, C. Romano, E. Schena, L. Innocenti and A. Nicolò, "The effects of different algorithms on the performance of a strain-based wearable device estimating respiratory rate during cycling exercise," 2023 IEEE International Workshop on Metrology for Industry 4.0 & IoT (MetroInd4.0&IoT), Brescia, Italy, 2023.
C9	L. Giorgi et al., "An innovative smart face mask for the estimation of respiratory rate: design, development and feasibility assessment," 2023 IEEE International Workshop on Metrology for Industry 4.0 & IoT (MetroInd4.0&IoT), Brescia, Italy, 2023.
	-2022-
C10	D. Lo Presti et al., "A quantitative assessment of team members physiological traits and interactions for the development of Collective Intelligence in a clinical scenario," 2022 IEEE Intl Conf on Dependable, Autonomic and

	Secure Computing, Intl Conf on Pervasive Intelligence and Computing, Intl Conf on Cloud and Big Data Computing, Intl Conf on Cyber Science and Technology Congress (DASC/PiCom/CBDCom/CyberSciTech), Falerna, Italy, 2022.
C11	C. Massaroni, C. Romano, A. Nicolo, L. Innocenti, M. Sacchetti and E. Schena, "Continuous respiratory rate estimation with a wearable temperature sensor during cycling exercise: a feasibility study," 2022 IEEE International Workshop on Sport, Technology and Research (STAR), Trento - Cavalese, Italy, 2022.
C12	D. L. Presti, C. Romano, C. Leitão, C. Massaroni, D. Formica and E. Schena, "A soft sensor based on FBG technology for heart rate monitoring in archery," 2022 IEEE International Symposium on Medical Measurements and Applications (MeMeA), Messina, Italy, 2022.
C13	C. Massaroni et al., "Heart Rate And Heart Rate Variability Indexes Estimated By Mechanical Signals From A Skin-Interfaced IMU," 2022 IEEE International Workshop on Metrology for Industry 4.0 & IoT (MetroInd4.0&IoT), Trento, Italy, 2022.